NTNU

Norwegian University of
Science and Technology

Fractal modelling of turbulent flows
Subgrid modelling for the Burgers equation

Christopher Nilsen

Master of Science in Product Design and Manufacturing
Submission date: June 2011
Supervisor: Helge Ingolf Andersson, EPT

Norwegian University of Science and Technology
Department of Energy and Process Engineering

NTNU

Norwegian University
of Science and Technology

Department of Energy
and Process Engineering

EPT-M-2011-15

MASTER THESIS

for

Stud.techn. Christopher Nilsen
Spring 2011

Fractal modeling of turbulent flows
Fraktal modellering av turbulent strømning

Background and objective.

Turbulence models aimed for computational fluid dynamics (CFD) are developed within the framework of Reynolds-averaging and implemented in the Reynolds-averaged Navier-Stokes (RANS) equations. A rather different approach is fractal-based turbulence modelling. In this project a fractal-based subgrid model shall be used in conjunction with a statistically forced Burgers equation.

The following questions should be considered in the project work:

1 The candiate shall provide an overview of how concepts from fractal theory can be used to model turbulent flows on the basis of available literature. Advantages and disadvantages relative to the conventional Reynolds-averaged turbulence models should be identified and discussed.
2 A numerical method for the integration of the stochastically forced Burgers equation shall be programmed and the numerical accuracy of the method verified.
3 A subgrid model is to be chosen and implemented and solution of the coarse-grained Burgers equation obtained.
4 Numerical solutions of the fine-grained Burgers equation are to be compared with the coarse-grained solution.
5 The findings of the calculations are to be analysed and recommendations given for further advancements in the field of fractal turbulence modelling.

-- " --

Within 14 days of receiving the written text on the master thesis, the candidate shall submit a research plan for his project to the department.

When the thesis is evaluated, emphasis is put on processing of the results, and that they are presented in tabular and/or graphic form in a clear manner, and that they are analyzed carefully.

The thesis should be formulated as a research report with summary both in English and Norwegian, conclusion, literature references, table of contents etc. During the preparation of the

text, the candidate should make an effort to produce a well-structured and easily readable report. In order to ease the evaluation of the thesis, it is important that the cross-references are correct. In the making of the report, strong emphasis should be placed on both a thorough discussion of the results and an orderly presentation.

The candidate is requested to initiate and keep close contact with his/her academic supervisor(s) throughout the working period. The candidate must follow the rules and regulations of NTNU as well as passive directions given by the Department of Energy and Process Engineering.

Pursuant to "Regulations concerning the supplementary provisions to the technology study program/Master of Science" at NTNU §20, the Department reserves the permission to utilize all the results and data for teaching and research purposes as well as in future publications.
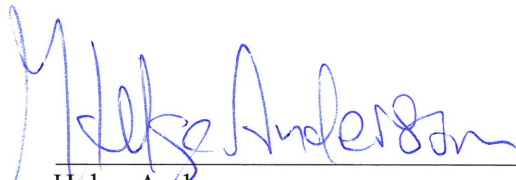
One – 1 complete original of the thesis shall be submitted to the authority that handed out the set subject. (A short summary including the author's name and the title of the thesis should also be submitted, for use as reference in journals (max. 1 page with double spacing)).
Two – 2 – copies of the thesis shall be submitted to the Department. Upon request, additional copies shall be submitted directly to research advisors/companies. A CD-ROM (Word format or corresponding) containing the thesis, and including the short summary, must also be submitted to the Department of Energy and Process Engineering

Department of Energy and Process Engineering, 17. January 2011

_____
Olav Bolland
Department Head

_____
Helge Andersson
Academic Supervisor

Preface

This thesis is the result of approximately twenty weeks of work in the period 17th of January to 14th of June. The process has been interesting and at times rather challenging, but ultimately tremendously educational.

Some of the results were presented at the MekIT'11 conference in Trondheim on the 23th and 24th of May. The article for the conference proceedings (Nilsen & Andersson, 2011) is enclosed at the end of this report in appendix D. Appendices A and B are slightly modified versions of two of the chapters in the project report I wrote last semester (Nilsen, 2010).

I would like to thank my supervisor Helge I. Andersson for his support and the freedom to pursue my interests. I would also like to thank him for encouraging me to present some of my results at the MekIT'11 conference. Additional thanks go to Finn P. Nilsen for reading the manuscript and suggesting important changes. Lastly, I would like to thank Jan B. Aarseth for a very interesting conversation about numerical methods, and my fellow students Ted Ørjan K. Gundersen and Roy-Andre Midtgård for many useful discussions.

Christopher Nilsen   Trondheim, 14th June 2011

Abstract

The stochastically forced Burgers equation shares some of the same characteristics as the three-dimensional Navier-Stokes equations. Because of this it is sometimes used as a model equation for turbulence. Simulating the stochastically forced Burgers equation with low resolution can be considered as a one dimensional model of a three-dimensional large eddy simulation, and can be used to evaluate subgrid models.

Modified versions of subgrid models using the fractal interpolation technique are presented here and tested in low resolution simulations of the stochastically forced Burgers equations. The results are compared with high resolution simulations, then low resolution simulations first using the dynamic Smagorinsky model and then using no subgrid model other than the numerical dissipation of the convective flux discretisation scheme.

The fractal models perform reasonably well and most of the large scale features from the high resolution simulations are reproduced by corresponding simulations with low resolution. The performance of the fractal models is not, however, better than the performance of the dynamic Smagorinsky model. Therefore one might say that although the fractal models give promising results, it is not obvious that they are in any way superior to the traditional models. Also the low resolution simulation with the dissipative convective scheme performs well, suggesting that numerical dissipation can be sufficient as a subgrid model in one dimension.

The solutions to the stochastically forced Burgers equation follow a $\kappa^{-\frac{5}{3}}$ energy spectrum, but high order statistics are not similar to real turbulence, due to the complete domination of shocks. Thus the stochastically forced Burgers equation might not be a suitable model for turbulence. It is not likely that the complexity of three-dimensional subgrid modelling is sufficiently represented by the one-dimensional case either.

Oppsummering

Burgers' ligning med stokastisk kildeledd deler enkelte av de samme egenskapene som Navier-Stokes-ligningene, og den blir i noen tilfeller brukt som en modelligning for turbulens. En simulering med grovt romlig nettverk kan ses på som en endimensjonal modell av en tredimensjonal "large eddy simulation", og kan dermed brukes til å teste "subgrid"-modeller.

Modeller som bruker fraktalinterpolering har blitt modifisert og utprøvd i simuleringer med grovt nettverk av Burgers' ligning med stokastisk kildeledd. Disse resultatene har blitt sammenlignet med resultater fra simuleringer med fint nettverk. Også lavoppløste simuleringer som benytter den dynamiske Smagorinsky-modellen og simuleringer uten "subgrid"-modell har blitt brukt som sammenligningsgrunnlag. I simuleringen uten "subgrid"-modell benyttes en diskretiseringsmetode som tilfører betydelige mengder numerisk dissipasjon.

Fraktalmodellene gir forholdsvis gode resultater, og de store skalaene ser ut til å stemme godt overens med de største skalaene i den høyoppløste simuleringen. Resultatene er imidlertid ikke bedre enn tilsvarende resultater for simuleringen som bruker Smagorinsky-modellen. Til tross for lovende resultater, ser det derfor ikke ut til å være noe som tyder på at fraktalmodellene yter bedre enn de tradisjonelle modellene. Også den lavoppløste simuleringen uten "subgrid"-modell gir gode resultater. Dette antyder at numerisk dissipasjon er en tilstrekkelig god "subgrid"-modell for endimensjonale problemer.

Det velkjente $\kappa^{-\frac{5}{3}}$-energyspektrumet finner man også for Burgers' ligning med stokastisk kildeledd. Høyereordens statistiske parametre er derimot veldig forskjellig for Burgers' ligning, grunnet de karakteristiske støtene, og det er dermed ikke sikkert at Burgers' ligning med stokastisk kildeledd er en spesielt god modelligning for turbulens. Det ser heller ikke ut til at kompleksiteten i tredimensjonal "subgrid"-modellering er spesielt godt ivaretatt i én dimensjon.

Contents

Chapter 1

Introduction

In most engineering applications and in nature, flows are turbulent. Because turbulent flow problems are so complex, they can rarely be solved directly, and models are required. This report deals with the use of fractals to model turbulence, and this chapter gives an introduction to the topics addressed in the rest of the report.

1.1   Background

The governing equations for both laminar and turbulent flow are the Navier-Stokes equations. The Navier-Stokes equations can be solved directly without modelling in both cases, but for turbulent flow this is very time consuming. To get reasonable solutions to the problem, one is therefore often required to simplify. The two most common ways of simplifying the turbulence equations are temporal averaging and spatial filtering, leading to the Reynolds-averaged Navier-Stokes equations and the large eddy simulation equations, respectively. In both cases models are required to close the equations.

For large eddy simulations the type of models required to close the equations are known as subgrid models, because they model the scales that are smaller than the grid size. The idea is then to solve the larger scales and create a model that represents the effect the small scales have on the larger scales.

It was first suggested by Mandelbrot (1974) and Mandelbrot (1975) that several aspects of turbulence could be described as fractal, and this proposition led to a large number of scientific papers reporting similar

observations. Many of the earlier papers on fractals and turbulence are
presented by Sreenivasan (1991). In recent years it has been suggested
that fractals could be used as a method for subgrid closure for large
eddy simulations. Scotti & Meneveau (1999) proposed that the fractal
interpolation technique could be used to model the unresolved scales, and
the simulations showed intriguing results.

Because also large eddy simulations are very time consuming, it can
sometimes be useful to study a simplified system instead of the full three-
dimensional large eddy simulation equations. Chekhlov & Yakhot (1995a)
showed that simulations of the stochastically forced Burgers equation
shared similar features with the three-dimensional Navier-Stokes equations.
Based on these results, Scotti & Meneveau (1999) chose to use the
stochastically forced Burgers equation as a model equation, when testing
the performance of a fractal subgrid model.

1.2   Objectives

The principal objective for this project is to study the use of fractals for
subgrid modelling. To do this, the stochastically forced Burgers equation
is used as a model equation for turbulence. The Burgers equation allows
simple experimentation while still sharing some of the characteristic features
of the Navier-Stokes equations. The fractal models are also compared with
more conventional subgrid models.

In order to assess the performance of the subgrid models, low resolution
solutions to the stochastically forced Burgers equation with subgrid
modelling is compared with results from high resolution simulations of the
stochastically forced Burgers equation. This means that the results of the
high resolution simulations first have to be validated by earlier published
results. The finite volume method is commonly used in computational fluid
dynamics and is used for solving the stochastically forced Burgers equation.

The stochastically forced Burgers equation is used as a model for the
Navier-Stokes equations. The ambition is that the observations from the
use of the Burgers equation in one way or another can also be applicable
to the Navier-Stokes equations. The degree of applicability and relevance
is however highly dependent upon how well the solutions to the Burgers
equation resemble real turbulence.

1.3 Overview

Many different topics are treated in the report, each organised in a separate chapter. A brief summary of each chapter is given here to provide an overview of the rest of the report.

1.3.1 Chapter 2

Chapter 2 is called "The non-linear diffusion equation" and presents the Burgers equation, the equation studied for the rest of the report. Exact analytical solutions, to be later used when testing numerical methods, are developed.

1.3.2 Chapter 3

Chapter 3 is called "Fractals and fractal interpolation" and introduces the fractal theory used in the fractal subgrid model that is presented in chapter 7. An informal description of the concept of multifractality is provided, and the fractal interpolation technique is presented. The analytical expressions that are used for the fractal subgrid model are derived here.

1.3.3 Chapter 4

Chapter 4 is called "The finite volume method for the Burgers equation" and introduces the numerical methods used for discretising the Burgers equation. The numerical schemes are tested by comparing the results with the exact solutions derived in chapter 2.

1.3.4 Chapter 5

Chapter 5 is called "The Burgers equation and turbulence" and contains a description of solutions to the stochastically forced Burgers equation. The numerical schemes presented in chapter 4 are tested for the stochastically forced Burgers equation, and high resolution reference results are presented and discussed.

1.3.5 Chapter 6

Chapter 6 is called "Modelling turbulence" and introduces the different types of turbulence models used to obtain approximate solutions to the

Navier-Stokes equations.   The difference between the time averaging approach and the spatial filtering approach is explained. A description of how these models can be used for the stochastically forced Burgers equation is provided at the end of the chapter.

1.3.6   Chapter 7

Chapter 7 is called "A fractal subgrid model for the stochastically forced Burgers equation" and presents two different versions of a multifractal subgrid model developed using the fractal interpolation technique.

1.3.7   Chapter 8

Chapter 8 is called "Results" and presents the most important results obtained when testing the fractal subgrid models from chapter 7. Both their ability to reproduce the actual subgrid stress and their performance in actual simulations are tested.

1.3.8   Chapter 9

Chapter 9 is called "Conclusion" and sums up the most important results and what we might conclude from these results.

1.3.9   Appendix A

Appendix A is called "Statistical treatment of turbulence" and introduces basic statistical concepts used in turbulence research.

1.3.10   Appendix B

Appendix B is called "Fractal geometry" and gives an introduction to basic concepts in fractal geometry.

1.3.11   Appendix C

Appendix C is called "Programming" and presents the program created to solve the stochastically forced Burgers equation.

1.3.12   Appendix D

Appendix D is called "A computational study of Burgers turbulence" and contains an article for the proceedings at the MekIT'11 conference.

Chapter 2

The non-linear diffusion equation

The chapter covers the non-linear diffusion equation, commonly called the Burgers equation, analytical solutions and applications. Analytical solutions of the Burgers equation are covered by Burgers (1974), which is the main reference used for this chapter.

2.1 The Burgers equation

The Burgers equation, is a quasilinear parabolic partial differential equation in one-dimensional space and time. It was first suggested by Burgers (1948) as a model equation for studying turbulence. The Burgers equation,

$$\frac{\partial u}{\partial t} + \frac{\partial}{\partial x}\left(\frac{1}{2}u^2\right) = \nu\frac{\partial^2 u}{\partial x^2},\tag{2.1}$$

can be considered as a one-dimensional version of the Navier-Stokes equations without pressure gradient. It contains a time derivative, a convective term and a diffusive term. The Burgers equation describes a compressible flow, as only trivial incompressible flows exist in one dimension.

For convenience the equation will be considered non-dimensional. Then u is a non-dimensional velocity, x is a non-dimensional length and t is non-dimensional time. The diffusion coefficient ν is a non-dimensional kinematic viscosity, or inverse Reynolds number.

2.2   Analytical solutions

There are many different exact solutions to the Burgers equation, which make it especially well suited for testing numerical methods. When exact analytical solutions are available, it is easy to determine the accuracy of approximate numerical methods.

2.2.1   The inviscid Burgers equation

The inviscid Burgers equation is a one-dimensional scalar conservation law of the type

$$\frac{\partial u}{\partial t} + \frac{\partial f(u)}{\partial x} = 0, \tag{2.2}$$

where $f(u) = \frac{1}{2}u^2$. Along characteristic lines $x(t)$ with $\frac{dx}{dt} = u$, the inviscid Burgers equation is reduced to an ordinary differential equation

$$\frac{du}{dt} = \frac{\partial u}{\partial t} + \frac{dx}{dt}\frac{\partial u}{\partial x} = \frac{\partial u}{\partial t} + u\frac{\partial u}{\partial x} = 0, \tag{2.3}$$

and thus for initial condition $u_0(x) = u(x, 0)$ the exact solution is implicitly given as

$$u(x, t) = u_0(x - u(x, t)t). \tag{2.4}$$

The velocity u is constant along the characteristics determined by straight lines of slope $u_0(x)$.

2.2.2   The Riemann problem

An initial value problem for equation (2.2) with initial value

$$u(x, 0) = \begin{cases} u_L & \text{for } x < 0 \\ u_R & \text{for } x > 0 \end{cases} \tag{2.5}$$

is called a Riemann problem. For the Burgers equation two distinct solutions emerge depending on which of u_L and u_R is the largest.

For $u_L > u_R$ the solution is a shock propagating with a shock speed s that can be calculated from the Rankine-Hugoniot condition

$$s(u_R - u_L) = f(u_R) - f(u_L), \tag{2.6}$$

which gives the shock speed

$$s = \frac{1}{2}(u_L + u_R). \tag{2.7}$$
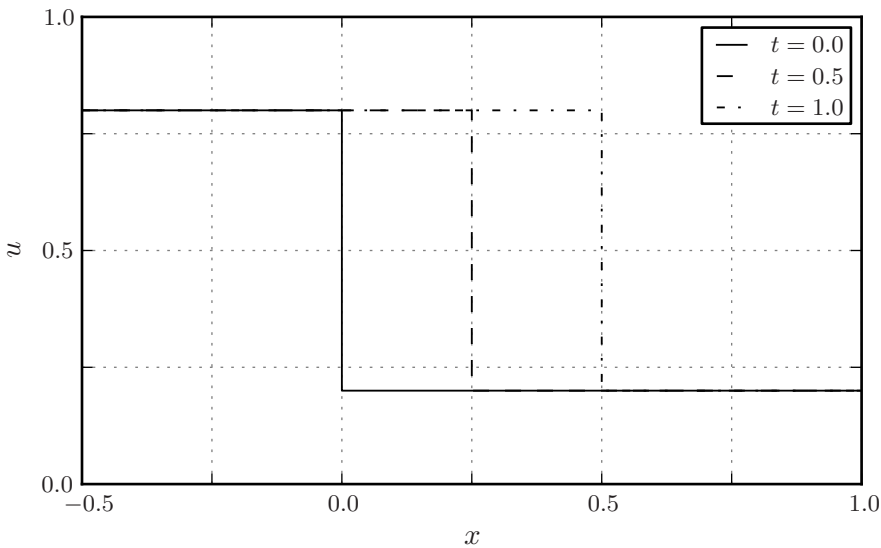
Figure 2.1: The shock in the solution of the Riemann problem propagates from left to right with speed s.

The exact solution of the Riemann problem is then

$$u(x,t) = \begin{cases} u_L & \text{for } x < st \\ u_R & \text{for } x > st \end{cases} \tag{2.8}$$

The solution to the Riemann problem for $u_L > u_R$ is seen in figure 2.1, where it is shown at three different times. The left side velocity is $u_L = 0.8$ and the right side velocity is $u_R = 0.2$, which gives a shock speed $s = 0.5$.

For $u_L < u_R$ the exact solution is a rarefaction wave

$$u(x,t) = \begin{cases} u_L & \text{for } x < u_L t \\ \frac{x}{t} & \text{for } u_L t < x < u_R t \\ u_R & \text{for } x > u_R t \end{cases} \tag{2.9}$$

An expansion shock is another possible solution to the equation, but is not correct because it is not a physical solution. The flux function is hyperbolic and so the Lax entropy condition requires that $f'(u_L) > s > f'(u_R)$ (Müller, 2010), which is not satisfied for the expansion shock. The solution to the Riemann problem for $u_L < u_R$ is seen in figure 2.2, at three different times for $u_L = 0.2$ and $u_R = 0.8$. The wave expansion is distinctly different from the shock solution in figure 2.1.
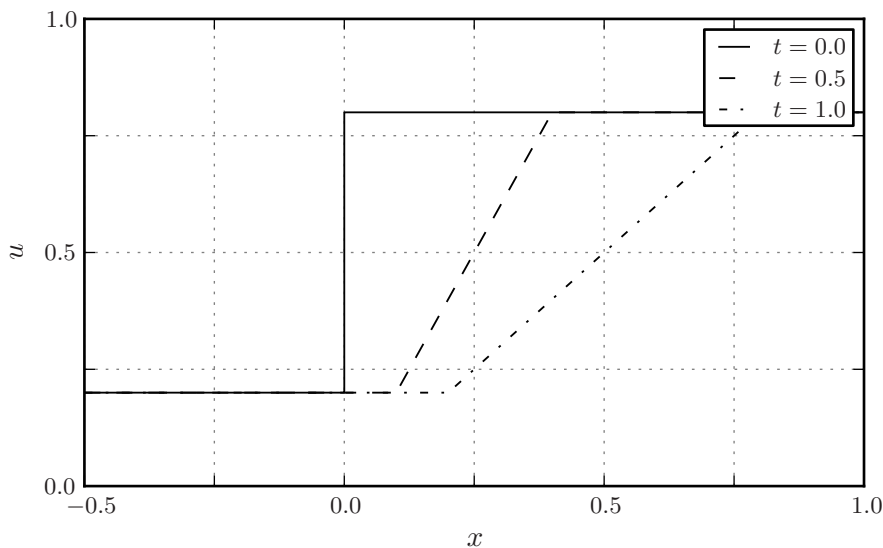
Figure 2.2: The rarefaction wave moves from left to right, and because the right side moves with higher velocity, the width of the wave increases.

2.2.3   Hopf-Cole transformation

In order to transform the quasi-linear Burgers equation into a linear partial differential equation, the Hopf-Cole transformation was introduced (Hopf, 1950; Cole, 1951). The transformation introduces the variable ϕ and sets u equal to

$$u = -2\nu \frac{1}{\phi} \frac{\partial \phi}{\partial x}. \tag{2.10}$$

When this is introduced into equation (2.1), we get, after cancellations,

$$\frac{1}{\phi} \frac{\partial \phi}{\partial x} \left(\frac{\partial \phi}{\partial x} - \nu \frac{\partial^2 \phi}{\partial x^2} \right) - \frac{\partial}{\partial x} \left(\frac{\partial \phi}{\partial x} - \nu \frac{\partial^2 \phi}{\partial x^2} \right) = 0. \tag{2.11}$$

It then follows that if ϕ is a solution of the equation

$$\frac{\partial \phi}{\partial x} = \nu \frac{\partial^2 \phi}{\partial x^2}, \tag{2.12}$$

then u is a solution of the Burgers equation. Equation (2.12) is called the heat equation and is a linear partial differential equation.
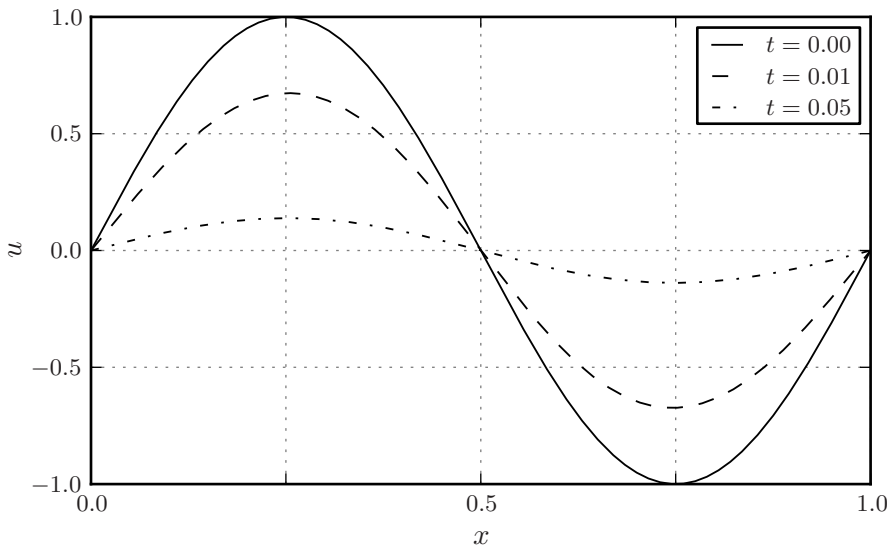
Figure 2.3: The exact solution for $u_0(x) = \sin(2\pi x)$ and $\nu = 1$ shows the sine wave amplitude decreasing in time.

A general solution of the heat equation for an infinite domain and $t > 0$ is

$$\phi = \frac{1}{2\sqrt{\pi\nu t}} \int_{-\infty}^{+\infty} \exp\left[-\frac{(x-\xi)^2}{4\nu t} + F(\xi)\right] d\xi, \qquad (2.13)$$

where $F(\xi)$ is an arbitrary function. When $t \to 0$ this yields

$$w_0(x) = \exp[F(x)], \qquad (2.14)$$

and for u with initial condition u_0

$$u_0(x) = -2\nu\frac{dF}{dx}. \qquad (2.15)$$

When the function F is determined from u_0, the solution is

$$\phi = \frac{1}{2\sqrt{\pi\nu t}} \int_{-\infty}^{+\infty} \exp\left[-\frac{(x-\xi)^2}{4\nu t} - \frac{1}{2\nu}\int_0^\xi u_0(\tilde{\xi})\,d\tilde{\xi}\right] d\xi, \qquad (2.16)$$

and for u

$$u(x,t) = \frac{\frac{1}{2\sqrt{\pi\nu t}} \int_{-\infty}^{+\infty} \frac{x-\xi}{t} \exp\left[-\frac{(x-\xi)^2}{4\nu t} - \frac{1}{2\nu}\int_0^\xi u_0(\tilde{\xi})\,d\tilde{\xi}\right] d\xi}{\frac{1}{2\sqrt{\pi\nu t}} \int_{-\infty}^{+\infty} \exp\left[-\frac{(x-\xi)^2}{4\nu t} - \frac{1}{2\nu}\int_0^\xi u_0(\tilde{\xi})\,d\tilde{\xi}\right] d\xi}. \qquad (2.17)$$
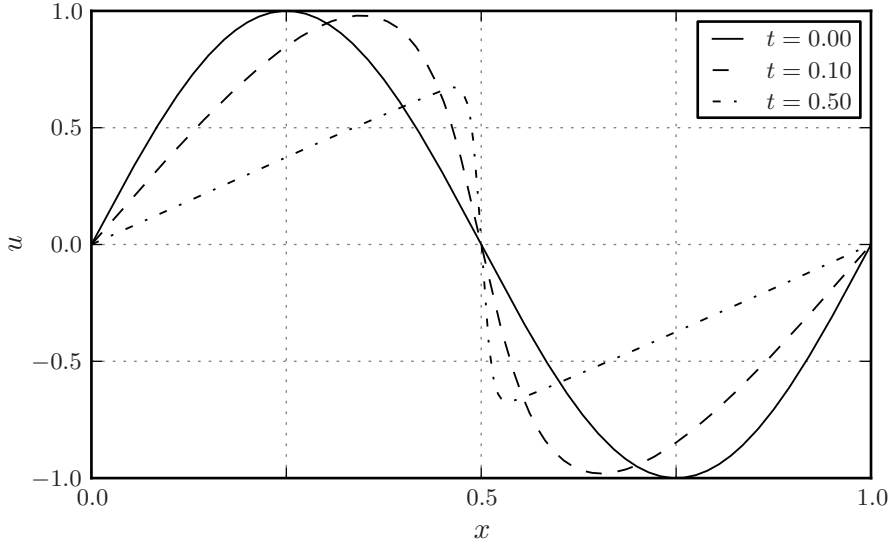
Figure 2.4: The exact solution for $u_0(x) = \sin(2\pi x)$ and $\nu = 0.005$ shows the sine wave developing into a shock.

Alternatively, the solution can be obtained using Fourier series. Consider the viscous Burgers equation with initial condition

$$u(x, 0) = u_0(x), \quad 0 < x < L \tag{2.18}$$

and Dirichlet boundary conditions

$$u(0, t) = u(L, t) = 0, \quad t > 0. \tag{2.19}$$

Using the Hopf-Cole transformation this problem is transformed to the heat equation (2.12) with initial condition

$$\phi(x, 0) = \phi_0(x) = \exp\left(-\frac{1}{2\nu} \int_0^\xi u_0(\tilde{\xi}) \, d\tilde{\xi}\right) \tag{2.20}$$

and Neumann boundary conditions

$$\left.\frac{\partial \phi}{\partial x}\right|_{x=0} = \left.\frac{\partial \phi}{\partial x}\right|_{x=L} = 0, \quad t > 0. \tag{2.21}$$
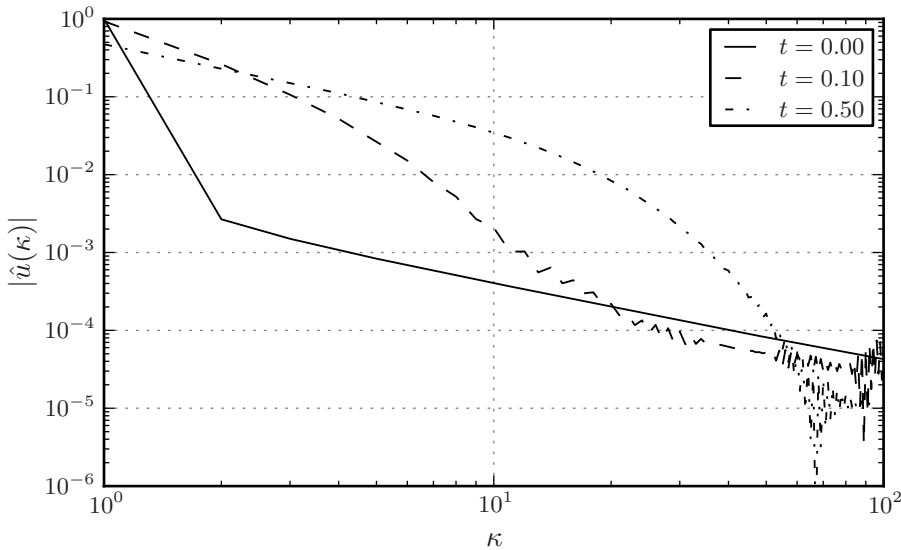
Figure 2.5: The amplitude spectrum of the exact solution for $u_0(x) = \sin(2\pi x)$ and $\nu = 0.005$ shows how the Burgers equation creates high wave number information.

Using separation of variables, the exact Fourier series solution to the heat equation problem outlined above is

$$\phi(x, t) = \sum_{n=0}^{\infty} A_n \cos\left(\frac{n\pi x}{L}\right) \exp\left(-\frac{\nu n^2 \pi^2}{L^2}t\right), \qquad (2.22)$$

where

$$A_0 = \frac{1}{L} \int_0^L \phi_0(x)\, dx \qquad (2.23)$$

$$A_n = \frac{2}{L} \int_0^L \phi_0(x) \cos\left(\frac{n\pi x}{L}\right)\, dx. \qquad (2.24)$$

Then the solution to the corresponding Burgers equation problem is

$$u(x, t) = \frac{2\pi\nu}{L} \frac{\sum_{n=1}^{\infty} A_n n \sin\left(\frac{n\pi x}{L}\right) \exp\left(-\frac{\nu n^2 \pi^2}{L^2}t\right)}{A_0 + \sum_{n=1}^{\infty} A_n \cos\left(\frac{n\pi x}{L}\right) \exp\left(-\frac{\nu n^2 \pi^2}{L^2}t\right)}, \qquad (2.25)$$

with coefficients $\{A_n : n = 0, 1, \ldots\}$ defined in equations (2.23)–(2.24).

Two examples of exact solutions to the viscous Burgers equation are shown in figure 2.3 and 2.4. Figure 2.3 shows the solution for $u_0(x) = \sin(2\pi x)$ and $\nu = 1$. The high viscosity ensures a rapid decrease in amplitude. Figure 2.4 shows the solution for equal initial condition but with viscosity $\nu = 0.05$. The left part of the sine wave surpasses the right part and a shock-like sharp gradient develops.

Figure 2.5 shows the amplitude spectrum of the velocity in figure 2.3. The initial condition is a sine wave and should have an zero amplitude for all other wave numbers than $\kappa = 1$. The amplitude spectrum in the figure has non-zero values for larger wave numbers due to numerical inaccuracy. It is clear that the later samples ($t = 0.1$ and $t = 0.5$) contain more high wave number information. This shows how the Burgers equation creates smaller scales than those included in the initial condition. The transport of energy from large to smaller scales is one of the characteristics that the dynamics of the Burgers equation shares with turbulence.

2.3   Applications

The Burgers equation is a nonlinear wave equation, and has found applications in nonlinear acoustics and other wave problems. A review is found in Gurbatov *et al.* (1991). Other applications include cosmology, condensed matter and statistical physics, and also vehicular traffic. This is elaborated on in Frisch & Bec (2001) and references therein.

A common usage of the Burgers equation is as a testing ground for the three-dimensional Navier-Stokes equation, both with regards to testing numerical methods and studying the physics. Because the terms in the Burgers equation are similar to those in the Navier-Stokes equations, new numerical methods can typically be tested for the Burgers equation, with the added convenience of having exact solutions.

Even though the Burgers equation was initially thought to be a model equation for turbulence, the standard Burgers equation has little to do with turbulence. As will be elaborated later, the addition of a stochastic element can make the Burgers equation more relevant for turbulence.

Chapter 3

Fractals and fractal interpolation

The objective of this chapter chapter is to give an introduction to multifractal theory and the fractal interpolation technique. The theory builds on the basic fractal theory described in appendix B.

Multifractals are also covered briefly by Falconer (2003) and Schroeder (1991), and some of the information comes from papers, cited when appropriate. The main references on iterated function systems and fractal interpolation are Falconer (2003), Barnsley & Rising (1993, chapter VI) and Barnsley (1986).

3.1 Multifractals

The fractals mentioned in appendix B are characterised by a single parameter known as the fractal dimension. This dimension describes the scaling or self-similar properties of the geometry, and contains in its simplicity a lot of information. Such fractals are known as monofractals. There are, however, many phenomena in nature that require a scaling description with several scaling exponents, and thus the theory of multifractals emerged.

Figure 3.1 shows the SGS stress in a solution to the stochastically forced Burgers equation, as presented in chapter 5. It is obvious that the stress is highly non-uniform and intermittent. If a particular measure has a Gaussian probability distribution, then the process is completely described by the mean and variance of the distribution. Several other
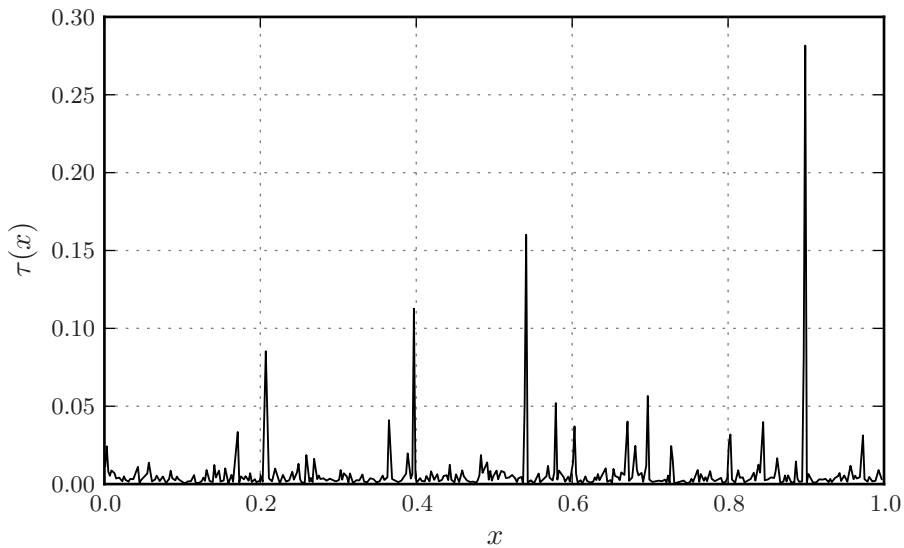
Figure 3.1: Plotted subgrid scale stress showing multifractal features

common probability distributions are completely described by a few low-order moments. For measures like the SGS stress in figure 3.1, the lower order moments reveal little about the true nature of the process.

To describe highly intermittent measures, the concept of multifractality is particularly well suited. The idea of a multifractal can be illustrated with a multiplicative cascade, a process that distributes the measure at one scale unequally to the next smaller scales. When the measure is unequally divided among the offsprings, and this process is repeated the measure becomes increasingly unevenly distributed. This process is illustrated in figure 3.2, where the measure at a given scale is divided into two parts with 70% to the right and 30% to the left, after 1, 2 and 10 partitions. The distribution after 10 steps begins to resemble the subgrid stress in figure 3.1, but the real process is much more random. If the rule determining the partitioning of the measure at each step is similar or equal for all steps in the process, then scale-similarity is expected.
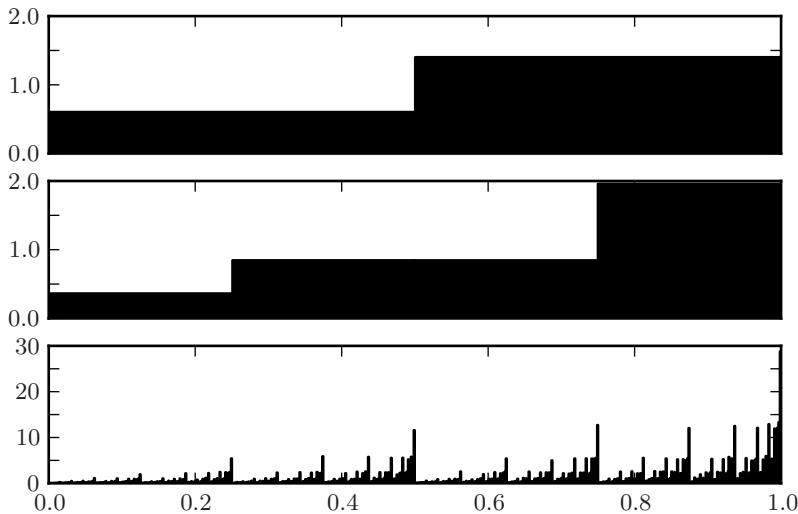
Figure 3.2: Multiplicative cascade where each step involves distributing 70% of the measure to the right side and 30% to the left

3.1.1   Structure functions

Using the definition of statistical moment (appendix A), a useful concept called a structure function can be defined.

Definition 3.1. *The longitudinal structure function of order p is defined as*

$$S_p(r) \equiv \langle [u(x+r) - u(x)]^p \rangle, \tag{3.1}$$

where x is the position and r is the spatial increment.

Using the ergodicity theorem (theorem A) the sample averages can be replaced by time averages and the structure functions computed as

$$S_p(r) = \overline{|u(x+r) - u(x)|^p}, \tag{3.2}$$

where the absolute value is taken to avoid cancellations for non-even p.

For many different phenomena the structure functions scale as power laws, i.e.

$$S_p(r) \sim r^{\zeta_p}, \tag{3.3}$$

where ζ_p are the structure function exponents, which will be shown to be closely connected with the fractal description.

3.1.2   The multifractal spectrum

Multifractals are typically characterised with what is known as a multifractal spectrum, also called a singularity spectrum. The concept of a multifractal spectrum is not that intuitive and will be introduced here rather informally, broadly following Sreenivasan (1991). For formal proofs and derivations see Falconer (2003, chapter 17) and references therein.

Lets imagine that the total energy dissipation in a certain region of size r is E_r. Following the logic of a box-counting algorithm the total integrated dissipation E_r in a box of size r is expressed as

$$\frac{E_r}{E_L} \sim \left(\frac{r}{L}\right)^{\beta} ,$$
(3.4)

where L is a characteristic large scale. The exponent β is a local scaling exponent and will depend on the position of the box. This is a reflection of the fact that multifractal scaling is a local phenomenon. One can then imagine the measure consisting of infinitely many sets of constant scaling exponent β that are intertwined. Each of these sets has a fractal dimension $f(\beta)$, describing the geometry of the particular set that has a scaling exponent equal to β. The function $f(\beta)$ is known as the singularity spectrum, or multifractal spectrum.

Another approach to characterising the multiplicative measure is by using moment exponents $\tau(q)$. The exponents are implicitly defined through the relation

$$\sum E_r^q \sim E_L^q \left(\frac{r}{L}\right)^{\tau(q)} .$$
(3.5)

For $q > 0$ the major contribution will be from increasingly larger peaks as q is increased. Thus the parameter q will accentuate peaks of a certain size, and $\tau(q)$ is the corresponding scaling exponent. This description is linked to what is called the generalised dimension defined as

$$D_q = \frac{\tau(q)}{(q-1)}.$$
(3.6)

The dimension D_0 corresponds to the regular fractal dimension of the support of the measure. The two different scaling descriptions presented here ($f(\beta)$ and $\tau(q)$) are linked through the Legendre-transform relation (see e.g. Falconer (2003)), and are equivalent. Both methods can be said to describe the strengths of singularities and the dimension of the sets they are distributed on. A thorough treatise of the multifractal formalism and

how to determine the scaling spectra was given by Jaffard (1997a) and
Jaffard (1997b).

Determining the multifractal spectrum is not the topic of this report,
rather multifractal theory has principal interest in its relation to the
structure function components and the use to determine the parameters
in the fractal interpolation technique. It was shown by Meneveau &
Sreenivasan (1987) that the structure function scaling exponents ζ_p were
related to the generalised dimension D_q as

$$\zeta_p = \left(\frac{p}{3} - 1\right) D_{p/3} + 1. \tag{3.7}$$

3.1.3 Multifractals and turbulence

The idea of a multiplicative cascade is very similar to the notion of an
energy cascade in turbulence. Richardson (1922) presented the idea of
eddies transferring their energy to smaller eddies in much the same way as
for each step in the multiplicative cascade the measure is divided among the
offsprings. This has inevitably led to the multifractal studies of turbulence
being quite popular. Early studies of multifractality in turbulence were
presented in the review by Sreenivasan (1991).

Kolmogorov's hypothesis of global scale invariance in the inertial range
predicts that the structure function exponents follow the linear relation
$\zeta_p = \frac{p}{3}$ over inertial range separations. Deviations from this linear relation
suggest inertial range intermittency, and this is still an unresolved issue in
turbulence research.

3.2 The fractal geometry of graphs

Many different phenomena of interest, display fractal features when plotted
as functions of time. Examples include stock prices, reservoir levels,
population data, measurements of brain-waves and heart beats, and velocity
or pressure traces in turbulent flow.

There are also examples of graphs of functions that are fractal, and it is
possible for a continuous function to be so irregular that it has a dimension
strictly greater than 1. Perhaps the most well-known example of this is the
function

$$f(t) = \sum_{k=1}^{\infty} \lambda^{(s-2)k} \sin(\lambda^k t), \tag{3.8}$$

where $1 < s < 2$ and $\lambda > 1$. The function is called the Weierstrass function, and its graph is continuous everywhere although nowhere differentiable. The graph is a strictly self-similar fractal and has a fractal dimension equal to s.

The fractal dimension of a graph can be determined by using a box-counting dimension as for more general geometries, but there are other simpler ways of finding the dimension. These methods use the relation between the fractal dimension and other common methods used to characterise graphs, such as structure functions and power spectra.

A signal with a power spectrum proportional to $1/\kappa^\alpha$, where κ is the wavenumber is expected to have a graph of dimension $\frac{1}{2}(5-\alpha)$ for $1 < \alpha < 3$. The dimension can also be determined from the second order structure function, which is expected to scale as $S_2(r) \sim r^{(\alpha-1)}$.

3.3   The fractal interpolation technique

From an experiment or a numerical simulation, the resulting data set $\{(x_i, y_i) : i = 0, 1, 2, \ldots, N\}$ is given. To analyse this data set it is common to use elements from Euclidian geometry and elementary functions such as sine, cosine and polynomials. A graphical representation might be used and elementary functions fitted to different sections of the graph.

N is a positive integer, $x_{i-1} < x_i \forall i$ and $y_i = y(x_i)$. In order to estimate a value for $y(x)$ for $x_i < x < x_{i+1}$ and interpolation function f, such that $f(x_i) = y_i \forall i$ might be used. The typical interpolation functions consist of piecewise linear functions, polynomials and splines. While these functions are well suited for smooth curves, they might not be well suited for highly irregular ones. In order to devise an interpolation function for highly irregular, and assumed somewhat self-similar curves, the fractal interpolation technique (FIT) was introduced (Barnsley, 1986).

3.3.1   Iterated function systems

Many fractals consist of parts that are similar to or resemble the whole geometry. Iterated function systems use this property to define the fractals with a simple iterative mapping procedure.

Let F be a closed subset of $\mathbb{R}^n$ and $w_n : F \to F$ for $n \in \{1, 2 \ldots, N\}$ be a continuous mapping. Then a finite collection $\{w_n : n = 1, 2, \ldots, N\}$ is termed an iterated function system (IFS) and has an attractor G defined

as

$$G = W(G) = \bigcup_n w_n(G). \tag{3.9}$$

The attractor of an IFS is usually fractal.

If for some $0 \leq s < 1$ and for all n

$$|w_n(x) - w_n(y)| \leq |x - y|, \quad \forall\, x, y \in F, \tag{3.10}$$

where $|\cdot|$ is the Euclidian distance, then w is called a contraction mapping, the IFS is called hyperbolic and the attractor G is the unique attractor defined by

$$G = \lim_{m \to \infty} W^{(m)}(G) = \lim_{m \to \infty} W(W(\cdots W(x)\cdots)). \tag{3.11}$$

An example of an IFS is the collection of the two contraction mappings $w_1 = \frac{1}{3}x$ and $w_2 = \frac{1}{3}x + \frac{2}{3}$. If F is the interval $[0, 1]$ then w_1 creates a smaller copy of F on the interval $\left[0, \frac{1}{3}\right]$ and w_2 creates a copy of F on $\left[\frac{2}{3}, 1\right]$. If this process is repeated an infinite number of times, the middle-third Cantor set emerges (see appendix B.3.1). Thus the middle-third Cantor set is the attractor of the IFS $\{w_1, w_2\}$.

The mappings w_1 and w_2 are examples of affine transformations. Affine transformations are defined as $w(x) = T(x) + a$, where T is a non-singular linear transformation and a is a point in $\mathbb{R}^n$. An affine transformation can be thought of as a shear transformation in terms of fluid dynamics nomenclature.

3.3.2 A fractal interpolation function

Given the set of data $\{(x_i, y_i) \in \mathbb{R}^2 : i = 0, 1, 2, \ldots, N\}$, where $x_0 < x_1 < x_2 < \cdots < x_N$, an interpolation function for the data is a function $f : [x_0, x_N] \to \mathbb{R}$ such that

$$f(x_i) = y_i, \quad \text{for } i = 0, 1, 2, \ldots, N. \tag{3.12}$$

The fractal interpolation technique uses an interpolation function f whose graph $G = \{(x, f(x)) : x \in [x_0, x_N]\}$ is an attractor of an IFS. These functions will be referred to as fractal interpolation functions, as the Hausdorff dimension of G often is non-integer. The interpolation function f will then be continuous but not differentiable.

The IFS whose attractor is the graph of the interpolation function is defined such that

$$w_n(x, y) = (L_n(x), F_n(x, y)).$$ (3.13)

Linear fractal interpolation functions are defined as those using affine maps

$$L_n(x) = a_n x + e_n,$$ (3.14)

$$F_n(x, y) = c_n x + d_n y + f_n,$$ (3.15)

or in matrix notation

$$w_n \begin{bmatrix} x \\ y \end{bmatrix} = \begin{bmatrix} a_n & 0 \\ c_n & d_n \end{bmatrix} \begin{bmatrix} x \\ y \end{bmatrix} + \begin{bmatrix} e_n \\ f_n \end{bmatrix}.$$ (3.16)

The constraints for these functions are

$$w_n \begin{bmatrix} x_0 \\ y_0 \end{bmatrix} = \begin{bmatrix} x_{n-1} \\ y_{n-1} \end{bmatrix},$$ (3.17)

and

$$w_n \begin{bmatrix} x_N \\ y_N \end{bmatrix} = \begin{bmatrix} x_n \\ y_n \end{bmatrix},$$ (3.18)

for all $n = 1, 2, \ldots, N$. This yields the following coefficients:

$$a_n = \frac{(x_n - x_{n-1})}{(x_N - x_0)},$$ (3.19)

$$e_n = \frac{(x_N x_{n-1} - x_0 x_n)}{(x_N - x_0)},$$ (3.20)

$$c_n = \frac{(y_n - y_{n-1})}{(x_N - x_0)} - d_n \frac{(y_N - y_0)}{(x_N - x_0)},$$ (3.21)

$$f_n = \frac{(x_N y_{n-1} - x_0 y_n)}{(x_N - x_0)} - d_n \frac{(x_N y_0 - x_0 y_N)}{(x_N - x_0)},$$ (3.22)

where d_n are the only remaining free parameters. The coefficients d_n are called vertical stretching factors because they determine how much the affine mapping stretches the original data in the vertical direction. A more general class of IFS is defined by

$$L_n(x) = a_n x + e_n$$ (3.23)

$$F_n(x, y) = d_n y + q_n(x), \tag{3.24}$$

where q_n can be used to fix the approximate general shape of the interpolation function. In order to be able to calculate the integrals required here, the interpolation will be limited to linear fractal interpolation functions.

Definition 3.2. *A linear fractal interpolation function on the data* $\{(x_i, y_i) \in \mathbb{R}^2 : i = 0, 1, 2, \ldots, N\}$ *is defined as the continuous function* $f : [x_0, x_N] \to \mathbb{R}$ *that is the attractor* G *of the IFS defined by* $\{w_n : n = 1, 2, \ldots, N\}$ *and equations (3.16), (3.19)–(3.22), with* d_n *as a free parameter.*

3.3.3 Integration of fractal interpolation functions

Using linear fractal interpolation functions, it will be shown how to explicitly calculate moment integrals of the type

$$f_{1,m} = \int x^m f(x)\, dx \tag{3.25}$$

and

$$f_{l,m} = \int x^m (f(x))^l \, dx \,. \tag{3.26}$$

Linearity is not a necessary requirement for the first integral, but it is for the second integral. Because also the second integral will be shown to be necessary when the fractal interpolation technique is applied, only linear fractal interpolation functions are considered. Given that the second integral (3.26) by definition also includes the first integral, only the solution to this integral will be developed.

For $I = [x_0, x_N]$ a fractal interpolation function $f : I \to \mathbb{R}$ is defined as before. If $L_n(x)$ are affine and the values of a_n are given by (3.19), the identity

$$\int_I H(x, f(x))\, dx = \sum_{n=1}^{N} a_n \int_I H(L_n(x), F_n(x, f(x)))\, dx \tag{3.27}$$

holds, where $H(x, f(x))$ is a function on the iterated function system. This identity makes it possible to calculate the specified integrals. The proof of this identity is given in Barnsley (1986), and will not be dwelled further on here.

For simplicity the integral

$$f_{1,0} = \int_I f(x)\,dx \tag{3.28}$$

will be considered first. Using equation (3.27) with $H(x,y) = y$, and $L_n(x), F_n(x, f(x))$ defined from equations (3.14)–(3.15) the integral can be rewritten as

$$f_{1,0} = \sum_{n=1}^{N} a_n \int_I F_n(x, f(x))\,dx = \sum_{n=1}^{N} a_n \int_I c_n x + d_n f(x) + f_n\,dx. \tag{3.29}$$

This can then be written as

$$f_{1,0} = \left(\sum_{n=1}^{N} a_n d_n\right) f_{1,0} + \sum_{n=1}^{N} a_n \int_I c_n x + f_n\,dx \tag{3.30}$$

which then gives

$$f_{1,0} = \frac{\sum_{n=1}^{N} a_n \int_I c_n x + f_n\,dx}{1 - \sum_{n=1}^{N} a_n d_n} \tag{3.31}$$

$$= \frac{\sum_{n=1}^{N} a_n (c_n f_{0,1} + f_n f_{0,0})}{1 - \sum_{n=1}^{N} a_n d_n}. \tag{3.32}$$

For $H(x,y) = x^m y^l$ and $L_n(x), F_n(x, f(x))$ given as before, the integral in equation (3.26) can be computed as

$$f_{l,m} = \sum_{n=1}^{N} a_n \int_I (a_n x + e_n)^m (c_n x + d_n f(x) + f_n)^l\,dx. \tag{3.33}$$

This can then be rewritten as

$$f_{l,m} = \sum_{p=0}^{l} \int_I (f(x))^p P_{l,m,p}(x)\,dx, \tag{3.34}$$

where $P_{l,m,p}(x)$ is a polynomial defined as

$$P_{l,m,p}(x) = \sum_{n=1}^{N} \binom{l}{p} a_n (c_n x + f_n)^{l-p} d_n^p (a_n x + e_n)^m \tag{3.35}$$

$$= \sum_{j=0}^{l+m-p} K(l, m, p, j) x^j. \tag{3.36}$$

From this and

$$K(l, m, l, m) = \sum_{n=1}^{N} a_n^{j+1} d_n^l \qquad (3.37)$$

it is obtained that

$$
\begin{aligned}
f_{l,m} = \Bigg(& \sum_{j=0}^{m-1} f_{l,j} \binom{m}{j} \sum_{n=1}^{N} a_n^{j+1} d_n e_n^{m-j} \\
& + \sum_{p=0}^{l-1} \sum_{j=0}^{l+m-p} K(l, m, p, j) f_{p,j} \Bigg) \Bigg/ \Bigg(1 - \sum_{n=1}^{N} a_n^{m+1} d_n^l \Bigg).
\end{aligned}
\qquad (3.38)
$$

By choosing $l = 1$ and $m = 0$, the expression is reduced to equation (3.32). For $l = 2$ and $m = 0$ the integral is

$$
\begin{aligned}
f_{2,0} = \Bigg(& \sum_{n=1}^{N} a_n (c_n^2 f_{0,2} + 2 c_n f_n f_{0,1} + f_n^2 f_{0,0} + 2 c_n d_n f_{1,1} \\
& + 2 d_n f_n f_{1,0}) \Bigg) \Bigg/ \Bigg(1 - \sum_{n=1}^{N} a_n d_n^2 \Bigg),
\end{aligned}
\qquad (3.39)
$$

where

$$
\begin{aligned}
f_{1,1} = \Bigg(& \sum_{n=1}^{N} a_n d_n e_n f_{1,0} + \sum_{n=1}^{N} a_n (a_n c_n f_{0,2} + c_n e_n f_{0,1} \\
& + a_n f_n f_{0,1} + e_n f_n f_{0,0}) \Bigg) \Bigg/ \Bigg(1 - \sum_{n=1}^{N} a_n^2 d_n \Bigg),
\end{aligned}
\qquad (3.40)
$$

and the computation of all $f_{0,m}$ are trivial. Thus a framework exists from which all $f_{l,m}$ can be computed.

3.3.4 The dimension of fractal interpolation functions

The fractal dimension of fractal interpolation functions can be determined using the following theorem.

Theorem 3.3. *Let an IFS described by equation 3.16, and with parameters determined by equations 3.19–3.22, be associated with the set of data $\{(x_i, y_i) : i = 0, 1, 2, \ldots, N\}$, for $N > 1$. The scaling factors d_n all obey*

$0 \leq d_n < 1$. Let G be the attractor of the IFS, so that it is the graph of the fractal interpolation function associated with the IFS. Then if

$$\sum_{n=1}^{N} |d_n| > 1 \qquad (3.41)$$

and the interpolation points are not all collinear, the fractal dimension D_F of the graph G is the solution to

$$\sum_{n=1}^{N} |d_n| a_n^{D_F-1} = 1. \qquad (3.42)$$

An informal demonstration of this theorem is found in Barnsley & Rising (1993, page 224–226).

For equally spaced interpolation points a_n is given by $a_n = \frac{1}{N}$ and using theorem 3.3 we get

$$D_F = 1 + \log_N \left(\sum_{n=1}^{N} |d_n| \right). \qquad (3.43)$$

This is in interesting formula, both in its simplicity, and the sole dependence on d_n. The fractal dimension of the graph is completely independent of the interpolation values.

With the introduction of the multifractal formalism it is possible to find a formula that provides a more general description of the scaling properties of the graph. An expression relating the scaling exponent spectrum to the stretching factors is

$$\zeta_p = 1 - \log_N \sum_{n=1}^{N} |d_n|^q, \qquad (3.44)$$

as shown by Basu *et al.* (2004*a*). Using the relation that $D_F = 2 - \zeta_1$ (see e.g. Davis *et al.*, 1994), equation 3.43 is recovered. If all d_n are equal ζ_p is a linear function of p and the interpolation is monoaffine. Otherwise, the interpolation is multiaffine.

Chapter 4

The finite volume method for the Burgers equation

The finite volume method (FVM) is presented and applied to the Burgers equation. Different temporal and spatial discretisation schemes are presented. The presentation broadly follows Müller (2010), Geurts (2004) and Versteeg & Malalasekera (2007).

4.1 The finite volume method

The finite volume method is a spatial discretisation method commonly used for computational fluid dynamics (CFD). The FVM is a popular approach as it has several convenient properties, such as geometric flexibility, discrete conservation and shock capturing capability. However, numerical analysis of FVM methods is much less developed than for finite difference and finite element methods, and it is more difficult to extend numerical schemes to higher order of accuracy.

The distinguishing feature of the FVM is that instead of directly approximating the partial derivatives in the equation, an integral formulation is considered. The viscous Burgers equation with a general volume force g can be written as

$$\frac{\partial u}{\partial t} + \frac{\partial}{\partial x}\left(\frac{1}{2}u^2\right) = \nu\frac{\partial^2 u}{\partial x^2} + g(x,t), \tag{4.1}$$

where the kinematic viscosity ν is constant. Integrating this equation over

a general volume V yields

$$\int_V \frac{\partial u}{\partial t}\, dV + \int_V \frac{\partial}{\partial x}\left(\frac{1}{2}u^2\right) dV = \int_V \nu \frac{\partial^2 u}{\partial x^2}\, dV + \int_V g(x,t)\, dV , \quad (4.2)$$

which, using Gauss' divergence theorem and Leibniz's rule, can be rewritten as

$$\frac{d}{dt}\int_V u\, dV + \int_{\partial V} \frac{1}{2}u^2 n_x\, dS = \int_{\partial V} \nu \frac{\partial u}{\partial x} n_x\, dS + \int_V g(x,t)\, dV , \quad (4.3)$$

where ∂V is the boundary of V and n_x is the x-component of the surface normal of ∂V.

If V has a constant cross-section in the y-z-plane and x goes from x_a to x_b, then the integral equation simplifies to

$$\Delta x \frac{d\hat{u}}{dt} + \left(\frac{1}{2}u^2\right)_b - \left(\frac{1}{2}u^2\right)_a = \left(\nu \frac{\partial u}{\partial x}\right)_b - \left(\nu \frac{\partial u}{\partial x}\right)_a + \Delta x\, \hat{g}, \quad (4.4)$$

where

$$\Delta x = x_b - x_a, \quad (4.5)$$

and $\hat{u}$ and $\hat{g}$ are cell-averages of u and g defined as

$$\hat{u} = \frac{1}{\Delta x}\int_{x_a}^{x_b} u\, dx \quad (4.6)$$

$$\hat{g} = \frac{1}{\Delta x}\int_{x_a}^{x_b} g\, dx . \quad (4.7)$$

To solve the Burgers equation, the domain is divided into NJ control volumes $\left[x_{j-\frac{1}{2}}, x_{j+\frac{1}{2}}\right]$, each satisfying equation (4.4). In the centre of each control volume the node x_i, where values are evaluated, is located. Each node j has a left neighbour $j-1$ and a right neighbour $j+1$. The cell-averaged values $\hat{u}$ and $\hat{g}$ are approximated by u_j and g_j, and the integral equation for control volume j is

$$\Delta x_j \frac{du_j}{dt} + \left(\frac{1}{2}u^2\right)_{j+\frac{1}{2}} - \left(\frac{1}{2}u^2\right)_{j-\frac{1}{2}} = \left(\nu \frac{\partial u}{\partial x}\right)_{j+\frac{1}{2}} - \left(\nu \frac{\partial u}{\partial x}\right)_{j-\frac{1}{2}} \quad (4.8)$$
$$+ \Delta x_j\, g_j.$$

This is no longer an exact equation, as the cell-averaged values are approximated by the known values in node x_i. The equation can be written symbolically as

$$\Delta x_j \frac{du_j}{dt} + f_{j+\frac{1}{2}} - f_{j-\frac{1}{2}} = diff_{j+\frac{1}{2}} - diff_{j-\frac{1}{2}} + \Delta x_j \, S\left(u_j, x_j, t\right), \qquad (4.9)$$

where f is a convective flux, $diff$ is a diffusive flux and S is the source term. These different types of terms in the equation need to be treated differently when they are approximated. The fluxes must be approximated at the cell faces using the known values in the nodes. The leftmost term in the equation is the time-dependent term which needs to be dealt with when the equation is integrated in time.

4.2 Discretising the diffusive flux

The diffusive fluxes can be approximated at the cell faces using normal finite difference discretisation. A second order central difference method yields

$$\left(\nu \frac{\partial u}{\partial x}\right)_{j-\frac{1}{2}} = \frac{u_j - u_{j-1}}{x_j - x_{j-1}}, \qquad (4.10)$$

$$\left(\nu \frac{\partial u}{\partial x}\right)_{j+\frac{1}{2}} = \frac{u_{j+1} - u_j}{x_{j+1} - x_j}. \qquad (4.11)$$

4.3 Discretising the convective flux

4.3.1 Central method

The central FVM approximates the convective flux at the cell faces by taking the arithmetic average of the adjacent flux values, i.e.

$$f_{j-\frac{1}{2}} = \frac{1}{2}\left(f_{j-1} + f_j\right), \qquad (4.12)$$

$$f_{j+\frac{1}{2}} = \frac{1}{2}\left(f_j + f_{j+1}\right). \qquad (4.13)$$

The central FVM is second order accurate for an equidistant grid, but will introduce oscillations at discontinuities. Therefore, the central FVM can only be used for well resolved smooth flow and is not suitable for the Burgers equation.

4.3.2   Upwind method

The central FVM does not contribute to numerical dissipation. In order
to deal with discontinuities and sharp gradients without oscillations, the
method should add numerical dissipation. A dissipation model is therefore
added to the central FVM.

The upwind FVM, also called Roe's approximate Riemann solver,
approximates the convective fluxes at the cell interfaces by solving a
Riemann problem at each interface. The upwind method is an approximate
Riemann solver, as opposed to Godunov's method, that exactly solves a
Riemann problem at each interface.

The upwind FVM prescribes the convective flux at $x_{i+\frac{1}{2}}$ as

$$
f_{j+\frac{1}{2}} = \begin{cases} f\left(u_L\right) & \text{if } a_{j+\frac{1}{2}} \geq 0 \\ f\left(u_R\right) & \text{if } a_{j+\frac{1}{2}} < 0 \end{cases} ,
\tag{4.14}
$$

where

$$
a_{j+\frac{1}{2}} = \begin{cases} \frac{f(u_R)-f(u_L)}{u_R-u_L} & \text{if } u_L \neq u_R \\ \left.\frac{df}{du}\right|_{u_L} & \text{if } u_L = u_R \end{cases} ,
\tag{4.15}
$$

and u_L and u_R are the velocities at the left and right side of the interface.
The numerical flux function can also be written as

$$
f_{j+\frac{1}{2}} = \frac{1}{2}\left[f\left(u_L\right) + f\left(u_R\right) - \left|a_{j+\frac{1}{2}}\right|\left(u_R - u_L\right)\right],
\tag{4.16}
$$

where it is apparent that the upwind method is a central method with an
added dissipation model. The velocities are assumed constant inside the
cells, and so u_L and u_R can be approximated by u_j and u_{j+1}. For the
Burgers equation the convective flux function then becomes

$$
f_{j+\frac{1}{2}} = \frac{1}{2}\left[\frac{1}{2}u_j^2 + \frac{1}{2}u_{j+1}^2 - \left|\frac{1}{2}\left(u_j + u_{j+1}\right)\right|\left(u_{j+1} - u_j\right)\right],
\tag{4.17}
$$

and similarly for $f_{j-\frac{1}{2}}$.

The upwind method predicts an unphysical expansion shock in cases
where the solution should be a rarefaction wave. This corresponds to a
decrease in total entropy (Geurts, 2004), which is not physically correct.
To avoid this, a certain amount of numerical viscosity can be added where
it is needed. This can be done by replacing $\left|a_{j+\frac{1}{2}}\right|$ with $Q(a_{j+\frac{1}{2}})$ defined by

$$
Q(a) = \begin{cases} |a| & \text{if } |a| > \delta \\ \delta & \text{if } |a| \leq \delta \end{cases} ,
\tag{4.18}
$$

where δ is a small problem specific positive constant. A possible choice of δ is to use

$$\delta = \max(f'(u_R) - f'(u_L), eps),\qquad(4.19)$$

where $eps = 2^{-53}$ is standard double precision machine epsilon.

The upwind FVM with constant cell reconstructions is first order accurate. An important property of the upwind method is that it is total variation diminishing (TVD). That is, the total variation defined as

$$TV\left(\boldsymbol{u}^n\right) = \sum_{i=-\infty}^{\infty} \left|u_j^n - u_{j-1}^n\right|\qquad(4.20)$$

does not increase from time step n to $n+1$, i.e.

$$TV\left(\boldsymbol{u}^n\right) \leq TV\left(\boldsymbol{u}^{n+1}\right).\qquad(4.21)$$

This ensures that oscillations do not occur at discontinuities, as they can for methods that are not TVD.

4.3.3 Local Lax-Friedrichs method

Another simple and robust method is the local Lax-Friedrichs method, also called the Rusanov method, which is a modification of the Lax-Friedrichs method. The flux function for the local Lax-Friedrichs method is

$$f_{j+\frac{1}{2}} = \frac{1}{2}\left[f\left(u_L\right) + f\left(u_R\right) - \max\left(\left|f'\left(u_L\right)\right|, \left|f'\left(u_R\right)\right|\right)\left(u_R - u_L\right)\right],\quad(4.22)$$

and when u_L and u_R are approximated by u_j and $u_{j+\frac{1}{2}}$ the method is first order accurate.

4.3.4 MUSCL interpolation

To extend the first order TVD methods to higher order of accuracy the MUSCL (Monotone Upwind-centred Schemes for Conservation Laws) interpolation method was developed (van Leer, 1974). Instead of assuming constant reconstruction inside the cells, the MUSCL technique applies a linear or quadratic reconstruction to approximate u_L and u_R in the flux functions.

To avoid loss of TVD property the slopes are limited near extrema using the minmod-limiter. The limiting reduces the accuracy to second order at extrema. The MUSCL interpolated values of u_L and u_R for flux $f_{j+\frac{1}{2}}$ are

$$u_L = u_j + \frac{1}{4} \left[(1 - \kappa)\Delta^+ u_j + (1 + \kappa)\Delta^- u_j \right] \qquad (4.23)$$

and

$$u_R = u_{j+1} - \frac{1}{4} \left[(1 - \kappa)\Delta^- u_{j+1} + (1 + \kappa)\Delta^+ u_{j+1} \right], \qquad (4.24)$$

where $\Delta^+ u$ and $\Delta^- u$ are the minmod-limited velocity differences

$$\Delta^+ u_j = \mathrm{minmod}\left(\Delta u_{j-\frac{1}{2}}, \beta \, \Delta u_{j+\frac{1}{2}} \right) \qquad (4.25)$$

and

$$\Delta^- u_j = \mathrm{minmod}\left(\Delta u_{j+\frac{1}{2}}, \beta \, \Delta u_{j-\frac{1}{2}} \right). \qquad (4.26)$$

The minmod limiter is defined as

$$\mathrm{minmod}(a, b) = \frac{1}{2}(\mathrm{sign}(a) + \mathrm{sign}(b)) \min(|a|, |b|). \qquad (4.27)$$

The MUSCL approach can be used to increase the order of accuracy of the first-order flux functions by inserting the interpolated u_L and u_R values into the flux function approximation expressions. For $\kappa = \frac{1}{3}$ the method is third order accurate in smooth regions of the flow, and a value of $\beta = \frac{2}{3}$ is recommended (Geurts, 2004).

4.4 Discretising sources

The source term in the equation can be approximated by a sum of a part that is independent of u_j and a linear function of u_j

$$S(u_j, x_j, t) = S_0(x_j, t) + S_j u_j. \qquad (4.28)$$

If S is not a linear function of u, then it has to be linearised.

4.5 Temporal discretisation

After introducing the approximations for the fluxes and the source term, the equation can be written as a system of ordinary differential equations (ODE)

$$\frac{d\boldsymbol{u}}{dt} = \boldsymbol{R}(\boldsymbol{u}), \qquad (4.29)$$

where $\boldsymbol{u}$ is the velocity vector and R is the vector of residuals. This system can be solved with different types of ODE solvers, and a popular class of solvers are the explicit Runge-Kutta methods.

4.5.1 Explicit Euler method

The simplest explicit Runge-Kutta method is the explicit Euler method, which is a first order explicit method. The algorithm for the explicit Euler method is

$$\boldsymbol{u}^{n+1} = \boldsymbol{u}^n + \Delta t\, \boldsymbol{R}(\boldsymbol{u^n}), \tag{4.30}$$

where $\boldsymbol{u}^{n+1}$ is the velocity vector for the new time step and $\boldsymbol{u}^n$ is the velocity vector for the old time step.

4.5.2 TVD Runge-Kutta

A third-order Runge-Kutta method that preserves the TVD property was developed by Gottlieb & Shu (1998). This is a three-stage method with the following algorithm

$$\begin{aligned}
\boldsymbol{u}^{(1)} &= \boldsymbol{u}^n + \Delta t\, \boldsymbol{R}(\boldsymbol{u^n}), \\
\boldsymbol{u}^{(2)} &= \tfrac{3}{4}\boldsymbol{u}^n + \tfrac{1}{4}\boldsymbol{u}^{(1)} + \tfrac{1}{4}\Delta t\, \boldsymbol{R}(\boldsymbol{u}^{(1)}), \\
\boldsymbol{u}^{n+1} &= \tfrac{1}{3}\boldsymbol{u}^n + \tfrac{2}{3}\boldsymbol{u}^{(2)} + \tfrac{2}{3}\Delta t\, \boldsymbol{R}(\boldsymbol{u}^{(2)}).
\end{aligned} \tag{4.31}$$

4.6 Stability analysis

An important concern when choosing the numerical method for a particular partial differential equation is stability. In order to get reliable results the simulation must be stable and not diverge. For explicit methods in particular one must abide to a strict time step criterion to ensure stability. Because of this, stability analysis is an important part of the study of numerical methods for solving partial differential equations.

The most used form of stability analysis is the von Neumann analysis. This method is involves inserting a Fourier mode in the discretised equation and requires that the amplitude is non-increasing. In von Neumann analysis the non-linear equation is locally linearised and checked for stability.

Two non-dimensional numbers are revealed when studying stability analysis, the von Neumann number

$$r = \frac{\nu\,\Delta t}{\Delta x^{\,2}}, \tag{4.32}$$

and the Courant number

$$C = \frac{|u|\,\Delta t}{\Delta x},\tag{4.33}$$

where u is the locally linearised velocity. The maximum Courant number C_{max} uses the maximum velocity in the initial condition.

For the inviscid Burgers equation discretised using the upwind method and integrated with the explicit Euler method, the stability condition reads

$$C_{max} = \max_{j}\frac{|u_j|\,\Delta t}{\Delta x} \le 1,\tag{4.34}$$

and for the viscous Burgers equation using central discretisation for the diffusive flux the stability condition is

$$C_{max} + 2r \le 1.\tag{4.35}$$

4.7 Numerical accuracy

In order to assess the accuracy of different numerical methods, one can compare the results of these methods with a reference. For some problems exact numerical solutions of the Burgers equation exist and can provide such a reference. The exact solutions used here are discussed in more detail in chapter 2.

A useful method when comparing different discretisation schemes is to compute the Euclidian norm of the error. The discrete Euclidian norm, or L_2-norm, of the error is defined as

$$\|\boldsymbol{u} - \boldsymbol{u}_{exact}\| = \sqrt{\frac{1}{NJ}\sum_{j=1}^{NI}(u_j(t) - u_{exact}(x_j,t))^2}.\tag{4.36}$$

If it is assumed that the error in the calculation can be expressed as

$$error(\,\Delta x\,) = c\,\Delta x^{\,p},\tag{4.37}$$

where c is constant, then the convergence rate p can be calculated as

$$p = \frac{\log\left(error(\,\Delta x\,)/error(\frac{\Delta x}{2})\right)}{\log(2)}.\tag{4.38}$$

The range in which c is constant is called the asymptotic range of convergence. The convergence rate specifies the order of accuracy of the computation and an n-order method should have a convergence rate p equal to n.
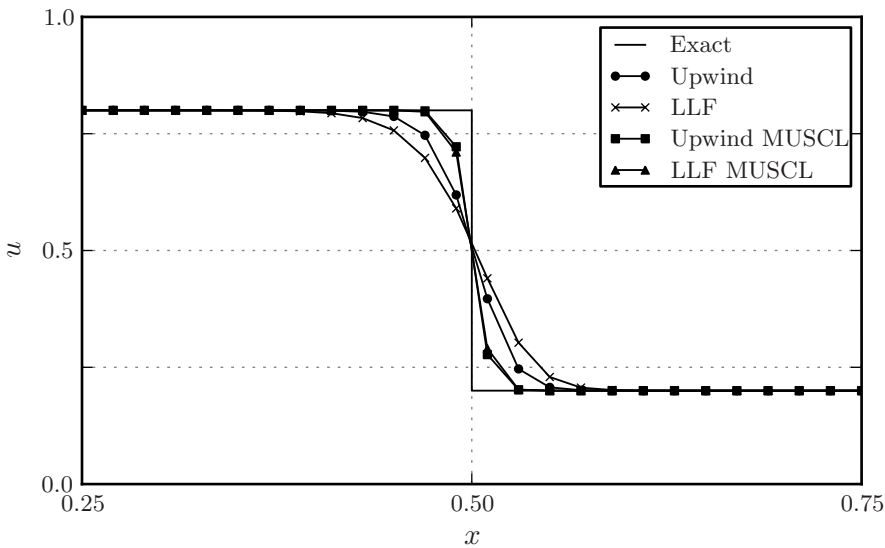
Figure 4.1: Numerical solution to the Riemann shock problem for four different convective flux functions for $t = 1.0$.

4.7.1 The inviscid Burgers equation

The Riemann problem with $u_L > u_R$ is solved using an FVM code with explicit Euler time integration. The convective flux functions tested are the upwind method and the local Lax-Friedrichs method (LLF), both with and without MUSCL interpolation. The central method was tested and discarded, due to instability causing infinite values (as expected). Spatial resolution was 75 cells between -0.5 and 1.0, the time step was 0.01 and the time of comparison was $t = 1.0$, for all methods. This corresponds to a maximum Courant number of $C = 0.4$. The explicit Euler method is used for temporal integration.

The MUSCL interpolation method is used with limiter, as described earlier in the chapter. Both MUSCL simulations use the suggested values for κ and β. The upwind method is equipped with the entropy fix suggested in equations (4.18) and (4.19).

The resulting velocity can be seen in figure 4.1. The shock is placed correctly for all methods, suggesting little dispersion error. There are no oscillations for any of the methods, but all of them suffer to some degree
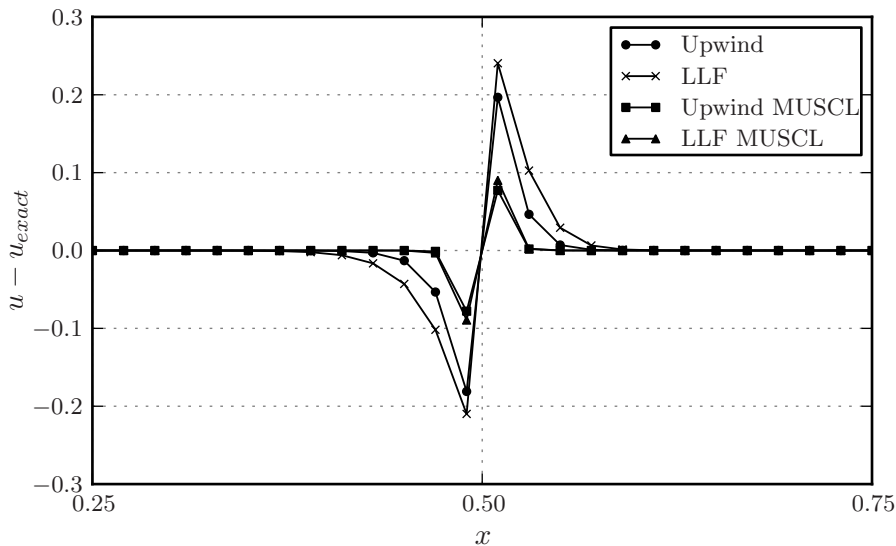
Figure 4.2: Difference between numerical solution of Riemann shock problem and analytical solution clearly shows difference in accuracy.

from dissipation error. The shock is smoothened by numerical dissipation for all four methods, but to a lesser degree for the two methods using MUSCL due to the higher order of accuracy.

The difference between the numerical simulation and the exact solution is plotted in figure 4.2. The accuracy of the methods is more easily assessed by looking at the difference, than the actual value. Except for the higher accuracy of methods using MUSCL, another observation is that the upwind method is slightly more accurate than the local Lax-Friedrichs method.

Figure 4.2 shows a velocity error that appears perfectly antisymmetric around the shock. The implication of this is that there is no trailing error caused by the shock.

Figure 4.3 shows the Euclidian norm of the error for different grid resolutions. The difference in accuracy is even clearer here, than in the earlier plots. All methods show a reduction in error for increased number of grid cells, but the convergence rate is only 0.5 for all the different flux functions. The value of c in equation (4.37) is constant, suggesting an asymptotic range of convergence. For this particular problem the higher order methods exhibit an equally low convergence rate as the first
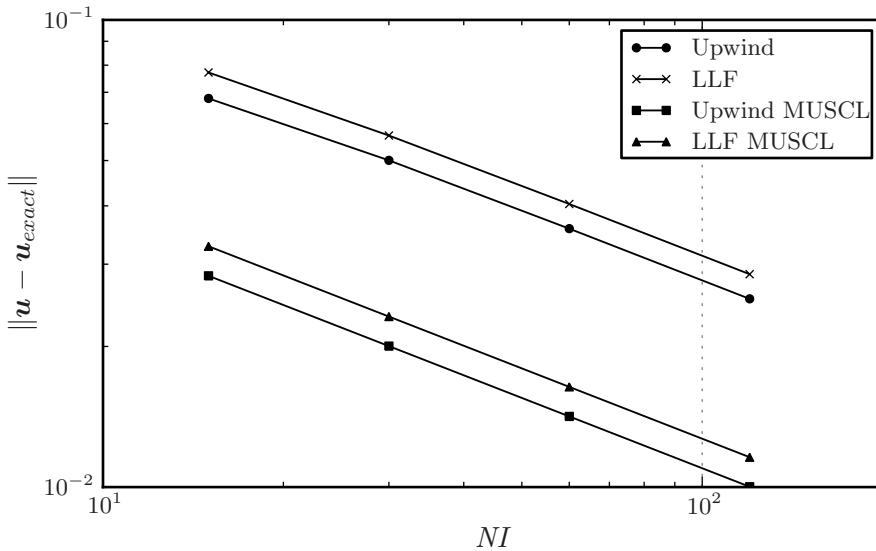
Figure 4.3: The Euclidian norm of the error for the Riemann shock problem shows a positive convergence rate of 0.5 for all flux functions, at constant Courant number $C = 0.4$.

order methods. All methods also show lower convergence rate than their theoretical order of accuracy. The estimated order of accuracy of the numerical methods is based on Taylor expansion, and thus smoothness is assumed. The fact that the discontinuous Riemann problem does not follow the theoretical order of accuracy, should therefore not be surprising.

4.7.2 The viscous Burgers equation

For comparison with the Hopf-Cole solution, the viscous Burgers equation has been solved numerically for initial condition $u_0 = \sin(2\pi x)$ and viscosity $\nu = 0.005$. The solution is compared with the exact solution at time $t = 0.5$ for the upwind method and the local Lax-Friedrichs method, both with and without MUSCL interpolation. The explicit Euler method is used for temporal integration.

The error in the simulation is computed as the difference between the simulation results and the exact solution, and plotted in figure 4.4 for $NI = 80$ and $C = 0.4$. All methods show diffusion errors at the shock

position $x = 0.5$, but less so for the MUSCL methods. While the MUSCL methods show very little error in the smoother sections, both first order methods show consistent errors away from the shock. This can be attributed to a dispersion error causing a phase shift.

The Euclidian norm of the error is compared for different grid resolution at constant $2r + C = 1.0$ and is presented in figure 4.5. Both the first order methods show fairly consistent convergence rates at around 1. The last two grid refinements can be said to be within the asymptotic range of convergence for both methods.

The MUSCL methods exhibit better convergence rates and significantly lower total error for the first two grid refinements. For the first two grid refinements both methods appear to asymptotically converge, and have convergence rates around 1.7. For the final grid refinement however, the convergence rate is around 1 for both methods.

Due to the second order central method used for the diffusive flux, the error caused by the diffusive term is going to be second order accurate. The error in the solution is therefore not going to exceed second order accuracy for anything but negligible diffusion, even though the flux functions are third order accurate.

4.7.3   Temporal discretisation accuracy

The numerical temporal integration method also introduces error. However, this error will often be smaller than the error introduced by spatial discretisation. For explicit methods with restrictive stability requirements, this is especially true.

There are various concerns to consider when choosing the time step for a numerical simulation. Most obvious is the requirement for sufficient accuracy. The time step must be small enough for temporal changes to be sufficiently finely resolved. The requirement for sufficient resolution can be expressed as a requirement that the time step Δt is smaller or equal to an accuracy time step Δt_{acc}.

Also the stability of the numerical integration method must be taken into account. The numerical integration method might have stability restrictions that require the time step Δt to be smaller than the stability time step Δt_{stab}.

Numerical integration methods can either be implicit or explicit. The numerical integration methods presented and discussed here are explicit methods. A disadvantage with explicit methods is a sometimes very
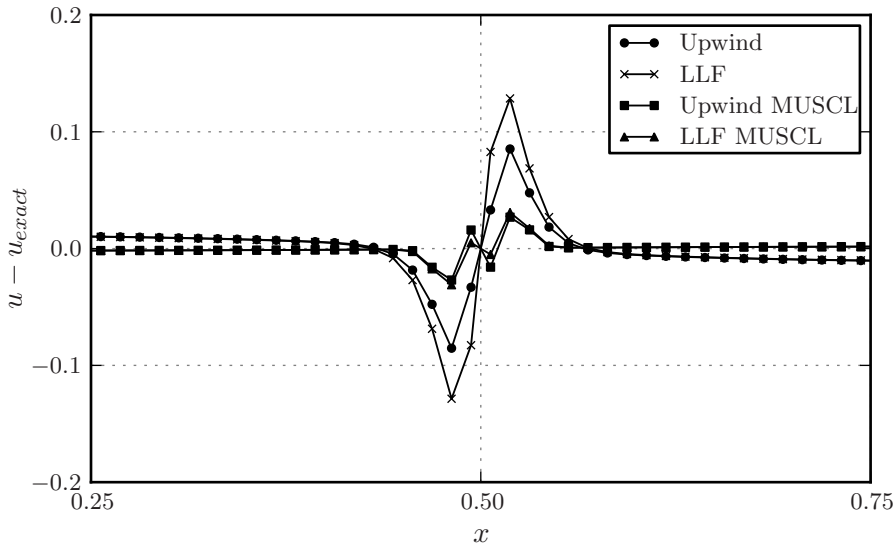
Figure 4.4: Difference between numerical solution and Hopf-Cole solution clearly shows difference in accuracy.
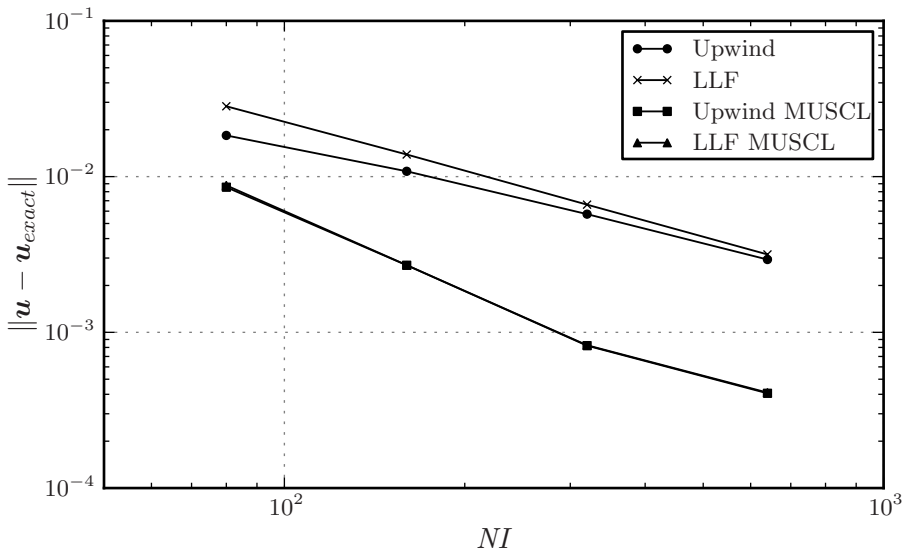

Figure 4.5: The Euclidian norm of the error for the Hopf-Cole problem shows difference in convergence rates for the different flux functions.

restrictive stability requirement. Often the stability time step will be smaller than the accuracy time step, leading to increased computational effort. Explicit methods are chosen here because they are simple to implement and because the required accuracy time steps of the simulations presented later in the report are very small.

Figure 4.6 shows the Euclidian norm of the error for a simulation of the viscous Burgers equation with $u_0 = \sin(2\pi x)$ and viscosity $\nu = 0.005$. The solution is compared with the exact Hopf-Cole solution at time $t = 0.5$, for different time steps Δt and the two different numerical integration methods. Both methods are tested with both the upwind method and the upwind method with MUSCL.

There is a general decrease in error for finer temporal resolution, but only corresponding to a convergence rate around 0.5. The difference between the explicit Euler method and the TVD Runge Kutta method is negligible for the first order upwind method, but more significant for the higher order MUSCL method for the lowest temporal resolution.

The difference in error, both with regards to temporal resolution and integration method appears to be small. This could be because the stability requirement enforces a time step that is so small that the error caused by the temporal discretisation is small in comparison with the spatial error.

4.8 Other convective flux discretisation methods

As will be explained later in the report, the methods for discretising the convective flux discussed thus far did not give satisfying results for the particular type of simulation required. Because of this some alternative discretisation methods were used; these will be presented in this section. The necessity of replacing the previously explained discretisation methods was discovered in the later stages of the project. Therefore, it has not been possible to subject these methods to the same numerical analysis as the former described methods. All methods presented are however well known and documented in the cited literature.

4.8.1 Higher order fixed stencil interpolation

As shown the MUSCL interpolation is used to increase the order of accuracy by computing left and right reconstructions of the velocity at the cell faces. Also other interpolation methods can be used to achieve higher order
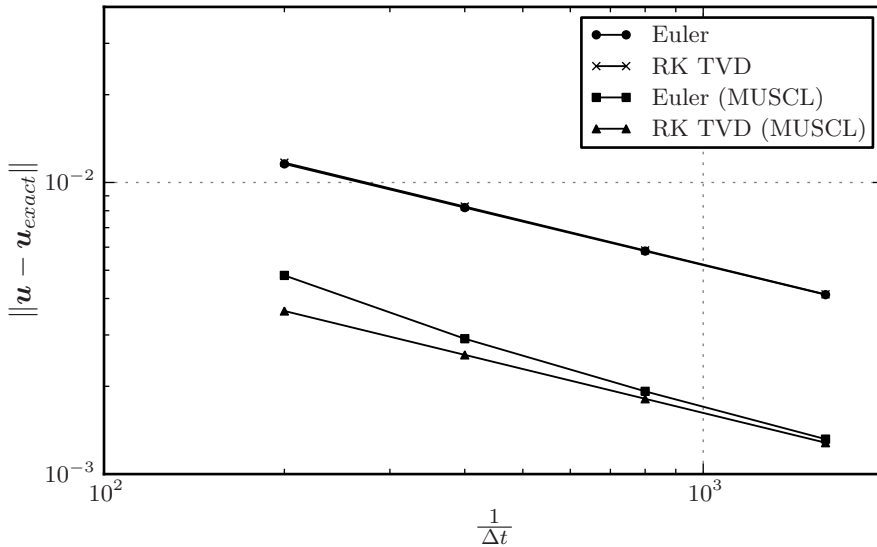
Figure 4.6: The Euclidian norm of the error for the Hopf-Cole problem for different time steps and integration schemes.

accuracy. The order of accuracy of the interpolation is determined by the number of cell values used to reconstruct the velocity. Here a third order reconstruction using three cell values is presented.

When using interpolation to estimate the value at $x_{j+\frac{1}{2}}$ a weighted sum of the neighbouring points is derived and known as a stencil. The stencil weights used by Cockburn *et al.* (1998) for third order approximation at point $x_{j+\frac{1}{2}}$ are the following for different degrees of upwind bias:

$$u_L^a = \frac{11}{6}u_{j+1} - \frac{7}{6}u_{j+2} + \frac{1}{3}u_{j+3} \tag{4.39}$$

$$u_L^b = \frac{1}{3}u_j + \frac{5}{6}u_{j+1} - \frac{1}{6}u_{j+2} \tag{4.40}$$

$$u_L^c = -\frac{1}{6}u_{j-1} + \frac{5}{6}u_j + \frac{1}{3}u_{j+1} \tag{4.41}$$

$$u_L^d = \frac{1}{3}u_{j-2} - \frac{7}{6}u_{j-1} + \frac{11}{6}u_j \tag{4.42}$$

The stencils range from the completely downwind-weighted u_L^a to the completely upwind-weighted u_L^b. Stencil weights for the right side

reconstruction u_R are found by mirroring the stencil weights for the left side reconstruction.

These stencil weights were used by Cockburn *et al.* (1998) in ENO (Essentially Non-Oscillatory Harten *et al.*, 1987) and WENO (Weighted Essentially Non-Oscillatory Liu *et al.*, 1994*b*) schemes to avoid oscillations. This is a different approach to limiting oscillations than the limiting used for the MUSCL interpolation, and involves choosing (ENO) or weighting (WENO) the stencils based on their smoothness. The stencils can also be used for fixed stencil interpolation without limiting or ENO/WENO.

4.8.2   Energy-conserving scheme

Another approach for discretising the convective term is skew-symmetric splitting. This method consists of splitting the convective term in a conservative and a non-conservative part. One of the earliest treatments of skew-symmetric splitting was written by Arakawa (1966). Using the skew-symmetric treatment in the finite difference method the convective term in the Burgers equation is approximated by

$$\frac{\partial \frac{1}{2} u^2}{\partial x} \approx \frac{\theta}{4 \, \Delta x} \left(u_{j+1}^2 - u_{j-1}^2 \right) + \frac{1 - \theta}{2 \, \Delta x} u_j \left(u_{j+1} - u_{j-1} \right). \tag{4.43}$$

For $\theta = \frac{2}{3}$ the method conserves the total energy. This can be seen by inserting $\theta = \frac{2}{3}$

$$\frac{\partial \frac{1}{2} u^2}{\partial x} \approx \frac{1}{6 \, \Delta x} \left(u_{j+1}^2 - u_{j-1}^2 \right) + \frac{1}{6 \, \Delta x} u_j \left(u_{j+1} - u_{j-1} \right), \tag{4.44}$$

and multiplying with u_j

$$\frac{\partial \frac{1}{2} u^2}{\partial x} \approx \frac{1}{6 \, \Delta x} u_j \left(u_{j+1}^2 - u_{j-1}^2 \right) + \frac{1}{6 \, \Delta x} u_j^2 \left(u_{j+1} - u_{j-1} \right), \tag{4.45}$$

and thus $\sum_j u_j^2$ is conserved. The method was covered in further detail by Arakawa (1966), McLachlan (2003) Turner & Rosales (1997) and Yee & Sjögreen (2004), and mentioned briefly by Durbin & Petterson Reif (2011, page 313).

In a finite volume framework the method can be rewritten to give the following flux functions:

$$f_{j-\frac{1}{2}} = \frac{1}{6} \left(u_{j-1} u_j + u_{j-1}^2 + u_j^2 \right) \tag{4.46}$$

$$f_{j+\frac{1}{2}} = \frac{1}{6} \left(u_j u_{j+1} + u_j^2 + u_{j+1}^2 \right) \tag{4.47}$$

These flux functions are then inserted in equation 4.9.

Chapter 5

The Burgers equation and turbulence

The chapter deals with the study of solutions to the stochastically forced Burgers equation, and how they relate to real three-dimensional turbulence. First an overview of the topic is given, and then later in the chapter results from new simulations are presented.

5.1 Burgers turbulence

When J. M. Burgers introduced the Burgers equation, he intended it to be a model equation for turbulence. The Burgers equation contains the same type of advective non-linearity and diffusion term as the three dimensional Navier-Stokes equations. When it was discovered that an explicit analytical solution to the Burgers equation could be found (Hopf, 1950; Cole, 1951), it seemed unlikely that solutions to the Burgers equation could contribute to the study of turbulence. One of the characteristic features of the Navier-Stokes equations and turbulence, is the sensitivity to changes in initial conditions. In real turbulence apparent randomness spontaneously develops; this does not happen with the Burgers equation.

The use of the Burgers equation to study turbulence has gained renewed popularity in recent years (1980s and onwards), and the study of random solutions to the Burgers equation is sometimes referred to as "burgulence". The randomness can either enter through a random initial condition or a stochastic source term, the latter being the approach studied here.

5.1.1   Relevant literature

There have been many studies on Burgers turbulence in recent years, and on how it relates, or does not relate, to real three-dimensional turbulence. Many of these studies are referenced in Frisch & Bec (2001). Analytical solutions to the Burgers equation are well documented and it is well-known that the dominance of shocks in the solution leads to an energy spectrum proportional to k^{-2} (Burgers, 1974).

One method of studying Burgers turbulence, is to study the Burgers equation with stochastic initial condition. The initial condition is typically of Brownian type, or fractional Brownian, with a power law spectrum. Because Brownian motion is continuous but not differentiable, shocks will form after an arbitrarily short time. She *et al.* (1992) studied solutions to the Burgers equation in the limit of vanishing viscosity with a fractional Brownian initial condition. A companion paper by Sinai (1992) studied the statistics of shocks for the same problem. Both showed an energy spectrum proportional to k^{-2}, characteristic of the shocks in the solution.

A general treatment of an n-dimensional Burgers equation with Brownian initial velocity was written by Vergassola *et al.* (1994). It was shown that there was a Devil's staircase of dimension 1/2 in the Lagrangian map of the solution of the Burgers equation in the limit of vanishing viscosity. Decaying Burgers turbulence was also studied by Gurbatov *et al.* (1997) for a homogeneous Gaussian initial condition with a spectrum proportional to k^n for small wave numbers and quickly falling off at large wave numbers.

The study of the stochastically forced Burgers equation has been the topic for many papers. Notably, simulations published by Chekhlov & Yakhot (1995*a*) provided new insight into the physics of Burgers turbulence. It was shown that the one-dimensional Burgers equation with stochastic forcing exhibited turbulence like properties, provided that the stochastic force is white in time with a κ^{-1} spatial power spectrum. The numerical experiments revealed an energy spectrum proportional to $\kappa^{-5/3}$, and strong intermittency.

Further investigations on scaling and statistical properties were published by Chekhlov & Yakhot (1995*b*), where biscaling behaviour was found. Properties of the tails of probability density functions were presented by Yakhot & Chekhlov (1996). Kolmogorov-like scaling was discovered for low order structure functions where ζ_p almost followed $\frac{p}{3}$ for p between $\frac{1}{3}$ and 2. For $p > 4$ the structure function scaled with almost constant exponent

$\zeta_p \approx 0.91$, characteristic of the shocks in the solution. So while the stochastically forced Burgers equation exhibited Kolmogorov scaling for low order structure functions, the higher order structure functions were completely dominated by shocks.

The results of Chekhlov & Yakhot (1995a), Chekhlov & Yakhot (1995b) and Yakhot & Chekhlov (1996) were further generalised by Hayot & Jayaprakash (1996), Hayot & Jayaprakash (1997b) and Hayot & Jayaprakash (1997a). They studied the general case of the stochastically forced Burgers equation with a source term energy spectrum proportional to $\kappa^{-\alpha}$. Theoretical and numerical investigations revealed that for $-1 < \alpha < 1$ increasingly multifractal structures appear as α approaches 1. Similar results as for Chekhlov & Yakhot (1995a), Chekhlov & Yakhot (1995b) and Yakhot & Chekhlov (1996) were found for $\beta = 1$. It was also shown that for $\frac{2}{3} < \alpha < 1$, the structure function scaling exponents could be analytically derived as

$$\zeta_2 = \frac{2\alpha}{3}, \tag{5.1}$$

$$\zeta_3 = \alpha, \tag{5.2}$$

$$\zeta_4 = \frac{2 + \alpha}{3}, \tag{5.3}$$

$$\zeta_5 = 1 - \frac{1 - \alpha}{12}. \tag{5.4}$$

Forced Burgers turbulence with large scale white-in-time random forcing was studied by Gotoh & Kraichnan (1998). So-called kicked Burgers turbulence combines features of decaying Burgers turbulence and continuously forced Burgers turbulence, and was studied by Bec *et al.* (2000).

5.1.2 The stochastically forced Burgers equation

The stochastically forced Burgers equation is the Burgers equation with the addition of a stochastic source term, i.e.

$$\frac{\partial u}{\partial t} + \frac{\partial}{\partial x}\left(\frac{1}{2}u^2\right) = \nu\frac{\partial^2 u}{\partial x^2} + g(x, t), \tag{5.5}$$

where $g(x, t)$ is the stochastic source. The source used here is white noise in time, but with spatial correlation, as for the simulations of Chekhlov & Yakhot (1995a). The source is described by the energy spectrum

$$|\hat{g}(\kappa)|^2 \propto \kappa^{-\alpha}, \tag{5.6}$$

where $(\hat{\cdot})$ denotes the Fourier transform.

5.2   Numerical solution and validation

The stochastically forced Burgers equation is solved numerically using an FVM code, as described in chapter 4.

5.2.1   Stochastic source

The source term in the equation is a stochastic force represented as the superposition of Fourier modes. The stochastic source is implemented in the FVM code as the inverse discrete Fourier transform

$$g(x_j, t) = \sum_{k=0}^{N-1} A_k \exp\left(2\mathrm{i}\pi \frac{jk}{N}\right), \tag{5.7}$$

where

$$A_k = \begin{cases} \frac{A}{\sqrt{\Delta t}} k^{-\alpha/2} e^{\mathrm{i}\phi_k} & \text{for } k \in \{k_1, k_1 + 1, \ldots, k_n\} \\ A_{N-k}{}^* & \text{for } k \in \{N - k_n, N - k_n + 1, \ldots, N - k_1\} \\ 0 & \text{otherwise} \end{cases}, \tag{5.8}$$

$$k_1, k_n \in \mathbb{N}, \quad k_1 \geq 1, \quad k_n < N/2. \tag{5.9}$$

A is a constant, α specifies the spectrum and ϕ_k is the random phase shift for wave number k chosen uniformly in $[0, 2\pi]$. The parameters k_1 and k_n represent the smallest and largest wave numbers, respectively, i is the imaginary unit $\mathrm{i} = \sqrt{-1}$ and $(\cdot)^*$ denotes the complex conjugate. The limiting wave numbers k_1 and k_n are determined by specifying the largest and smallest length scales, $2l$ and δ_G. The division by $\sqrt{\Delta t}$ is a normalisation required to be able to compare solutions for different sized time steps.

In order to reduce the computational time for performing the inverse Fourier transform, the fast Fourier transform (FFT) (Cooley & Tukey, 1965) algorithm was used, taking advantage of the periodicity of the Fourier modes and reducing the computational effort from N^2 to $N \log_2(N)$. The implementation of the source term and the FFT is discussed in more detail in appendix C.

A new set of ϕ_k values are generated for each time step, giving no temporal correlation, implying a white spectrum in time. Because the ϕ_k

values are chosen using a pseudo-random number generator, the numbers are not really random but follow a very long sequence of numbers. Because of the length of this sequence, the numbers can be perceived as random. This has however some consequences that are important to remember. Because of the nature of the algorithm, the same sequence of numbers will be generated each time, if not the generator is seeded using a different parameter. This means that reliable statistics can only be achieved by averaging over a number of simulations with different seeding or by running very long time series. A convenient consequence is that results obtained using the same seed and time step can be compared directly.

Because of the inherent symmetry in the Fourier transform of real functions it is convenient to use the absolute wave number κ defined as

$$\kappa = |k|. \tag{5.10}$$

Thus all references to the wave number κ actually refer to the absolute value of the wave number, and all functions of κ contain the contribution from both positive and negative wave numbers.

5.2.2 Numerical accuracy

To compare the different flux functions, low resolution simulations of the stochastically forced Burgers equation have been compared with a high resolution reference simulation. Source statistics are described by an amplitude constant $A = 0.05$, spectrum $\alpha = 1$ and an upper cut-off wave number of $\kappa = 100$. The equation was integrated in time using the TVD Runge-Kutta method with $\Delta t = 5 \cdot 10^{-5}$, and statistics are computed from $t = 0$ until $t = 10$, starting from initial condition $u_0 = 0$. The kinematic viscosity was $\nu = 1 \cdot 10^{-5}$, and periodic boundary conditions were used.

Simulations for 2^9 grid cells in $[0, 1]$ were compared with a reference simulation of 2^{13} grid cells. For the low resolution simulations all four flux function combinations, upwind and local Lax-Friedrichs with and without MUSCL, were tested and compared with the reference simulation using local Lax-Friedrichs method with MUSCL.

Averaged amplitude spectra for the results are plotted in figure 5.1 to investigate how well the different methods perform at low and high wave numbers. The spectra at the low resolutions are plotted up until $\kappa = 1/(2\,\Delta x)$, beyond which no spectral information exists.

The first order methods start deviating from the reference simulation already at wave number 20, while the higher order methods follow the
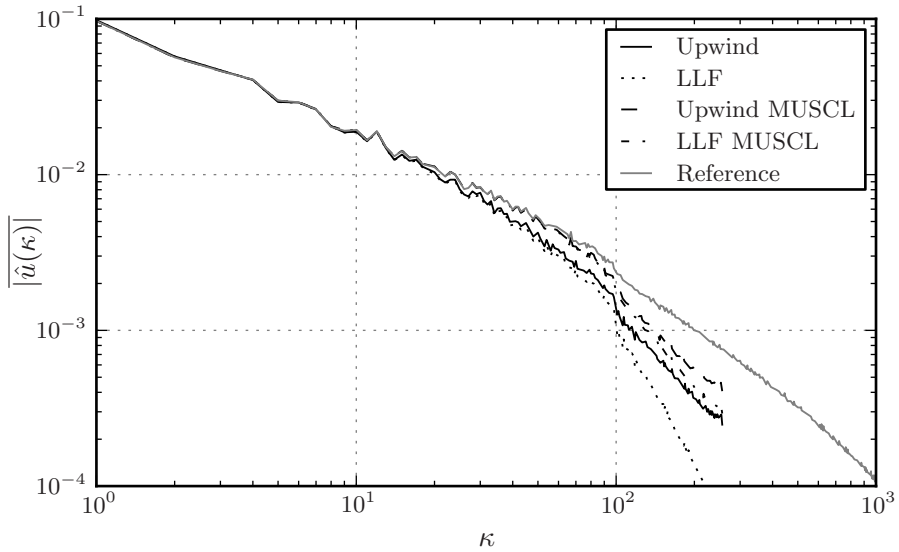
Figure 5.1: The averaged amplitude spectra of the velocity for the four different convective flux functions for 2^9 grid cells are compared with a reference simulation using the local Lax-Friedrichs method with MUSCL for 2^{13} grid cells.

reference spectrum until $\kappa = 70$. All methods end up deviating significantly, proving that the resolution is too low. In addition to exhibiting superior results for the higher order methods, the amplitude spectra also appear to exhibit less high wave number damping for the upwind flux function. This difference is less significant for the MUSCL methods.

To estimate the accuracy of the numerical solution in chapter 4 the exact solution was used as a reference. When no such reference exists, a common approach is to estimate accuracy by grid refinement. The difference in error for two different grids is equal to the difference between the two solutions. To study the accuracy of the different numerical methods and different grid sizes, the four different flux functions were tested for six different grids.

Numerical simulations of the stochastically forced Burgers equation with source described by the parameters $A = 0.035$, $2L = 1$, $\delta_G = 0.01$, $\alpha = 2$, were conducted for the different methods. The solutions were compared after $t = 2$ with a time step equal to $\Delta t = 5 \cdot 10^{-5}$ and for grids with $NI \in \{625, 1250, 2500, 5000, 10000, 20000\}$. The simulation domain
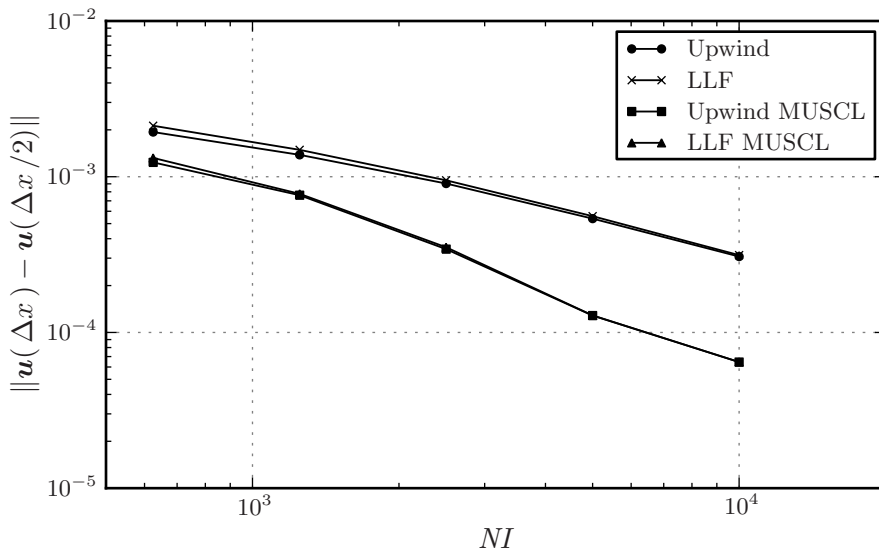
Figure 5.2: The Euclidian norm of the difference in solution for grid refinement, for the different flux functions.
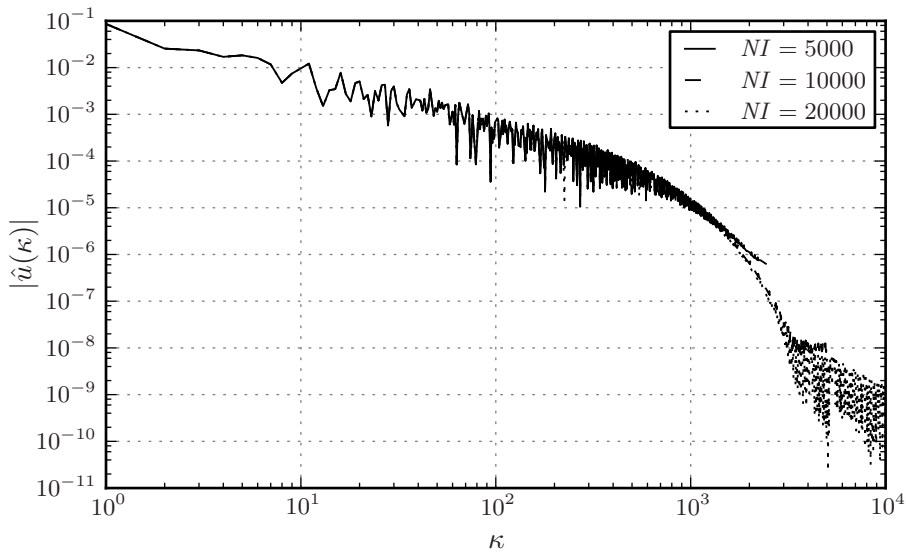

Figure 5.3: The amplitude spectrum of the velocity for three different grids for the local Lax-Friedrichs method with MUSCL.

was $x \in [0, 1]$, the viscosity $\nu = 1 \cdot 10^{-5}$ and initial condition $u_0 = 0$. The maximum velocity for this simulation is around 0.15. The temporal discretisation method used is the TVD Runge-Kutta method.

The solution at grid spacing Δx was compared with the solution at grid spacing $\frac{\Delta x}{2}$ and plotted in figure 5.2 to study the accuracy. As is apparent from the figure, the Euclidian norm of the difference is strictly decreasing, showing that the enhancement in accuracy gets smaller for each grid refinement. As for earlier tests, the difference between the upwind and the local Lax-Friedrichs method is very small, and the MUSCL interpolation increases accuracy.

To better be able to judge the effect of grid refinement, the amplitude spectra of the local Lax-Friedrichs method with MUSCL for three different grids ($NI \in \{5000, 10000, 20000\}$) are plotted in figure 5.3. A too low resolution means that the smaller scales of the problem are not properly resolved. This will show itself in the spectrum by inaccurate representation of high wave number modes. The spectra are plotted up to wave number $\kappa = 1/(2 \, \Delta x)$.

All three spectra follow a seemingly linear curve in most of the wave number range, and transition to a steeper declining range at wave number around 1000. The linear range is equivalent to the inertial range in three dimensional turbulence, and this range then transitions to the dissipation range. The three spectra seem to follow each other for all of the inertial range and the beginning transition to the dissipation range. How well resolved the smallest scales need to be is difficult to determine, but it is believed that most essential scales are resolved for all three simulations. The rapid decline in amplitude beyond wave number 1000 means that the smaller scales have much less energy and are less and less important for the larger scales.

The change in slope for the high resolution spectrum at wave number $\kappa = 3000$ does not appear to be physically sound, and this phenomenon does not occur for the first order methods. It is likely that this is a purely numerical effect.

The consistent reduction in error together with the small difference in amplitude spectrum between $NI = 10000$ and $NI = 20000$, implies that the results can be trusted as good numerical solutions of the problem. Since the convergence rate is different for the different grid refinements, it is difficult to get an accurate estimate of the total error in the solution at a given grid spacing. It is however, reasonable to assume that the error will be
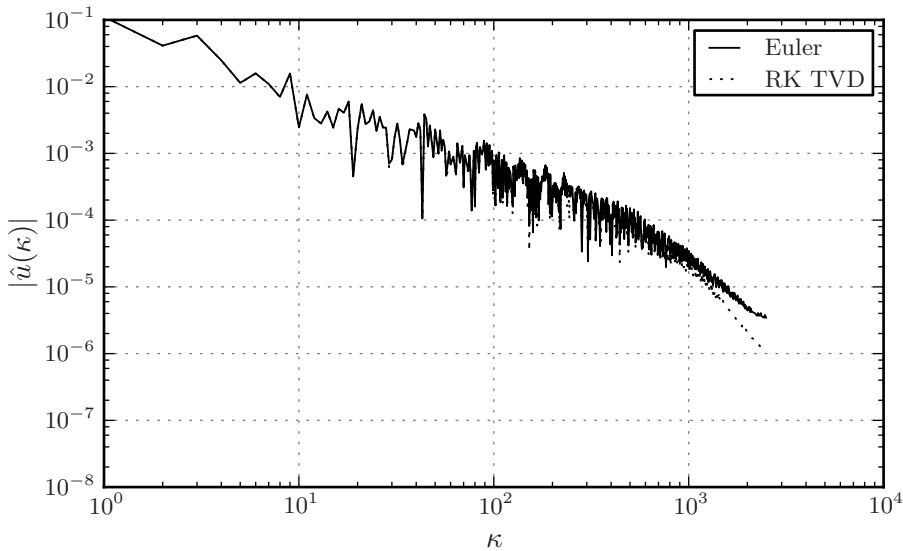
Figure 5.4: The amplitude spectrum of the velocity for the explicit Euler method and the TVD Runge-Kutta method for $\Delta t = 4 \cdot 10^{-4}$, for the local Lax-Friedrichs method with MUSCL.

of the same order of magnitude as the grid refinement differences plotted in figure 5.2. A resolution of 10000 should therefore have an estimated error of $\mathcal{O}(10^{-4})$. The relative size of this error compared with a velocity in the range $(-0.15, 0.15)$ combined with resolving scales well beyond the transition point to the dissipation range, suggests that the resolution is sufficient.

Because a new value of the source term is generated every time step, it is not possible to make direct comparisons between the results at a given time for different time steps. A study of the effect of changing the time step, could therefore be concerned with statistical properties. However, composing good statistics requires large amounts of data, and it will always be difficult to distinguish small differences when the sample is different. To compare the effect of changing the time step, the results from the two different numerical integration methods are compared. If the results from these two methods are not significantly different, it can be assumed that the temporal resolution is sufficient. The logic of this argument, is that when two different integration methods, of different theoretical order of accuracy,
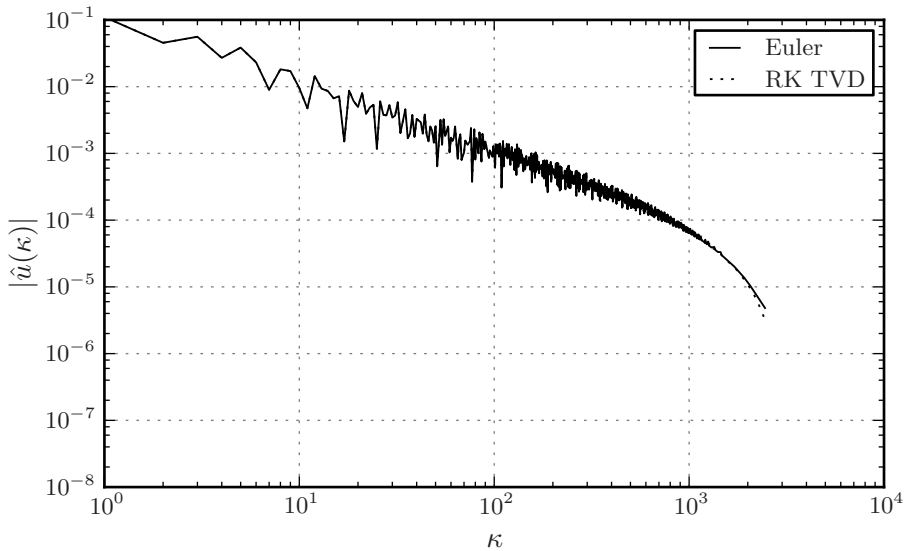
Figure 5.5: The amplitude spectrum of the velocity for the explicit Euler method and the TVD Runge-Kutta method for $\Delta t = 5 \cdot 10^{-5}$, for the local Lax-Friedrichs method with MUSCL.

give the same results, then the velocity is so smooth in time that the result is not dependent on the numerical integration method.

For the three different time step sizes $\Delta t \in \{5 \cdot 10^{-5}, 1 \cdot 10^{-4}, 4 \cdot 10^{-4}\}$, the stochastically forced Burgers equation has been solved numerically using both the explicit Euler method and the TVD Runge-Kutta method. The spatial resolution is $NI = 10000$ and the flux function used is the local Lax-Friedrichs method with MUSCL. The solutions are compared after $t = 1$. Other parameters are as before, but with a velocity field from after a statistically steady state is reached as initial condition.

The amplitude spectra for $\Delta t = 4 \cdot 10^{-4}$ for both the explicit Euler method and the TVD Runge-Kutta method are plotted in figure 5.4. There is a difference at high wave numbers, showing that the high wave number content of the solution is computed differently for the two integration methods. When the time step is reduced to $\Delta t = 5 \cdot 10^{-5}$, this difference is almost removed entirely (see figure 5.5). An independence of the temporal discretisation method is a good indication of the temporal resolution being sufficiently high. The difference present at the higher value of Δt does

not appear to be of crucial importance, and that time step is about the highest possible time step for which the solution is stable for both temporal integration methods.

The most fundamental criterion of sufficient temporal resolution is smoothness in time, as this is the very assumption employed when developing the methods used. Smoothness requires that the change in velocity is small in one time step. For $\Delta t = 4e - 4$ the maximum absolute change in u for the final time step is 0.014, and the average absolute change for the final time step is $1 \cdot 10^{-3}$. For 0.001 the numbers are 0.0027 and $1.7 \cdot 10^{-4}$ respectively. For velocity values in the range $(-0.15, 0.15)$, at least the smallest Δt can be said to be sufficiently smooth.

The results presented here are used to determine the numerical methods utilised for further simulations. Due to the reduction in error high order flux functions using MUSCL are chosen. There does not seem to be significant difference between the upwind method and the local Lax-Friedrichs method, and both appear to produce good results. When choosing the resolution, the primary concern is to resolve all scales in the inertial range. Simulations where the transition to the dissipation range is well within the resolved range are considered to have a sufficiently low Δx. The numerical methods used here have predictable behaviour also for low resolutions and the only appreciable differences are deviations at the largest applicable scales.

For numerical integration in time the TVD Runge-Kutta method is chosen for its larger stability domain and the higher theoretical order of accuracy. Due to the added steps of computing the TVD Runge-Kutta method will increase computation time compared with the explicit Euler method. The time step is then chosen so that there is no discernible difference between the results from the explicit Euler and the TVD Runge-Kutta method.

5.2.3 Initial condition and stationary solution

In order to compose good statistics from a solution, the sampling must start after a statistically steady state is reached, assuming that such a state exists. The statistical properties of the steady state condition should be independent of initial condition and statistically steady. In order to test different types of initial conditions and determine the time until the steady state was reached, simulations of the stochastically forced Burgers equation were conducted from $t = 0$ to $t = 20$.

All simulations had $NI = 4096$ grid cells and time step $\Delta t = 5 \cdot 10^{-5}$.
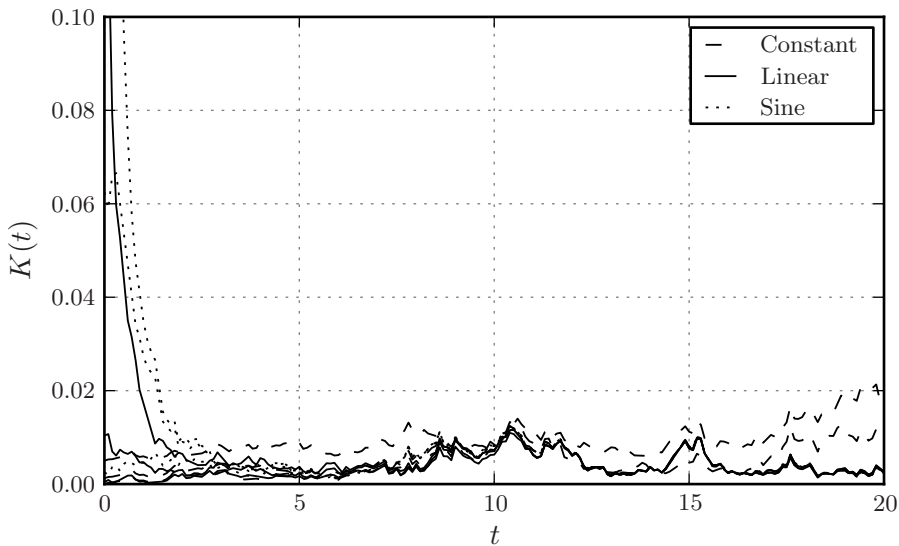
Figure 5.6: The total kinetic energy is plotted against time for constant, linear and trigonometric initial conditions, each with three different initial energy levels. The initial conditions are listed in equation 5.13.

The kinematic viscosity was $\nu = 1 \cdot 10^{-5}$ and the stochastic source was specified by the parameters $A = 0.035$, $2L = 1$, $\alpha = 2$ and $\delta_G = 0.01$.

The property used to study the dynamical behaviour of the system is the total specific kinetic energy $\frac{1}{2}u^2$, determined by integrating the power spectrum over all wave numbers. In order to study the dynamical development of the energy at particular scales the energy spectrum can be integrated over a certain range of wave numbers. So, the total kinetic energy in the velocity field is calculated as

$$K(t) = \int_0^\infty \frac{1}{2}(\hat{u}(\kappa))^2 \, d\kappa \,, \tag{5.11}$$

and the kinetic energy at wave numbers higher than $\kappa = 500$ is calculated as

$$K_{\kappa>500}(t) = \int_{500}^\infty \frac{1}{2}(\hat{u}(\kappa))^2 \, d\kappa \,. \tag{5.12}$$

As the stochastic source only contains energy at wave numbers up to $\kappa = N = \frac{1}{0.01} = 100$, the high wave number energy is produced by the dynamics of the equation.
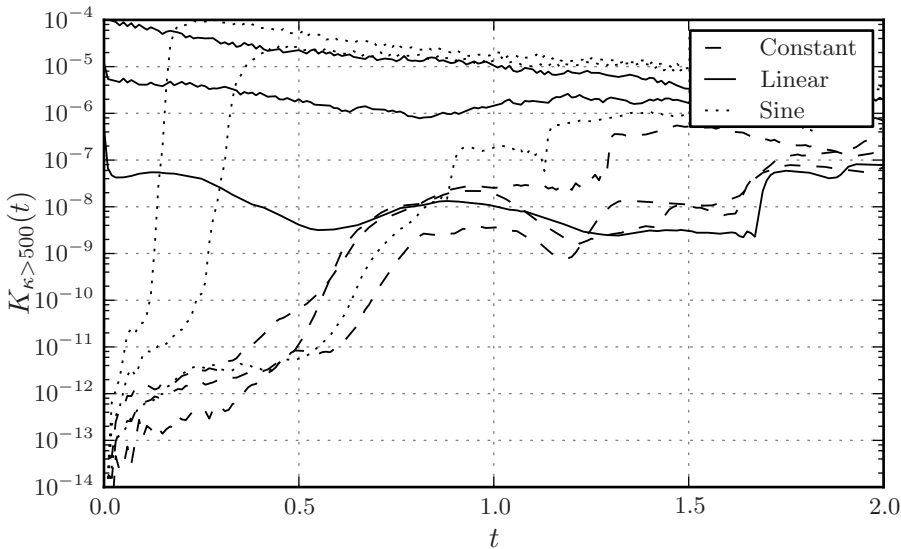
Figure 5.7: The total kinetic energy for wave numbers $\kappa > 500$ is plotted against time for constant, linear and trigonometric initial conditions, each with three different initial energy levels. The initial conditions are listed in equation 5.13.

Nine different initial conditions were tested, representing a range of different characteristics in initial energy content and spectrum. The initial conditions were the following:

$$
\begin{array}{lll}
u_0 = 0.0 & u_0 = 0.05 & u_0 = 0.1 \\
u_0 = 0.1x - 0.05 & u_0 = 0.5x - 0.25 & u_0 = 2.0x - 1.0 \\
u_0 = 0.1\sin(2\pi x) & u_0 = 0.5\sin(2\pi x) & u_0 = 1.0\sin(2\pi x)
\end{array}
\tag{5.13}
$$

These initial conditions exhibit, through the change of exponents, difference in initial kinetic energy. There is also a difference in spectral content. While the constant initial conditions and the sine initial conditions only contain energy at wave numbers zero and one respectively, the linear initial condition contains energy over a wide range of scales. Together these nine different initial conditions cover a large range of energy and spectral properties.

The total kinetic energy is plotted in figure 5.6 from $t = 0$ to $t = 2$. The different initial conditions all seem to converge towards a steady condition

quite rapidly, and already at $t = 5$ most of the curves seem to have flattened out. All but two initial conditions collapse at approximately $t = 13$, marking the point at which all memory of the initial condition seems to be lost. The two curves that deviate after $t = 13$ are the two non-zero constant initial conditions. The constant velocity in the initial data is not smoothed out considerably over time because of the lack of gradients. The spectral content of the initial condition does not seem to affect the convergence much, and the total energy in the high energy initial conditions is quite rapidly dissipated. All simulations reach a steady state condition rapidly, but the fluctuations in energy are large in the steady region.

To better understand the physics of the dynamical process towards steady state, the high wave number energy is plotted in figure 5.7. The comments above are also valid for the high wave number energy, and the energy at high wave numbers is also equal for all but two initial conditions for $t > 13$ (not shown here). Some other observations, are however also pertinent.   The linear initial conditions already contain energy at high wave numbers, and the process towards steady state is a smooth process of redistribution among the scales.

For two of the sine initial conditions (the two with highest initial energy) the solution exhibits a jump in high wave number energy and then a smooth decay. What happens is that the energy in the initial sine function is rapidly transported towards smaller scales, as seen in figure 2.5. For the rest of the energy curves, the increase in high wave number energy is later and smaller, and is caused by the energy in the stochastic source being transported to smaller scales.

Both the plot of total energy and high wave number energy show a process in which the energy in the initial condition is transported to higher wave numbers and eventually dissipated. As long as the initial conditions contain sufficient gradients, the energy of the initial condition is lost after $t = 13$, and a steady state can be said to be reached much sooner than this.

The rapid reduction of energy from the initial condition seems to imply that all memory of the initial condition is lost after a short amount of time. A velocity plot at $t = 10$ and $t = 20$ for initial condition $u_0 = 0.5x - 0.25$ in figure 5.8 does, however, seem to imply otherwise. At the time $t = 10$ the energy in the solution is almost identical to the other simulations, as seen in figure 5.6, but the velocity shows a quite distinctive sawtooth like profile reminiscent of the initial condition. Although it is very subtle, the velocity at time $t = 20$ also has one distinctive large shock that remains
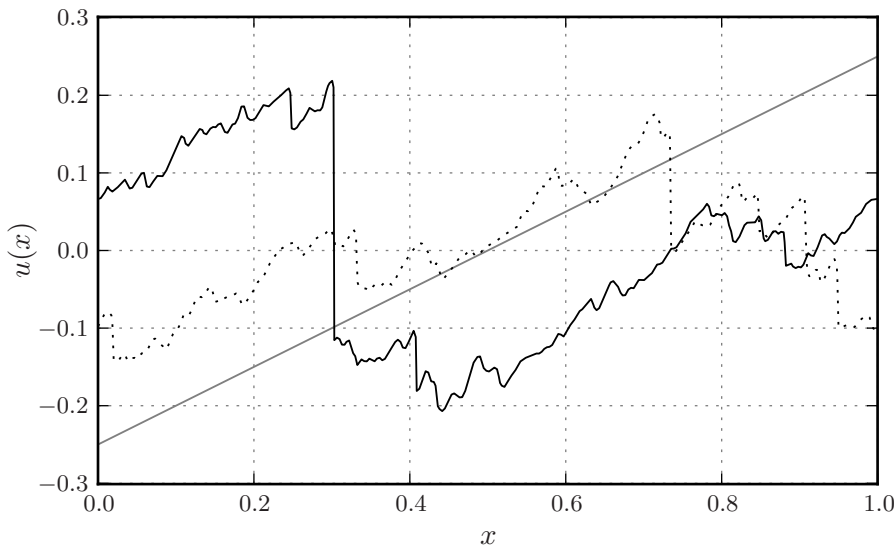
Figure 5.8: Velocity plotted at time $t = 10$ (solid black line) and $t = 20$ (dotted line) for initial condition $u_0 = 0.5x - 0.25$ exhibits a similar sawtooth pattern.

from the initial condition. This shows that even though the energy in the initial condition is dissipated, memory of shock patterns remains for much longer.

5.2.4 Comparison with published results

Simulations using the local Lax-Friedrichs method with MUSCL for 2^{15} and 2^{14} grid cells for $x \in [0, 2\pi]$ were conducted to be compared with previously published results by Scotti & Meneveau (1999). The TVD Runge-Kutta method was used for integration in time, and the time step was $\Delta t = 5 \cdot 10^{-5}$. Kinematic viscosity was $\nu = 1 \cdot 10^{-5}$, and the source parameters were $A = \sqrt{2} \cdot 10^{-3}$, $\alpha = 1$, with forcing at all scales. Initial conditions were $u_0 = 0.1 \sin(2\pi x)$ for the simulation with 2^{15} grid cells and $u_0 = 0.02(x - \pi)$ for the simulation with 2^{14} grid cells.

Energy spectra averaged between $t = 60$ and $t = 200$ are shown in figure 5.9, compared with results from a pseudo-spectral code by Scotti & Meneveau using 2^{13} modes. All three simulation results exhibit
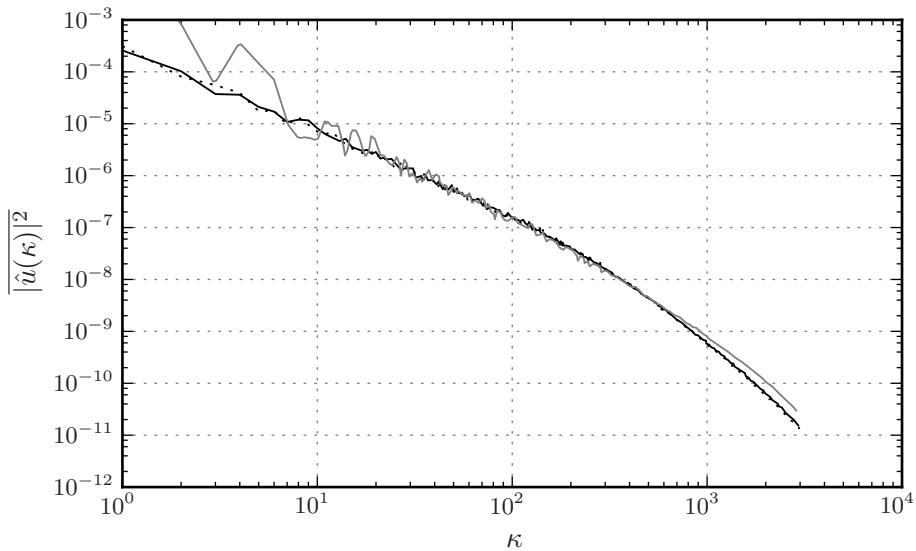
Figure 5.9: Averaged energy spectra for simulation using 2^{15} grid cells (solid black line) and simulation using 2^{14} grid cells (dotted line), compared with previously published amplitude spectrum of Scotti & Meneveau (1999) (grey line).

the $-5/3$ energy spectrum slope, characteristic of this type of Burgers turbulence. Spectrum results correspond well for most wave numbers, but deviate at the lowest wave numbers and for wave numbers larger than 10^3. The significance of this deviation is uncertain, but the high wave number difference could be attributed to excessive damping for the simulations presented here. There is however very little difference between the simulation with 2^{15} grid cells and the simulation with 2^{14} grid cells, and if the high wave number discrepancy was caused by numerical diffusion, one would expect the simulation with the highest resolution to yield better results.

It is perhaps more likely that the difference at high wave numbers is related to the difference at the lowest wave numbers. The simulation results from Scotti & Meneveau have large scales with significantly more energy, and thus more energy is transported to the smallest scales. The lack of smoothness at the smallest wave numbers indicates persistent large scale structures. This difference could perhaps be caused by the implementation
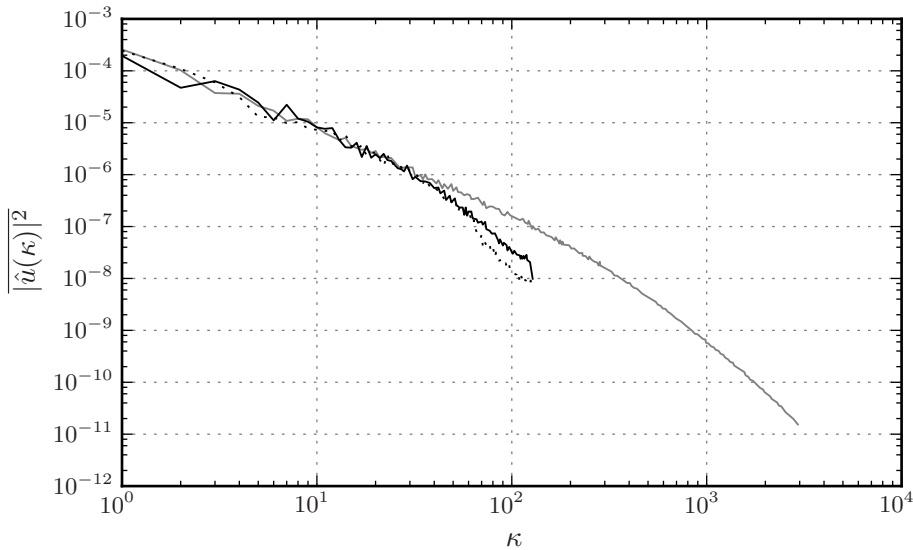
Figure 5.10: Averaged energy spectra for low resolution simulations using 2^8 grid cells and filter width $\Delta = 2\pi/128$ (solid black line) and filter width $\Delta = 2\pi/64$ (dotted line), compared with simulation using 2^{14} grid cells (grey line).

of the source term or the initial condition, the details of which are not entirely clear. Tests with different types of initial conditions have shown that even though the energy of the initial condition quite quickly dies out, traits of the initial condition, in particular shock patterns, survive for a long time.

Additional simulations at a very low resolution of 2^8 grid cells are compared with the high resolution simulation in figure 5.10, for similar initial conditions. These simulations represent one-dimensional large eddy simulations without subgrid modelling, and are filtered using a spectral cut-off filter (implemented by only prescribing the lowest wave numbers of the stochastic source). Filtering widths of both $\Delta = 2\pi/128$ and $\Delta = 2\pi/64$ were tested.

Energy spectra for both low resolution simulations follow the high resolution energy spectrum for wave numbers smaller than 40, but deviate for larger wave numbers. There is no build-up at the highest wave numbers, as one might expect, but instead excessive damping. Increasing

the filtering width to $2\pi/64$ increases the difference at the highest wave numbers. The results show that at this resolution and stochastic forcing, the numerical diffusion is sufficiently large to function as an eddy viscosity, thus dissipating the energy. Sufficient dissipation does not, however, by itself constitute a good subgrid model, and a dedicated subgrid model should be able to produce better results.

The evolution of large scale kinetic energy per length scale, defined

$$K(t) = \frac{1}{2 \cdot 2\pi} \int_0^{2\pi} \tilde{u}^2 \, dx \,, \tag{5.14}$$

is plotted in figure 5.11 for the highest resolution simulation, the low resolution simulation filtered at $\Delta = 2\pi/128$ and the simulation by Scotti & Meneveau. $\tilde{u}$ is the velocity u filtered at scale $\Delta = 2\pi/128$. All three spectral curves decay from an initial condition with high kinetic energy and then reach a statistically steady state where forcing and dissipation are in approximate equilibrium. Again it is apparent that the low resolution simulation dissipates a significant amount of energy, as the energy levels out instead of strictly increasing.

Within the statistically steady region, the kinetic energy fluctuations are large. This is because of the instability of the largest scales containing most of the energy, and could also be part of the explanation for the discrepancy seen in figure 5.9. Truly reliable statistics would require much longer time series than the ones used here. Another noteworthy observation is that the energy decreases far more rapidly from the initial condition for the simulations presented here, than for the results from Scotti & Meneveau. This is indicative of different initial conditions and lends credibility to the notion that the initial conditions could cause some of the difference observed in figure 5.9.

The effect of time step size was tested by comparing two simulations with 2^{14} grid cells, one with $\Delta t = 5 \cdot 10^{-5}$ and one with $\Delta t = 1 \cdot 10^{-5}$. Energy spectra for these two simulations almost completely overlapped, proving that the time step is low enough for the statistical features of the solution to be independent of time step size. This result is contingent on the normalisation by $1/\sqrt{\Delta t}$ in the amplitude of the source.

5.2.5   Effect of source parameters

The statistical properties of the stochastic force are to a large degree described by the Fourier spectrum. Three of the most well known types of
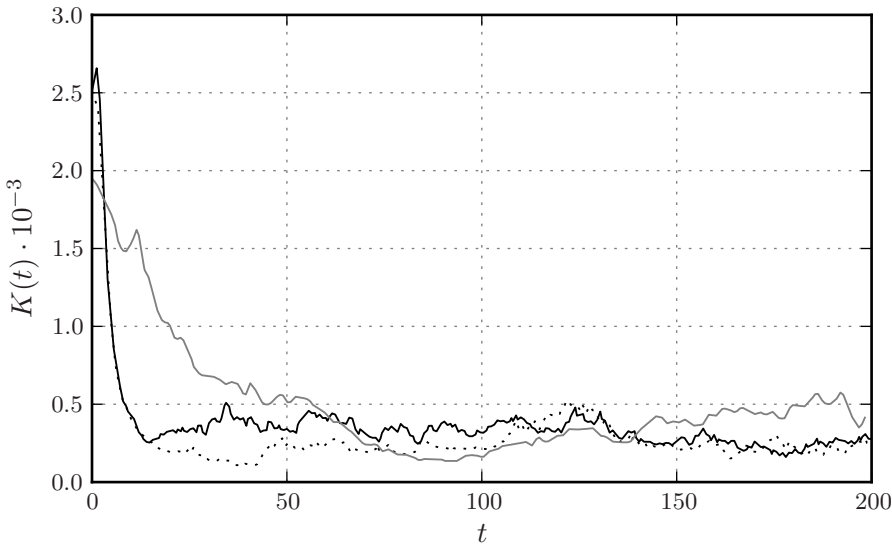
Figure 5.11: Evolution of large scale kinetic energy simulation using 2^{15} grid cells (solid black line) compared with previously published results from Scotti & Meneveau (1999) (grey line) and low resolution simulation with 2^8 grid cells filtered at $\Delta = 2\pi/128$ (dotted line).

noise functions are white noise with an energy spectrum $\propto \kappa^0$, pink noise with energy spectrum $\propto \kappa^{-1}$ and brown noise with an energy spectrum $\propto \kappa^{-2}$. These three energy spectra have been tested as sources in the stochastically forced Burgers equation in order to determine how the spectral properties of the source affects the spectral properties of the results.

Simulations have been conducted using the local Lax-Friedrichs method with MUSCL interpolation for the convective fluxes, and the TVD Runge-Kutta method in time with $\Delta t = 5 \cdot 10^{-5}$. The viscosity is $\nu = 1 \cdot 10^{-5}$, there are 2^{13} grid cells, and the source has an amplitude coefficient $A = 0.05$ and forcing at all admissible scales. All amplitude spectra are averaged over $t \in [10, 20]$, after a statistically steady state is reached, and all simulations are started from initial condition $u_0 = 0$.

Figure 5.12 shows the resulting velocity and time-averaged energy spectra $|\hat{u}(\kappa)|^2$ of the solution for the three different source types, white, pink and brown. Also plotted in the figure are the energy spectra of the source functions and proposed regression lines. A first observation is that
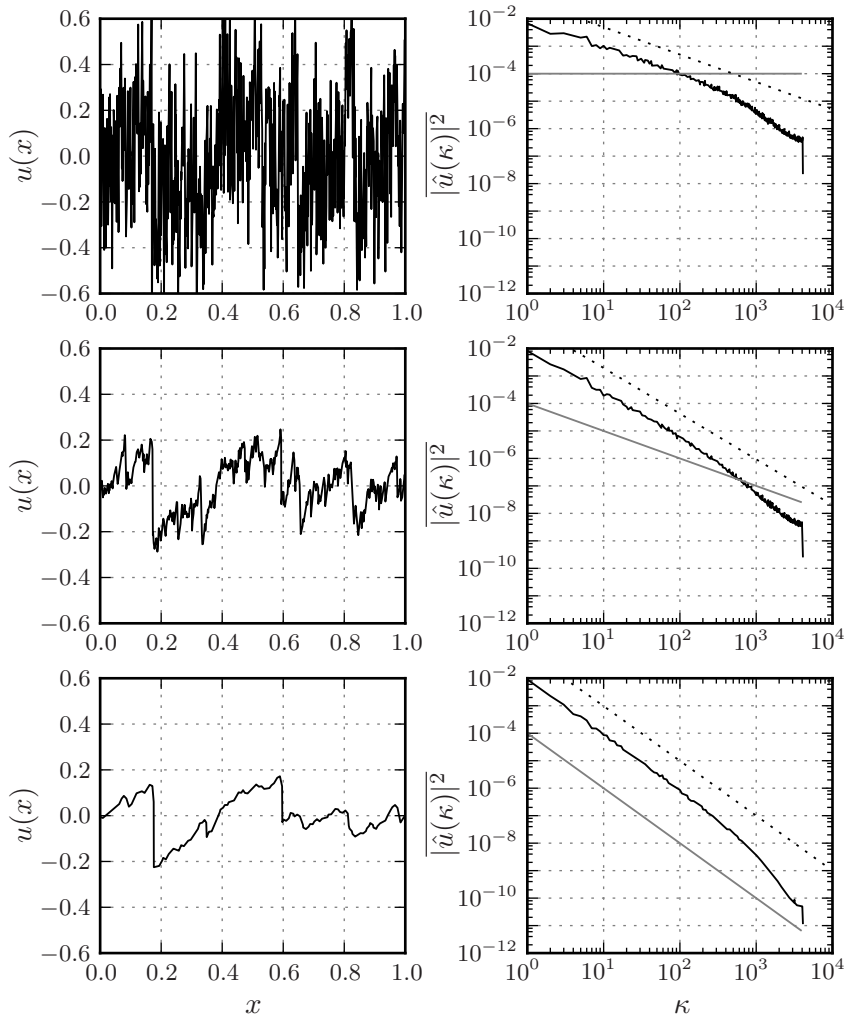
Figure 5.12: The velocity (left) and energy spectrum (right) for the three different source energy spectrum slopes κ^0 (top), κ^{-1} (centre) and κ^{-2} (bottom), corresponding to white, pink and brown noise, respectively. The grey lines are the energy spectra of the sources (multiplied by a factor 10^{-6}), and the dotted lines represent, from top to bottom, power laws κ^{-1}, $\kappa^{-5/3}$ and κ^{-2}.

the presence of a source term, with energy spectrum decreasing less rapidly than the κ^{-2} Burgers shocks, reduces the negative slopes of the spectra.

The velocity plots reveal obvious differences between the three different source types. The velocity plotted for the white source shows little coherent large-scale structures, but high-amplitude noise over a wide range of wave numbers. This is caused by the white source having equal amplitudes for all wave numbers. The energy spectrum follows the regression line κ^{-1} quite well, serving as a combination between the stochastic noise and the physics of the shocks in the Burgers equation.

The velocity plot for the source with a pink spectrum shows existence of large-scale structures as well as smaller structures over a range of wave numbers. This is explained by the energy spectrum falling more steeply than for the white source, and following the $\kappa^{-5/3}$ regression line reasonably well. Much less small scale structures are present in the last velocity plot, with the brown source. The solution is very much dominated by the large scale shocks, also apparent in the energy spectrum that follows the expected k^{-2}.

Out of the three velocity plots, the pink noise solution, is the one that resembles real turbulence the most. This is backed up by an energy spectrum following $\kappa^{-5/3}$, Kolmogorov's energy spectrum for homogeneous turbulence, as previously reported by Checklov & Yakhot Chekhlov & Yakhot (1995a).

The spectral slope of a graph also provides information about other features of the graph. For example a power law energy spectrum proves the existence of scaling laws, and it is expected that the graphs with energy spectral slopes -1, $-5/3$ and -2 have fractal dimensions (see e.g. Mandelbrot (1982)) 2, 5/3 and 3/2, respectively. A high fractal dimension is consistent with a high degree of roughness, evident from the velocity plots. The indicated spectral slopes also lead to second order structure functions scaling as $S_2(r) \propto r^0$, $S_2(r) \propto r^{2/3}$ and $S_2(r) \propto r^1$ for the white, pink and brown source, respectively.

Two other source parameters that are also expected to change the results are the source amplitude constant A and the lower cut-off scale δ_G. The effect of changing these parameters is presented in figures 5.13 and 5.14, respectively.

Figure 5.13 shows how the stochastic source reduces the negative slope of the energy spectrum in the region where it contributes energy. In the transition between forced and non-forced scales there is a sharp transition

Figure 5.13: The velocity (left) and energy spectrum (right) for the three different source lower cut-off scales $\delta_G = 0.1$ (top), $\delta_G = 0.01$ (centre) and $\delta_G = 0.001$ (bottom).
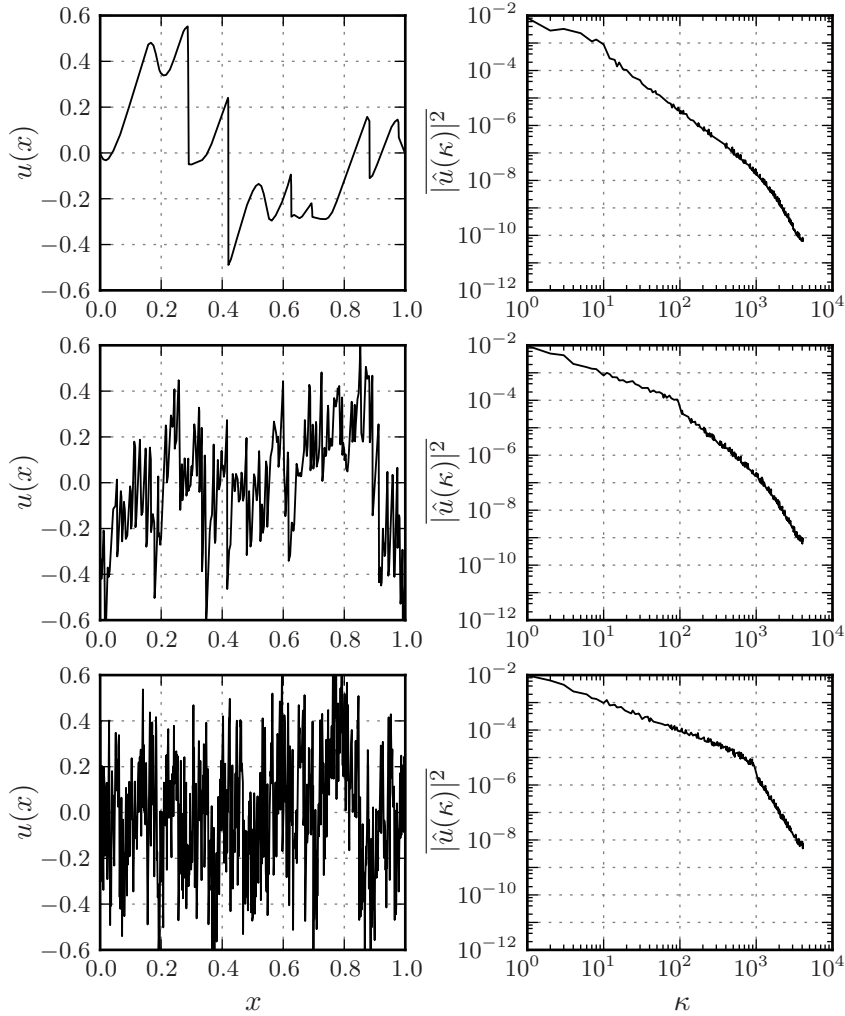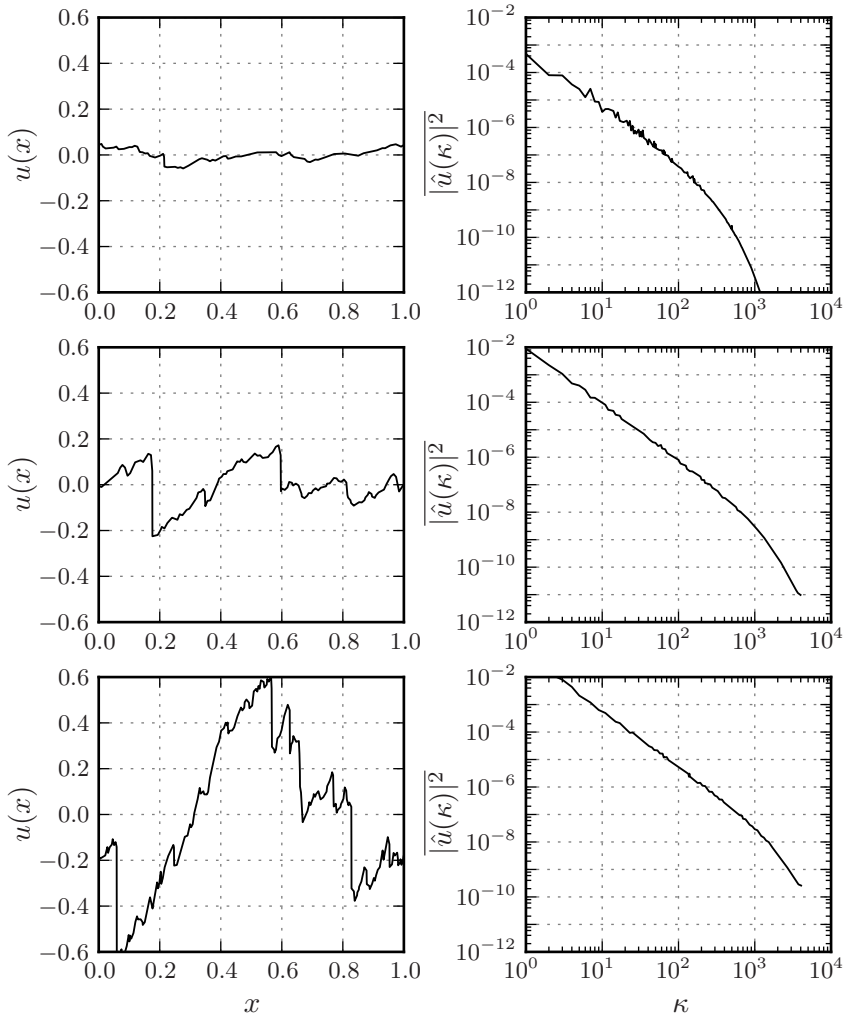
Figure 5.14: The velocity (left) and energy spectrum (right) for the three different source constants $A = 0.01$ (top), $A = 0.05$ (centre) and $A = 0.2$ (bottom).

to a steeper negative slope. This is also clearly shown on the velocity plots where the energy at higher wave numbers clearly increases as the range of the source is increased.

Increasing the source constant has the effect of increasing the amplitude of the velocity. This lifts the whole energy spectrum, but more interestingly extends the linear inertial range towards larger wave numbers. More energy in the larger scales causes more energy to be transferred to the smaller scales. This is similar to the process in three-dimensional turbulence where energy in large scale eddies are transferred to the smaller scales.

5.3   DNS of Burgers turbulence

Based on the numerical analysis presented thus far, numerical methods were chosen for fully resolved simulations of the stochastically forced Burgers equation. The simulation results presented in this chapter are the reference results later used when comparing subgrid models, and are referred to as DNS.

The TVD Runge-Kutta method was chosen for temporal integration with a time step of $\Delta t = 1 \cdot 10^{-5}$, and the upwind MUSCL method was used for convective flux discretisation. A total of 20000 grid cells were used for the domain $x \in (0, 1)$ and the simulation was run from $t = 0$ until $t = 1000$. The kinematic viscosity was $\nu = 5 \cdot 10^{-6}$. The simulation was initialised with a $\kappa^{-5/3}$ stochastic initial condition, and, as before, periodic boundary conditions were used. The parameters describing the source were $A = 0.25$ and $\alpha = 1$ (pink), with forcing at all scales.

The velocity plotted at $t = 2$ is shown in figures 5.15 5.16, showing existence of a large number of smaller shocks as well as some large shocks. The evolution of total kinetic energy $K(t)$ is plotted in figure 5.17 for the first two time units, and it can be seen that the energy decreases from the initial value and stabilises around a stationary condition after $t = 0.5$. A suitable characteristic time scale for the problem is 1, and so the simulation spans 1000 time scales, which should be sufficient for good statistics.

When plotting the total kinetic energy over a longer period of time, a slightly different image emerges. Figure 5.18 shows the kinetic energy for the first 50 time units, and it becomes clear how highly fluctuating the steady state energy is. The instability of the larger shocks in the solution causes large variations in the total kinetic energy. There are, however, no consistent trends and the solution can be considered to be
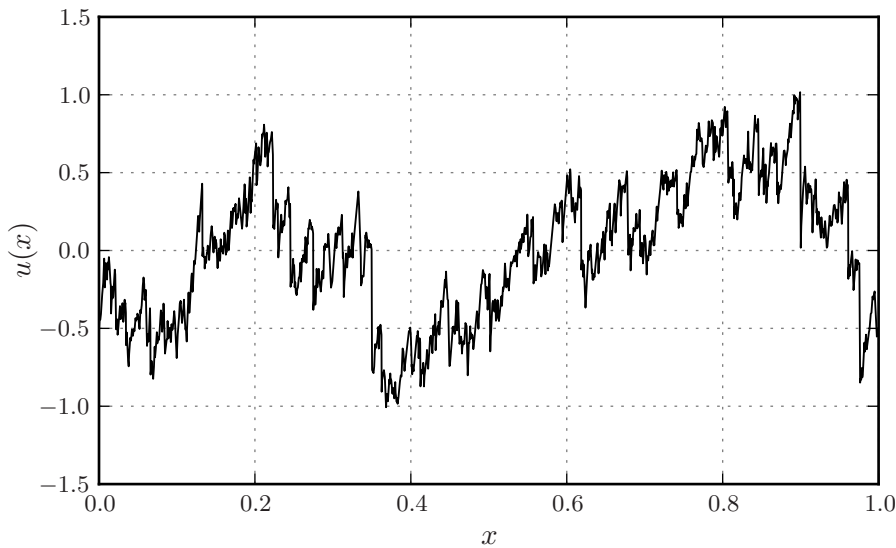
Figure 5.15: Velocity at time $t = 2$ for DNS with pink noise source shows presence of many small shocks and some large shocks

statistically steady. Due to the large variation in energy, long time-series will be important when computing averaged statistics. All time-averaged quantities are averaged from $t = 50$, at which point a stationary condition is surely reached, until $t = 1000$ unless otherwise noted. 100 time samples are used for each time unit, for a total of 950000 time samples for the whole simulation.

5.3.1 Energy spectrum

As noted before the $-\frac{5}{3}$ slope of the energy spectrum is one of the characteristic features of Kolmogorov homogeneous turbulence that is expected to be replicated by solutions to the stochastically forced Burgers equation. The averaged energy spectrum for the Burgers DNS results is plotted in figure 5.19 together with a power-law regression line. Due to the large number of time samples used when averaging, the spectrum is very smooth and appears linear for a large part of the wave number range. The slope of the regression line is -1.630, not that far from the $-\frac{5}{3} \approx 1.667$ result of Kolmogorov turbulence. The linear inertial range persists almost
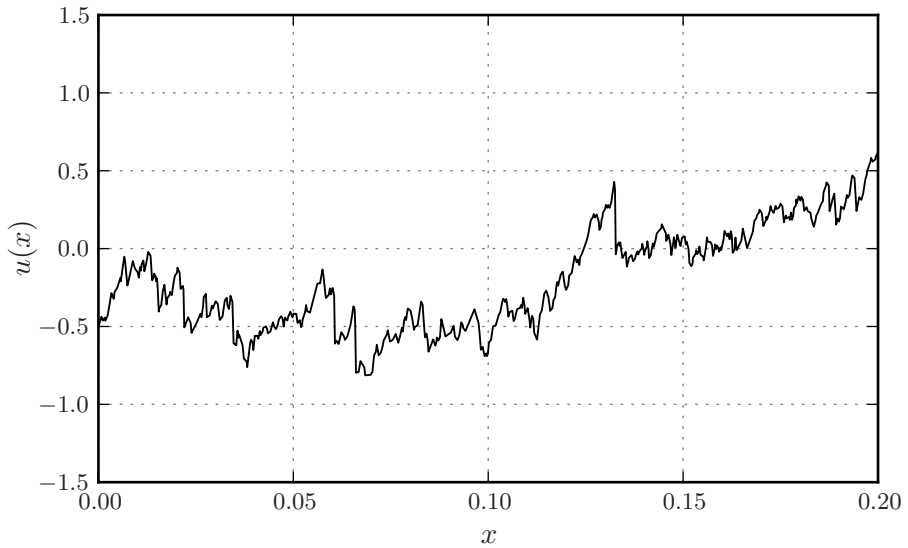
Figure 5.16: Detailed view of velocity at time $t = 2$ for DNS with pink noise source
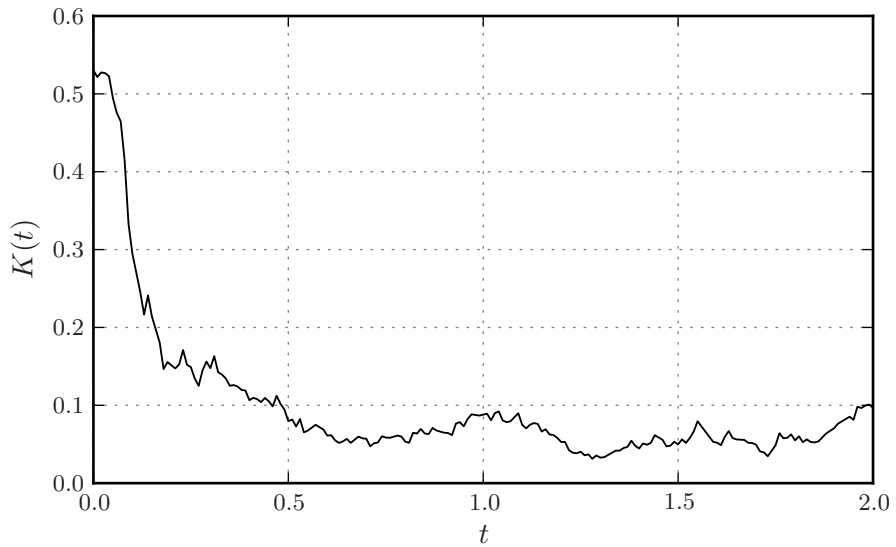
Figure 5.17: Evolution of large scale kinetic energy for $t \in (0, 2)$
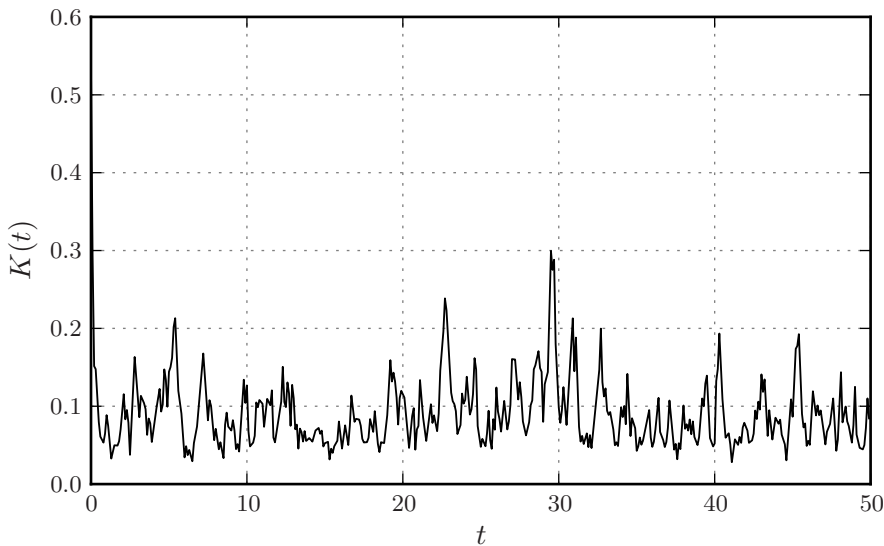
Figure 5.18: Evolution of large scale kinetic energy for $t \in (0, 50)$

to wave number $\kappa = 1000$, beyond which the negative slope is increasing.

Although the energy spectrum slope is quite resemblant of real turbulence, this is hardly enough to qualify as a model system for turbulence. Furthermore, and in particular of higher order, statistics need to be compared in order to assess the validity of the stochastically forced Burgers equation as a model equation for turbulence.

5.3.2 Structure functions

Structure functions of different orders are often used to characterise scaling behaviour and are, as noted in chapter 3, closely related to the multifractal description of turbulence. Here we look at structure functions of order $\frac{1}{3}$ to 8 computed based on simulation results from Burgers DNS. The structure function $S_p(r)$ is plotted as a function of the distance r for structure function orders $\{\frac{1}{3}, \frac{2}{3}, 1, \frac{4}{3}, \frac{5}{3}, 2, 3\}$ in figure 5.20 and orders $\{4, 6, 8\}$ in figure 5.21.

The least squares fit lines are fitted in the interval $r \in (0.01, 0.1)$, corresponding to wave numbers $\kappa \in (10, 100)$. This is the same region used for fitting the least squares fit line for the energy spectrum, and is located entirely within the inertial range. If the scaling exponent of the
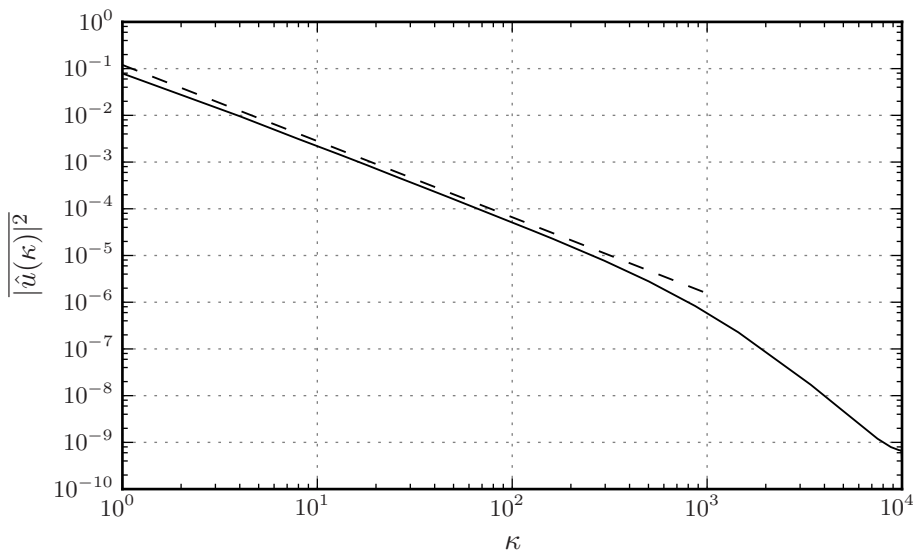
Figure 5.19: Averaged energy spectrum for DNS results (solid line) with power law regression line $\propto \kappa^{-1.630}$ (dashed line) least squares fitted for $\kappa \in (10, 100)$

second order structure function were to be used to determine the slope in the energy spectrum a value of $-1 - 0.613 = -1.613$ would be predicted, quite close but not identical to the value of -1.630 measured from the energy spectrum.

All curves in figure 5.20 appear perfectly smooth and the amount of data used seems sufficient for determining the behaviour of the lower order structure functions. For the three higher order structure functions the curves are less smooth, and for $p = 8$ in particular it seems that an even larger sample would be beneficial. This will inevitably lead to more uncertainty with regards to the predicted slope of the least squares fit line.

All the structure function scaling exponents ζ_p are plotted in figure 5.22 together with similar results from Chekhlov & Yakhot (1995a). The values computed here correspond well with the values determined by Chekhlov & Yakhot (1995a) for the whole range. The deviations are largest for the highest order structure functions, and the values are not completely constant for $p \in (4, 6, 8)$ as found by Chekhlov & Yakhot (1995a). Due to the insufficient data sample for accurately determining the slope of the
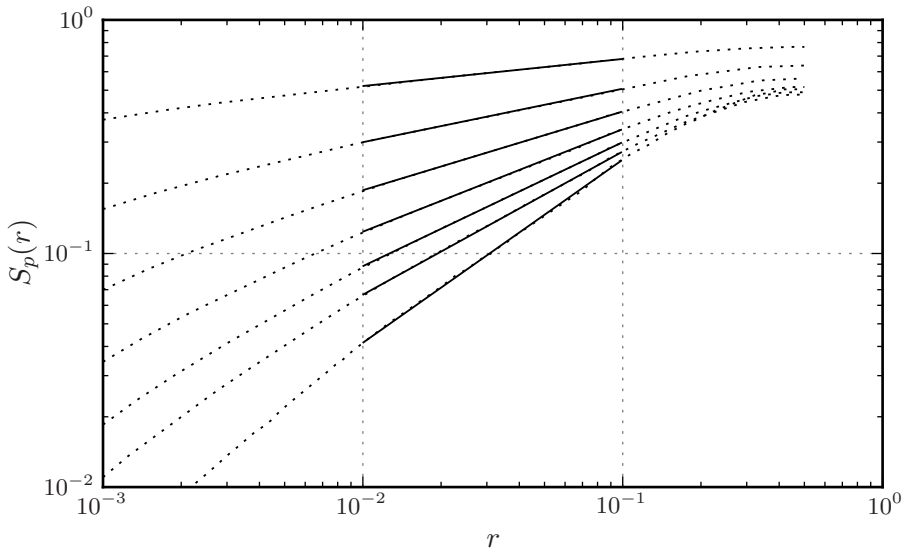
Figure 5.20: Structure functions (dotted lines) of order, from top to bottom, $\frac{1}{3}$, $\frac{2}{3}$, 1, $\frac{4}{3}$, $\frac{5}{3}$, 2 and 3 plotted together with least squares fitted power law (solid lines) fitted for $r \in (0.01, 0.1)$. Slopes of the least squares fits are, from top to bottom, 0.116, 0.229, 0.337, 0.439, 0.531, 0.613 and 0.784.

highest order structure functions, it is difficult to distinguish if this is a significant difference in the results or just a statistical aberration.

Also shown in figure 5.22 are structure function exponents for real three dimensional turbulence, as determined for a jet flow by Anselmet *et al.* (1984) and the theoretical Kolmogorov values of $\frac{p}{3}$. The deviation between the values estimated by Anselmet *et al.* (1984) and $\frac{p}{3}$ is what is referred to as inertial range intermittency and is a popular topic in turbulence research.

Compared with both the estimated values for real turbulence and the theoretical model, the results for Burgers turbulence deviates significantly. For low order structure functions up to around $p = 2$, the results for Burgers turbulence follow $\frac{p}{3}$ quite well. For higher order structure functions, the difference is very large. While the results for real turbulence has a slightly increasing deviation compared with $\frac{p}{3}$ for increasing p, the results from Burgers turbulence are vastly different for structure functions of order larger than 2.

The physical implication of this clear difference, is that small devia-
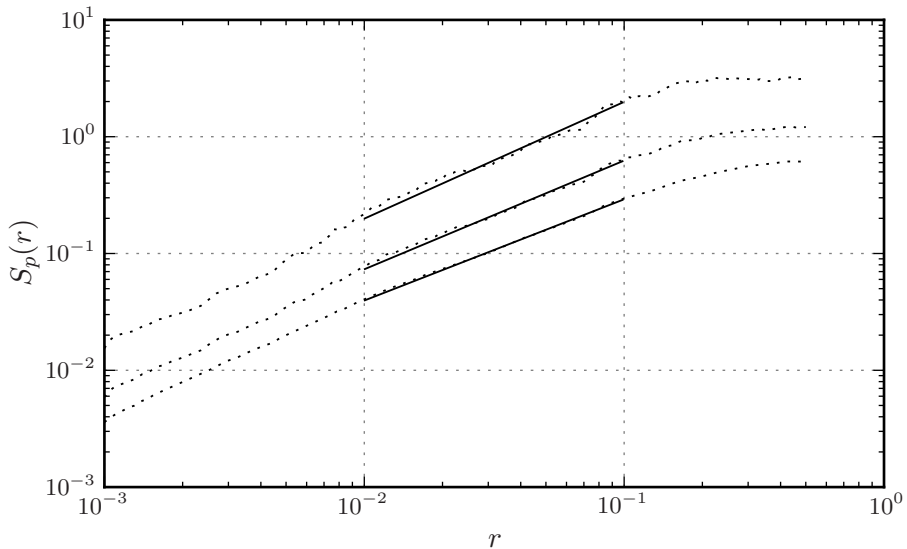
Figure 5.21: Structure functions (dotted lines) of order, from top to bottom, 8, 6 and 4 plotted together with least squares fitted power law (solid lines) fitted for $r \in (0.01, 0.1)$. Slopes of the least squares fits are, from top to bottom, 1.00, 0.931 and 0.867.

tions in the velocity behave quite similarly to theoretical homogeneous Kolmogorov turbulence, while the statistics of larger deviations are completely dominated by shocks. The statistics of higher order structure functions are similar to the constant $\zeta_p = 1$ expected for the standard Burgers equation, and it is obvious that the large shocks are dominating the higher order statistics. One might argue that this considerable difference in the scaling behaviour of higher order structure functions limits the usability of the stochastically forced Burgers equation as a model equation for turbulence.

5.4   Relevance for turbulence

Let us once again recall the energy spectrum of Burgers turbulence for a pink noise source, and consider its resemblance to real turbulence. In real three dimensional turbulence the energy spectrum is the result of an energy cascade from large to smaller scales, caused by the three-dimensional vortex stretching that occurs due to the interaction between different sized eddies.
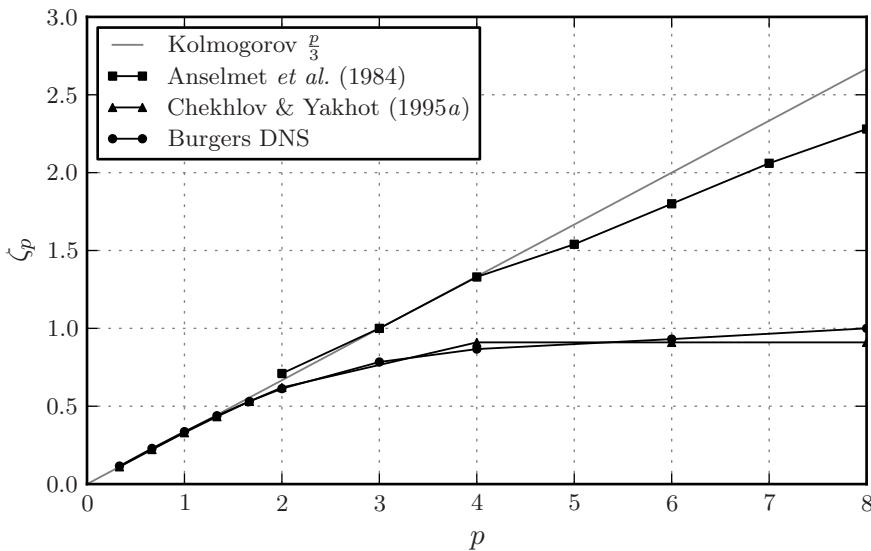
Figure 5.22: Structure function scaling exponents for Burgers DNS results compared with similar results from Chekhlov & Yakhot (1995a), results from three dimensional turbulence (Anselmet *et al.*, 1984) and Kolmogorov $\frac{p}{3}$ turbulence

In one-dimensional Burgers turbulence the concept of a vortex does not exist, but still an energy cascade of some sort occurs. Observing figure 5.15, showing the velocity at time $t = 2$ for the high resolution simulation, some salient features are apparent. The velocity plot is dominated by a few large shocks, and several smaller ones. Both the creation of large shocks and their breakdown into smaller shocks, take place constantly, serving as an energy interaction and transfer between large and small scales. A forcing that is active over a wide range of scales ensures that both processes occur. Because of this, one would expect a certain degree of backscatter, the process of energy being transported from small to larger scales.

An energy spectrum quite resemblant of three-dimensional homogeneous Kolmogorov turbulence is found, and lower order structure functions have scaling exponents following $\frac{p}{3}$. However, the statistics of higher order moments are completely dominated by shocks and are vastly different from the case in three-dimensional turbulence. The lack of similarity in higher order statistics is a serious concern if the stochastically forced Burgers equa-

tion is to be used as a model equation for turbulence.

5.5   LES of Burgers turbulence

The remainder of the report is primarily concerned with subgrid modelling and low resolution simulations. The presented DNS results will be used as a reference when comparing subgrid models. In order to provide a reasonable testing system for subgrid models the numerical methods used must be suited for the task. It has already been pointed out here that low resolution simulations using local Lax-Friedrichs or upwind with MUSCL add excessive numerical dissipation, and adding a subgrid model would only contribute even more dissipation. For the subgrid models to be tested fairly they must be used in a context where they are actually necessary.

Two new convective flux discretisation methods were introduced to be used for the simulations using a subgrid model. These two methods were presented in the last section of chapter 4 and will be tested here. The one cell upwind-biased fixed stencil (see equation 4.40) was used together with an upwind flux function, resulting in a third order upwind-biased method. The skew-symmetric energy conserving method is the second discretisation method tested here.

Simulations for the two new methods as well as the upwind MUSCL methods were run with 250 grid cells $t_{max} = 50$ and otherwise identical parameters as for the DNS. Energy spectra averaged for 5000 time samples between 0 and 50 are plotted in figure 5.23 together with similarly averaged energy spectrum for the DNS.

As before the upwind MUSCL method has too much numerical dissipation. This is largely because the combination of the limiter and a highly irregular velocity causes the method to be first order accurate in a large portion of the domain. When using a third order upwind-biased method without limiting the energy spectrum follows the DNS spectrum for almost the entire range, with only a small deviation at the largest wave numbers. This method has apparently the correct amount of numerical dissipation to not need a subgrid model and still not be excessively dissipative. The skew-symmetric treatment of the convective flux obviously has the least amount of numerical dissipation, and clearly needs a subgrid model to provide usable results.

Based on the energy spectra for the different discretisation methods the skew-symmetric treatment of the convective flux is chosen as the numerical
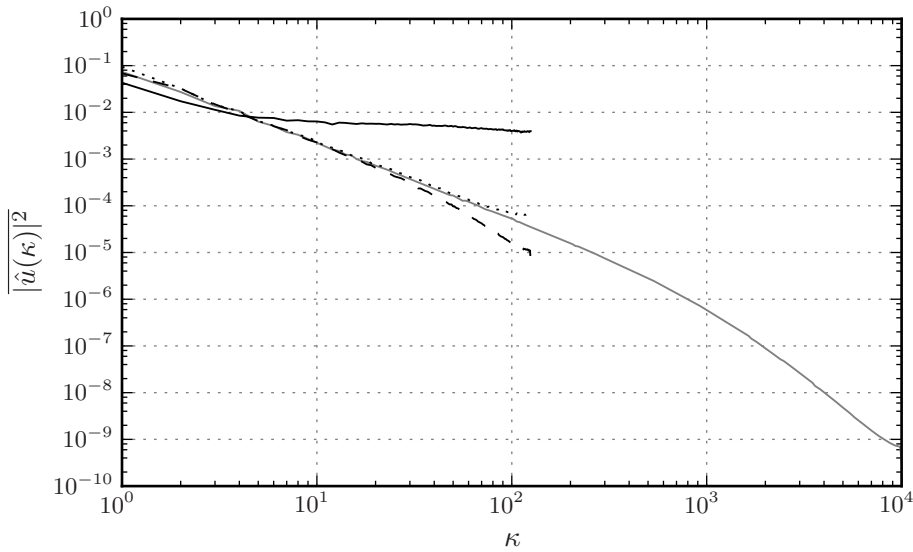
Figure 5.23: Averaged energy spectra for $t \in (0, 50)$ for Burgers DNS (grey line), skew-symmetric flux (solid black line), third order upwind-biased method (dotted line) and upwind MUSCL (dashed line)

method used together with the subgrid models. This numerical treatment has very little numerical dissipation, but does not cause problems with instability or oscillations. The required numerical dissipation to get decent results must then be supplied by the subgrid model.

The upwind-biased method without limiting seems to produce promising results without using a subgrid model. To provide a baseline for what can be achieved with numerical dissipation as the only subgrid model simulations based on this method will be revisited when different subgrid models are compared.

Chapter 6

Modelling turbulence

The chapter gives an introduction to turbulence modelling, and describes different approaches. First the non-modelling approach is explained and then the necessity of modelling is argued for. The two main approaches to modelling in turbulence, temporal averaging and spatial filtering, are then introduced and discussed. Lastly, the type of modelling employed in this thesis is discussed.

Many modern books about fluid dynamics contain chapters on turbulence modelling for the Reynolds-averaged Navier-Stokes equations. Here Versteeg & Malalasekera (2007), Ertesvåg (2000) and Andersson (1988) have been used as references on such models. Geurts (2004) and Meneveau & Katz (2000) have been the main references used for information about the large eddy simulation approach.

6.1   Direct Numerical Simulation

The governing equations for turbulent incompressible flow are the incompressible Navier-Stokes equations (6.1) and the continuity equation (6.2). The density and viscosity are assumed constant.

$$\rho \frac{Du_i}{Dt} = f_i - \frac{\partial p}{\partial x_i} + \mu \frac{\partial^2 u_i}{\partial x_j \partial x_j} \tag{6.1}$$

$$\frac{\partial u_i}{\partial x_i} = 0 \tag{6.2}$$

It is the general belief that these equations represent all aspects of incompressible turbulence, and that solving them numerically introduces

no approximations, other than those inherent in the numerical methods used. This approach is called direct numerical simulation (DNS).

DNS represents the most accurate solution of the governing system of equations conceivable. It is only second in terms of accuracy to an analytical solution, the existence of which is unlikely. The inaccuracies introduced when solving the equations numerically are well understood and controllable.

Using dimensional analysis Kolmogorov (1941b) obtained an estimate for the smallest relevant viscous spatial scale η, and showed that $\frac{\eta}{l} \sim Re^{-\frac{3}{4}}$, where l is a representative large scale. In three dimensions this yields a requirement for total spatial resolution scaling as $Re^{\frac{9}{4}}$. Also accounting for the effect of temporal resolution, the computational work will typically scale as Re^3 for most numerical methods (Geurts, 2004, page 23). This implies that even an increase in computational power on the order of 10^3 only increases the possible Reynolds number by an order of 10.

Due to the multiscale nature of turbulence, DNS requires high spatial and temporal resolution, and the computational requirements are immense for even the simplest turbulent flows. Despite rapid increase in computer power, the use of DNS for high Reynolds number engineering applications is inconceivable in the near future. In order to get solutions for high Reynolds number flows in complex geometries, simplifications are necessary. So, even though the Navier-Stokes equations, with continuity equation and suitable boundary conditions, represent a well-posed problem, they are seldom solved directly.

6.2   The need for models

As already argued, the equations describing turbulence in most applications need approximations in order to be solvable. An approximation to the original differential equation can be obtained by averaging or filtering. Both of these methods will introduce new unknowns, without introducing any new equations. The system of equations will then be underdetermined. The filtered or averaged equations are still exact, but considerable information is lost and the equations are no longer solvable.

In order to solve the system that emerges after initial filtering or averaging, models most be introduced. These models relate the unresolved parts of the problem to the resolved variables by explicitly or implicitly expressing the new unknowns in terms of known quantities. Many of these

models are crude approximations yet employ sophisticated mathematics. Few of these models can be said to yield a general approximation that is good enough for all cases.

6.3 The Reynolds-averaged Navier-Stokes equations

The most common approach to approximate turbulence simulations is using the Reynolds-averaged Navier-Stokes equations. This approach involves averaging the equations in time and modelling the new terms that emerge from this procedure.

6.3.1 Averaging the Navier-Stokes equations

Starting with the conservation form of the incompressible Navier-Stokes equations and continuity equation,

$$\frac{\partial \rho u_i}{\partial t} + \frac{\partial \rho u_j u_i}{\partial x_j} = f_i - \frac{\partial p}{\partial x_i} + \frac{\partial}{\partial x_j}\left(\mu \frac{\partial u_i}{\partial x_j}\right), \tag{6.3}$$

$$\frac{\partial u_i}{\partial x_i} = 0, \tag{6.4}$$

and introducing the Reynolds decomposition

$$u_i = \bar{u}_i + u_i', \tag{6.5}$$

where $\bar{u}_i$ is a temporal average defined as in definition A.2 and u_i' is the deviation. Temporal averaging of both sides of the equation, yields

$$\frac{\partial \rho \bar{u}_i}{\partial t} + \frac{\partial \rho \bar{u}_j \bar{u}_i}{\partial x_j} = \bar{f}_i - \frac{\partial \bar{p}}{\partial x_i} + \frac{\partial}{\partial x_j}\left(\mu \frac{\partial \bar{u}_i}{\partial x_j} - \rho \overline{u_i' u_j'}\right), \tag{6.6}$$

$$\frac{\partial \bar{u}_i}{\partial x_i} = 0. \tag{6.7}$$

This introduces nine new components in the Reynolds stress tensor $\overline{u_i' u_j'}$, but due to symmetry only six new unknowns. In order to solve the system, these unknowns have to be modelled. By time-averaging the Navier-Stokes equation, the models used must represent the effect of all the scales of turbulence on the mean flow.

6.3.2 Eddy viscosity models

As an analogy to Newton's law of viscosity, Boussinesq (1877) proposed that the Reynolds stress components might be proportional to the mean rates of deformation, that is

$$-\rho\overline{u_i'u_j'} = \mu_t \left(\frac{\partial \bar{u}_i}{\partial x_j} + \frac{\partial \bar{u}_j}{\partial x_i} \right) - \frac{1}{3}\rho \overline{u_i'u_i'} \delta_{ij}. \tag{6.8}$$

This effectively reduces the modelling problem to determining a new quantity μ_t called the eddy viscosity or turbulent viscosity.

The assumption that fluid flow can be treated as a continuum is based on the premise that there is substantial scale separation between the largest viscous scales and the mean free path of the molecules. This is well justified as even the smallest scales of turbulence do not approach the molecular scale. However the extension of this principle to turbulent eddies diminishes the physical interpretation. There is an incessant range of different sized eddies that interact continuously, and no distinct scale separation separating the smaller scales from the large scales.

Despite this, the eddy viscosity concept is widely used in turbulence modelling and forms the basis for some of the most used turbulence models. The models for the eddy viscosity range from simple analytical expressions to systems of partial differential equations that needs to be solved together with the RANS equations. The physical foundation of the eddy viscosity and the Boussinesq approximation is however the same.

The models are usually characterised by the number of additional differential equations they introduce. Zero-equation models such as the Prandtl mixing length model (Prandtl, 1945) usually involve prescribing a turbulence related length scale and represent the simplest approach to turbulence modelling. These models do however in some cases correspond well with experimental results, particularly in free shear flows (see Schlichting, 1979, page 741). The Prandtl mixing length model suggests the relation

$$\mu_t = \rho l^2 \left| \frac{\partial u}{\partial x} \right|, \tag{6.9}$$

where l is the prescribed mixing length.

The most common one-equation model introduces a partial differential equation for the turbulence energy k, a measurable turbulence quantity. A prescribed length scale is still required. Two-equation models usually involve the equation for turbulence energy k and an additional equation

for a quantity derived from k and a length scale. The k-ε (Launder & Spalding, 1974) model and the k-ω (Kolmogorov, 1942) model are two of the most popular two-equation eddy viscosity models and prescribe additional equations for dissipation and characteristic frequency, respectively.

While the models with added differential equations usually yield better results than zero-equations models, there is an obvious increase in computational work when additional partial differential equations needs to be solved. Also, despite the added complexity of the eddy viscosity models, these models are still based on the same principle that the eddy viscosity provides a suitable description of turbulence.

6.3.3 Reynolds stress models

Instead of introducing eddy viscosity, the Reynolds stress models model the components of the Reynolds stress tensor directly. This either involves analytical expressions for each component or, for the more complex models, partial differential equations for each component. Introducing six new partial differential equations significantly increases the computational effort required to solve the equations.

The Reynolds stress models using partial differential equations, are however generally regarded as the most accurate models for the RANS equations. Also, modelling the stress tensor directly avoids having to introduce an eddy viscosity or other model quantities that are not measurable.

6.4 Large eddy simulation

Instead of averaging the equations and modelling all scales of turbulence, a large eddy simulation (LES) uses a filtered equation and solves for the largest scales. This preserves more of the physics of turbulence and reduces the task of modelling to the smaller scales. This involves finding a relation between the behaviour of small scales and the behaviour of large resolved scales. The models are usually called subgrid-scale (SGS) models or just subgrid models, as they model the unresolved scales.

The idea of filtering the Navier-Stokes equations and modelling smaller scales appears logical when considering the physics of turbulent eddies. Smaller scales are largely considered to be more general, more isotropic and less geometry dependent than larger scales. The prospect of finding

general models that accurately represent the smaller scales of turbulence
should then be much brighter than that of finding a model that represents
all the scales of turbulence. However, there are numerous different models,
none of which can be expected to produce excellent results for all types of
flow.

6.4.1   Filtering the Navier-Stokes equation

In order to reduce the complexity of the Navier-Stokes equations a spatial
low-pass filter is used to remove the smallest scales (Leonard, 1974;
Germano, 1992). The velocity field is spatially filtered with a convolution
kernel G_Δ, that eliminates all scales smaller than Δ. By applying the filter
$\tilde{(\cdot)}$ to the Navier-Stokes equations the LES equations are obtained

$$\frac{\partial \tilde{u}_i}{\partial t} + \frac{\partial \tilde{u}_j \tilde{u}_i}{\partial x_j} = \frac{1}{\rho}\tilde{f}_i - \frac{1}{\rho}\frac{\partial \tilde{p}}{\partial x_i} + \nu \frac{\partial^2 \tilde{u}_i}{\partial x_j \partial x_j} - \frac{\partial \tau_{ij}}{\partial x_j}, \tag{6.10}$$

$$\frac{\partial \tilde{u}_i}{\partial x_i} = 0, \tag{6.11}$$

where

$$\tau_{ij} = \widetilde{u_i u_j} - \tilde{u}_i \tilde{u}_j. \tag{6.12}$$

As for the RANS equations, the LES equations reduce the range of scales
but introduce new unknowns. For the LES equations the new terms that
need to be modelled are the components of the subgrid stress tensor τ_{ij}.

There are various different filter types that can be utilised when filtering
the Navier-Stokes and many of these are presented in Geurts (2004, chapter
6). The intention of the low-pass filter is to remove the spatial scales
smaller than Δ without significantly altering the scales larger than Δ. The
filter is applied by convolving the filter kernel G_Δ with the velocity, in one
dimension defined as

$$\tilde{u}(x) = \int_{-\infty}^{\infty} G_\Delta(x - \xi)u(\xi)\,d\xi. \tag{6.13}$$

To satisfy the requirement that large scales should not be significantly
affected by the filter, the filter is required to be normalised such that $\tilde{1} = 1$,
i.e. constants are invariant under filtering.

One of the most commonly used filters is the top-hat filter. The top hat
filter is a simple spatial average over the filter width and is in one dimension

expressed as

$$\tilde{u}(x,t) = \int_{x-\frac{\Delta}{2}}^{x+\frac{\Delta}{2}} \frac{u(\xi,t)}{\Delta} \, d\xi \,. \tag{6.14}$$

In most cases an LES is performed either with filter width $\Delta = \Delta x$ or $\Delta = 2\,\Delta x$. It was (according to Geurts (2004, page 288)) found by Kwak (1975) and Love (1980) that $\Delta = 2\,\Delta x$ minimises the total simulation error, and also argued by Liu *et al.* (1994a) that $\Delta = 2\,\Delta x$ is an appropriate choice for the similarity model.

6.4.2 Subgrid-scale models

As for the RANS models, there are a large variety of turbulence models for subgrid scale closure. The most common approach is very similar to the method pursued for the RANS equations, and uses the notion of an eddy viscosity. The most well known of the eddy viscosity models is the Smagorinsky model (Smagorinsky, 1963; Lilly, 1967). The subgrid stress tensor is then related to the filtered velocity field as

$$\tau_{ij} - \frac{1}{3}\tau_{kk}\delta_{ij} = -2\nu_t \tilde{S}_{ij}, \tag{6.15}$$

where

$$\tilde{S}_{ij} = \frac{1}{2}\left(\frac{\partial \tilde{u}_i}{\partial x_j} + \frac{\partial \tilde{u}_j}{\partial x_i}\right) \tag{6.16}$$

is the resolved strain-rate tensor, and ν_t is a prescribed eddy viscosity. The eddy viscosity can be interpreted as the product of a characteristic length scale and a characteristic velocity scale, and is for the Smagorinsky model determined as

$$\nu_t = (C_S\Delta)^2|\tilde{S}|, \tag{6.17}$$

where

$$|\tilde{S}| = \sqrt{2S_{ij}S_{ij}}. \tag{6.18}$$

Several different values for the Smagorinsky constant C_S^2 have been suggested over the years, for several different flow conditions. It is also possible to determine the constant dynamically from the resolved scales. A suggested method to dynamically determine the constant was proposed by Germano *et al.* (1991), and subsequently modified by Lilly (1992). This approach uses an extra test filtering $\overline{(\cdot)}$ and the relation

$$L_{ij} = T_{ij} - \tilde{\tau}_{ij}, \tag{6.19}$$

known as the Germano identity. For the rest of this chapter $\overline{(\cdot)}$ denotes a second filter operator and not temporal averaging. In this equation τ_{ij} is the subgrid stress at filter width Δ, T_{ij} is the subgrid stress at the test filter width $\gamma\Delta$ and the second filter $\overline{(\cdot)}$ denotes filtering at $\gamma\Delta$, with $\gamma > 1$. L_{ij} is expressed as

$$L_{ij} = \overline{\widetilde{u}_i \widetilde{u}_j} - \overline{\bar{\widetilde{u}}}_i \overline{\bar{\widetilde{u}}}_j, \tag{6.20}$$

and is interpreted as the subgrid stress between Δ and $\gamma\Delta$. Assuming scale invariance, C_S^2 is equal for the two filter widths and can be fully determined from the resolved scales.

Inserted for the Smagorinsky model, the Germano identity yields

$$L_{ij} - \frac{1}{3}L_{kk}\delta_{ij} = C_S^2 M_{ij}, \tag{6.21}$$

where

$$M_{ij} = -2\Delta^2 \left(\gamma^2 |\overline{\bar{\tilde{S}}}|\overline{\bar{\tilde{S}}}_{ij} - \overline{|\tilde{S}|\tilde{S}_{ij}}\right). \tag{6.22}$$

Following the error-minimisation approach of Lilly (1992), the coefficient can be determined as

$$C_S^2 = \frac{\langle L_{ij} M_{ij}\rangle}{\langle M_{ij} M_{ij}\rangle}. \tag{6.23}$$

The averaging $\langle (\cdot) \rangle$ can be performed in different ways, but it is quite common to average along a statistically homogeneous direction, as suggested by Germano *et al.* (1991). Without this averaging, C_S^2 tends to vary a lot and can also take negative values. High variations violate the extraction of C_S^2 from the test filter operation, that was done to develop the expression for C_S^2. Negative values will be destabilising for the numerical simulation.

Another entirely different approach to subgrid modelling is the similarity model introduced by Bardina *et al.* (1980). The assumption of scale invariance is used to express the subgrid stress term as

$$\tau_{ij} = C_{sim} = (\overline{\widetilde{u}_i \widetilde{u}_j} - \overline{\bar{\widetilde{u}}}_i \overline{\bar{\widetilde{u}}}_j), \tag{6.24}$$

where $\overline{(\cdot)}$ again represents a second filter.

6.5   Subgrid modelling for the Burgers equation

As for the Navier-Stokes equations, the stochastically forced Burgers equation produces a wide range of scales. But, as a one-dimensional problem

the computational requirements for solving the equation numerically are quite manageable on a modern computer. It can still be useful to filter the equations and solve with a subgrid model, as this might reveal useful information about subgrid modelling in general. A study of subgrid modelling with the Burgers equation was performed by Love (1980), concluding that the tested subgrid models had satisfactory performance.

6.5.1 Filtering the Burgers equation

The Burgers equation is filtered in the same fashion as the Navier-Stokes equations. Starting with the Burgers equation with a source term

$$\frac{\partial u}{\partial t} + \frac{\partial}{\partial x}\left(\frac{1}{2}\tilde{u}^2\right) = \nu\frac{\partial^2 u}{\partial x^2} + g(x,t), \tag{6.25}$$

and filtering with filter width Δ yields

$$\frac{\partial \tilde{u}}{\partial t} + \frac{\partial}{\partial x}\left(\frac{1}{2}\tilde{u}^2\right) = \nu\frac{\partial^2 \tilde{u}}{\partial x^2} + \tilde{g}(x,t) - \frac{1}{2}\frac{\partial \tau}{\partial x}, \tag{6.26}$$

where τ is the subgrid stress

$$\tau = \widetilde{uu} - \tilde{u}\tilde{u}, \tag{6.27}$$

and needs to be modelled. This is very similar to the situation for the three dimensional filtered Navier-Stokes equation.

While the new term τ needs to be modelled, the remaining terms of the equation can be treated as for the non-filtered forced Burgers equation using the numerical methods presented in chapter 4.

6.5.2 Modelling the subgrid stress

Many of the same models used for a three-dimensional LES can also be used with the filtered Burgers equation. The Smagorinsky eddy-viscosity model is in the one-dimensional context reduced to

$$\tau = -2(C_S\Delta)^2 \left|\frac{\partial \tilde{u}}{\partial x}\right|\left(\frac{\partial \tilde{u}}{\partial x}\right). \tag{6.28}$$

The constant C_S can also here be determined using the Germano identity, i.e.

$$C_S^2 = \frac{\langle L_{11}M_{11}\rangle}{\langle M_{11}M_{11}\rangle}, \tag{6.29}$$

where

$$L_{11} = \overline{\tilde{u}\tilde{u}} - \bar{\tilde{u}}\bar{\tilde{u}}, \tag{6.30}$$

and the first $(\widetilde{(\cdot)})$ and second $(\overline{(\cdot)})$ filters denote filtering at scales Δ and $\gamma\Delta$, respectively. For $\gamma = 2$ we get

$$M_{11} = -2\Delta^2 \left(4 \left| \overline{\frac{\partial \tilde{u}}{\partial x}} \right| \left(\overline{\frac{\partial \tilde{u}}{\partial x}} \right) - \overline{\left| \frac{\partial \tilde{u}}{\partial x} \right| \left(\frac{\partial \tilde{u}}{\partial x} \right)} \right). \tag{6.31}$$

The dynamic Smagorinsky model was thoroughly tested by Basu (2009) and has shown to provide satisfactory results for one-dimensional turbulence.

Chapter 7

A fractal subgrid model for the stochastically forced Burgers equation

The chapter presents a fractal subgrid model to be used with low resolution simulations of the stochastically forced Burgers equation.

7.1 Requirements for a subgrid model

It is difficult to determine what in fact makes a good subgrid model and what the primary evaluation parameters should be for such a subgrid model. Perhaps the most obvious requirement would be that the modelled subgrid stress has a high correlation with the exact subgrid stress calculated from high resolution simulations. However, the Smagorinsky model has been shown to have a very poor correlation with the actual subgrid stress for three dimensional simulations (around 0.1–0.2, see Liu *et al.* (1994*a*) and Winckelmans *et al.* (1996)). Despite this the model remains popular, implying that there is more to this than just correlation numbers.

What the Smagorinsky model does succeed in supplying is sufficient dissipation. In a numerical context where the subgrid model is actually required, the primary purpose of the subgrid model is to model the energy interaction with the smaller scales. On average there should be a transport of energy towards the smaller scales, and so the subgrid scale model should on average be an energy sink. The energy lost in the subgrid model is called

the SGS dissipation rate and can in one dimension be defined as

$$\Pi = -\frac{\partial u}{\partial x}\tau. \tag{7.1}$$

A positive SGS dissipation rate corresponds to energy being removed from the larger scales, and vice versa. The energy transfer from smaller to larger scales, where $\Pi < 0$, is known as backscatter.

It is therefore believed that calculating the correct energy transfer, as the primary purpose of the model, is a good indicator of how well the model works. It should however still be noted that a high correlation for the subgrid stress is considered a desirable feature (see e.g Liu *et al.* (1994*a*)), but not a sufficient feature.

An important point is that the required amount of subgrid dissipation in the subgrid model is highly dependent on the type of numerical methods used, and as shown in chapter 5 some numerical methods, typically upwind-biased, already have too much numerical dissipation. This is important to keep in mind because it means that when choosing a subgrid model, the type of numerical methods used should be an important deciding factor.

7.2   Fractal subgrid modelling

Some of the most commonly used types of subgrid models were presented in chapter 6. A very different approach to subgrid modelling is to use the fractal interpolation technique as presented in chapter 3. This method was first suggested by Scotti & Meneveau (1997) and Scotti & Meneveau (1999) and proposed modified by Basu *et al.* (2004*b*). The general idea is to use the notion that velocity graphs in turbulent flow can be described as fractals and then create a fractal interpolation function that has the task to reproduce the small scale features of the velocity. There are many studies suggesting that features of turbulence can be described as fractal (see Sreenivasan (1991)) and Scotti *et al.* (1995) found that the fractal dimension of velocity signals in hydrodynamic turbulence was around 1.7.

The approach suggested by Scotti & Meneveau (1999) consists of using the three points $\{\tilde{u}_{j-1}, \tilde{u}_j, \tilde{u}_{j+1}\}$, and then use the fractal interpolation technique to reconstruct an approximation of the unfiltered velocity. A new variable ξ is used as a substitute for x and is defined such that

$$\xi(x_{i-1}) = 0.0, \quad \xi(x_i) = 0.5, \quad \xi(x_{i+1}) = 1.0. \tag{7.2}$$
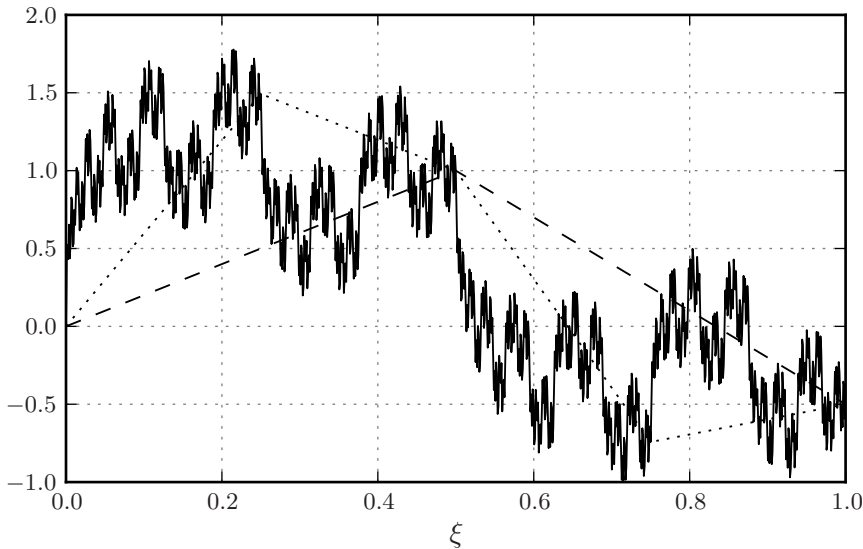
Figure 7.1: Graph of fractal interpolation function after one (dashed line), two (dotted line) and ten (solid line) iterations of the IFS

The interpolation includes the use of an IFS to iteratively construct smaller and smaller scales. The only free parameters for the interpolation function are the d_n stretching factor values. All the other parameters are determined from the stretching factors as shown in chapter 3. For this example there are $N + 1 = 3$ interpolation points and $N = 2$ stretching factors must be determined. Scotti & Meneveau (1999) chose $d_1 = -d_2$ and $|d_1| = |d_2| = 0.794$. Using equation 3.43 this gives a fractal dimension of

$$D = 1 + \log_2(|d_1| + |d_2|) = 1.67, \tag{7.3}$$

the expected fractal dimension of a signal with a $\kappa^{-\frac{5}{3}}$ energy spectrum.

An illustration of this approach is given in figure 7.1, where the interpolated velocity is shown after one, two and ten iterations of the IFS, for $d_1 = 0.794$ and $d_2 = -0.794$.

The subgrid scale stress can then be analytically calculated using the interpolation formulas in chapter 3 and top-hat filtering. Scotti & Meneveau (1999) used a top-hat filter with a filter width of $\Delta = \Delta x$, but here a filter width of $\Delta = 2\Delta x$ will be used. The modelled subgrid scale stress can

then be expressed as

$$\tau = \widetilde{uu} - \tilde{u}\tilde{u} = f_{2,0} - f_{1,0}f_{1,0}, \tag{7.4}$$

where $f_{1,0}$ and $f_{2,0}$ are defined by equation 3.26 and solved in terms of d_n and the interpolation points in equations 3.32 and 3.39, respectively.

The model presented by Scotti & Meneveau (1999) described monofractal fields, due to the choice of equal stretching factors $|d_1| = |d_2|$. This becomes obvious when looking at equation 3.44 as a linear ζ_p is predicted. Because of the expected deviation from monofractality, Basu *et al.* (2004*b*) suggested to use the stretching factors 0.887 and 0.676 chosen to produce interpolation functions with similar multifractal features as real turbulence.

7.3   A two-stage interpolation model

A modified version of the subgrid model presented by Scotti & Meneveau (1999) is presented here.   The fundamental idea of this modification is to create a two-stage interpolation method, where the first stage approximately fixes the overall shape of the interpolation function. The purpose of this first stage is to be able to adjust the amount of dissipation in the model by changing the method used for determining the first step. This is an important feature if the model is to be used with different types of numerical methods, with different varying of numerical dissipation.

The first stage in the interpolation method determines the values in the points $x_{i-\frac{1}{2}}$ and $x_{i+\frac{1}{2}}$, and then the second stage uses the fractal interpolation technique to create an interpolation function for the points $\{\tilde{u}_{j-1}, \tilde{u}_{i-\frac{1}{2}}, \tilde{u}_j, \tilde{u}_{i+\frac{1}{2}}, \tilde{u}_{j+1}\}$. The second stage of the interpolation method uses the same fractal interpolation technique as previously described but now with $N = 4$. A new substituted variable ξ is introduced and defined such that 7.2 holds and

$$\xi(x_{i-\frac{1}{2}}) = 0.25, \quad \xi(x_{i+\frac{1}{2}}) = 0.75. \tag{7.5}$$

An example of the graph of this type of fractal interpolation function is given in figure 7.2, where the first stage is determined using one step of a fractal interpolation function with $d_1 = 0.794$ and $d_2 = -0.794$. The second stage is a multifractal interpolation using $d_1 = 0.6$, $d_2 = -0.8$, $d_3 = 0.52$, $d_4 = -0.6$.
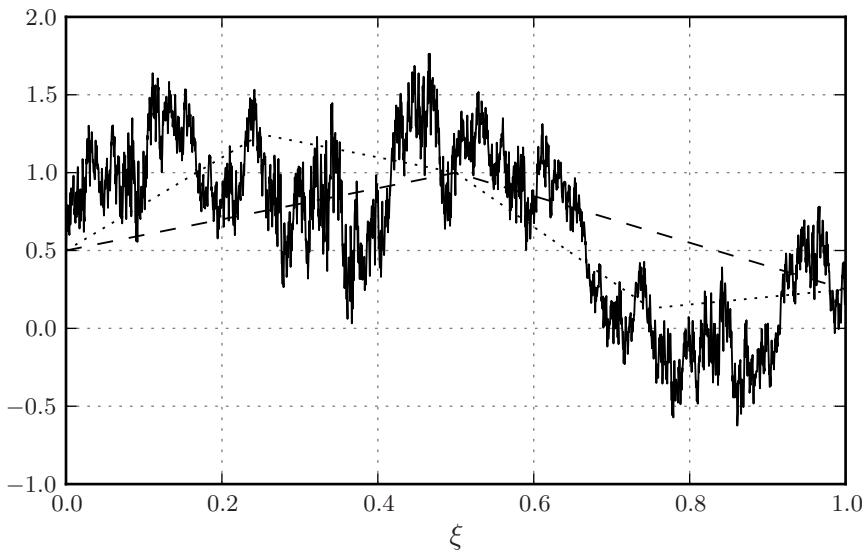
Figure 7.2: Graph of two-stage fractal interpolation function after one (dashed line), two (dotted line) and ten (solid line) iterations of the IFS

There are now four stretching factors d_n that must be determined. These stretching factors are determined using the method suggested by Basu *et al.* (2004b), i.e. using equation 3.43. Using this equation and the ζ_p data for $p \in \{\frac{1}{3}, \frac{2}{3}, 1, \frac{4}{3}, \frac{5}{3}, 2, 3, 4, 6, 8\}$ presented in chapter 5, the stretching factors can be determined. A least squares fit is used to determine the ideal stretching factors as

$$|d_1| = 0.438, \quad |d_2| = 0.438, \quad |d_3| = 0.595, \quad |d_4| = 0.999, \qquad (7.6)$$

or any other permutation of these four absolute values with positive or negative signs. A desirable effect of using four stretching factors instead of two is that one can get a closer fit for the scaling exponents ζ_p.

Figure 7.3 shows the graph of the two-stage fractal interpolation method with four different stretching factor permutations, and with the first stage equal to one step of the fractal interpolation function with $N = 2$ and $d_1 = 0.794$, $d_2 = -0.794$. The four different graphs show that the combination of the four stretching factors greatly affects the resulting interpolation function.

The expression for the subgrid stress term in point x_j using the two-
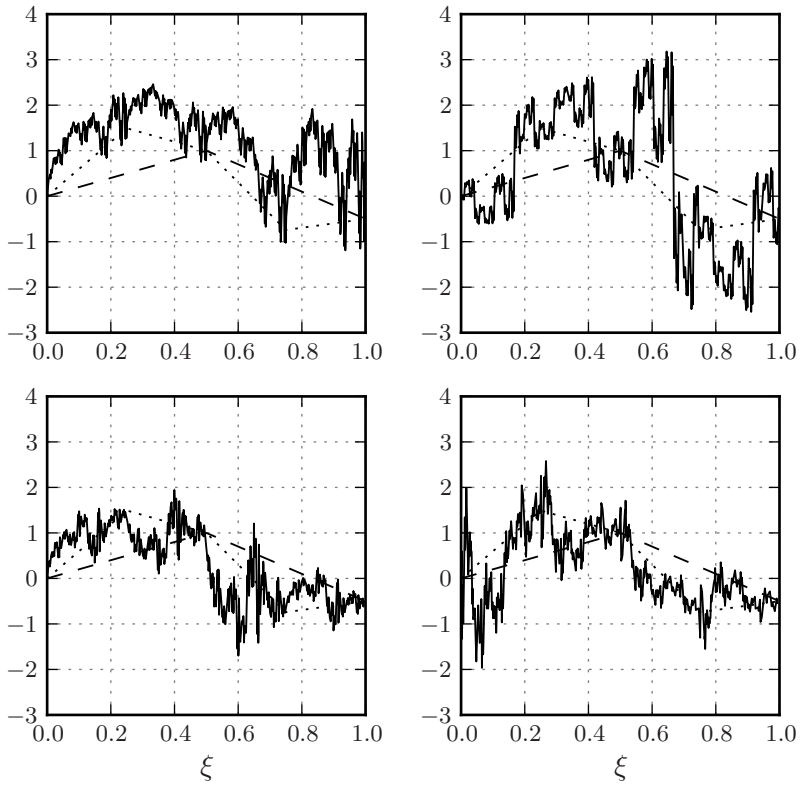
Figure 7.3: Two-stage fractal interpolation method with stretching factors $d_1 = 0.438$, $d_2 = 0.438$, $d_3 = 0.595$ and $d_4 = 0.999$ (upper left); $d_1 = -0.438$, $d_2 = 0.438$, $d_3 = 0.999$ and $d_4 = -0.595$ (upper right); $d_1 = 0.438$, $d_2 = -0.595$, $d_3 = -0.999$ and $d_4 = 0.438$ (lower left); $d_1 = -0.999$, $d_2 = -0.595$, $d_3 = -0.438$ and $d_4 = 0.438$ (lower right)

stage interpolation method and the fractal interpolation function for the second stage is

$$
\begin{aligned}
\tau(x_j) =&\alpha_1\tilde{u}^2_{i+1} + \alpha_2\tilde{u}_{i+\frac{1}{2}}\tilde{u}_{i+1} + \alpha_3\tilde{u}_i\tilde{u}_{i+1} + \alpha_4\tilde{u}_{i-\frac{1}{2}}\tilde{u}_{i+1} + \alpha_5\tilde{u}_{i-1}\tilde{u}_{i+1} \\
&+ \alpha_6\tilde{u}^2_{i+\frac{1}{2}} + \alpha_7\tilde{u}_i\tilde{u}_{i+\frac{1}{2}} + \alpha_8\tilde{u}_{i-\frac{1}{2}}\tilde{u}_{i+\frac{1}{2}} + \alpha_9\tilde{u}_{i-1}\tilde{u}_{i+\frac{1}{2}} + \alpha_{10}\tilde{u}^2_i \\
&+ \alpha_{11}\tilde{u}_{i-\frac{1}{2}}\tilde{u}_i + \alpha_{12}\tilde{u}_{i-1}\tilde{u}_i + \alpha_{13}\tilde{u}^2_{i-\frac{1}{2}} + \alpha_{14}\tilde{u}_{i-1}\tilde{u}_{i-\frac{1}{2}} + \alpha_{15}\tilde{u}^2_{i-1},
\end{aligned}
\tag{7.7}
$$

where the coefficients are determined using equation 7.4 and the prescribed stretching factors.

It was argued and shown by Basu *et al.* (2004*b*) that it was desirable to have stretching factors giving symmetrical stencils. In order to find the stretching factor permutation with the most symmetrical stencil the first stage in the interpolation method was determined with the central method

$$
\tilde{u}_{i-\frac{1}{2}} = \frac{1}{2}(\tilde{u}_{i-1} + \tilde{u}_i), \quad \tilde{u}_{i+\frac{1}{2}} = \frac{1}{2}(\tilde{u}_i + \tilde{u}_{i+1}),
\tag{7.8}
$$

and the coefficients in the new interpolation stencil

$$
\tau(x_j) = \beta_1\tilde{u}^2_{i+1} + \beta_2\tilde{u}_i\tilde{u}_{i+1} + \beta_3\tilde{u}_{i-1}\tilde{u}_{i+1} + \beta_4\tilde{u}^2_i + \beta_5\tilde{u}_{i-1}\tilde{u}_i + \beta_6\tilde{u}^2_{i-1}
\tag{7.9}
$$

were compared. The symmetry of the stencils was determined by how much $\frac{\beta_1}{\beta_6}$ and $\frac{\beta_2}{\beta_5}$ deviated from 1. The two most symmetrical stencils were described by the stretching factors

$$
|d_1| = -0.438, \quad |d_2| = 0.438, \quad |d_3| = 0.999, \quad |d_4| = -0.595,
\tag{7.10}
$$

and the mirrored stretching factors

$$
|d_1| = -0.595, \quad |d_2| = 0.999, \quad |d_3| = 0.438, \quad |d_4| = -0.438,
\tag{7.11}
$$

with

$$
\max\left(\frac{\beta_1}{\beta_6}, \frac{\beta_6}{\beta_1}, \frac{\beta_2}{\beta_5}, \frac{\beta_5}{\beta_2}\right) = 1.01.
\tag{7.12}
$$

The resulting stencils using these stretching factors are

$$
\begin{aligned}
\alpha_1 &= 0.3827, \quad \alpha_2 = -0.4400, \quad \alpha_3 = -0.5822, \\
\alpha_4 &= -0.1762, \quad \alpha_5 = 0.4332, \quad \alpha_6 = 0.3581, \\
\alpha_7 &= 0.1876, \quad \alpha_8 = -0.2444, \quad \alpha_9 = -0.2194, \\
\alpha_{10} &= 0.3932, \quad \alpha_{11} = 0.1998, \quad \alpha_{12} = -0.5915, \\
\alpha_{13} &= 0.2661, \quad \alpha_{14} = -0.3113, \quad \alpha_{15} = 0.3445,
\end{aligned}
\tag{7.13}
$$

and the mirror version

$$\alpha_1 = 0.3445, \quad \alpha_2 = -0.3113, \quad \alpha_3 = -0.5915,$$
$$\alpha_4 = -0.2194, \quad \alpha_5 = 0.4332, \quad \alpha_6 = 0.2661,$$
$$\alpha_7 = 0.1998, \quad \alpha_8 = -0.2444, \quad \alpha_9 = -0.1762, \tag{7.14}$$
$$\alpha_{10} = 0.3932, \quad \alpha_{11} = 0.1876, \quad \alpha_{12} = -0.5822,$$
$$\alpha_{13} = -0.3581, \quad \alpha_{14} = -0.4400, \quad \alpha_{15} = 0.3827.$$

These are the two stencils used for all subgrid models using the two-stage fractal interpolation model. One of the two stencil versions is chosen randomly with equal probability, for each grid cell j.

The initial guess for the first stage of the two-stage interpolation was to use one step of the fractal interpolation function with $|d_1| = |d_2| = 0.794$, $d_1 = -d_2$ and signs chosen randomly. The extra interpolation points $\{\tilde{u}_{j-\frac{1}{2}}, \tilde{u}_{j+\frac{1}{2}}\}$ were then determined as

$$\tilde{u}_{j-\frac{1}{2}} = \frac{1}{2}(\tilde{u}_{j-1} + \tilde{u}_j) - \frac{1}{2}d_1(\tilde{u}_{j-1} - 2\tilde{u}_j + \tilde{u}_{j+1}), \tag{7.15}$$

and

$$\tilde{u}_{j+\frac{1}{2}} = \frac{1}{2}(\tilde{u}_j + \tilde{u}_{j+1}) - \frac{1}{2}d_2(\tilde{u}_{j-1} - 2\tilde{u}_j + \tilde{u}_{j+1}). \tag{7.16}$$

The described subgrid model was then tested on filtered DNS results to see how closely it fitted the subgrid scale stress calculated from DNS results for $NJ = 250$ cells. The result can be seen in figure 7.4, where the modelled subgrid stress appears predict a subgrid stress with similar features as the exact subgrid stress. The peaks are however much too low. To test the subgrid model in an actual simulation context, it was implemented in a low resolution simulation with 250 grid cells and the skew-symmetric treatment of convection. The simulation quickly diverged, implying that the subgrid model did not satisfy its main task of adding dissipation, but instead destabilised the simulation.

7.4   Modified interpolation model

Due to the unsatisfactory performance of the first incarnation of the two-stage model, changes were implemented to increase the total dissipation of the simulation. Two different approaches were tested, local maximisation and a mixed model.
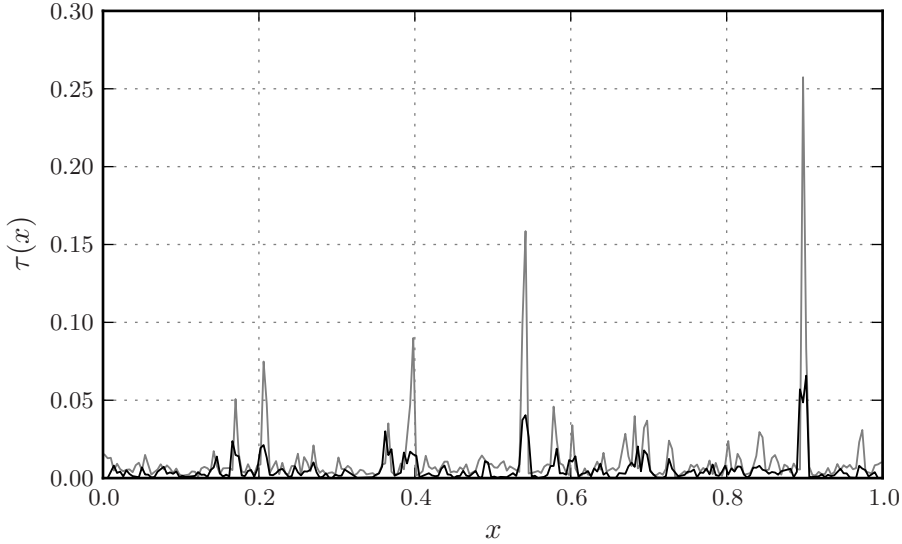
Figure 7.4: Plotted subgrid scale stress showing for Burgers DNS (grey line) and the first incarnation of the two-stage fractal interpolation model (black line)

7.4.1 The local maximisation approach

In order to increase the amount of dissipation contributed by the subgrid model, the amount of dissipation is locally maximised. The first stage of the two-stage method implements the fixed stencil interpolation functions presented in section 4.8. Different values of the two velocities $\{\tilde{u}_{j-\frac{1}{2}}, \tilde{u}_{j+\frac{1}{2}}\}$ are then computed using these four different fixed stencil interpolation functions. The second stage of the interpolation uses the same fractal interpolation function as before.

In order to maximise dissipation, four different values of the subgrid scale stress are calculated from the four different stencils. The one with the maximum amount of dissipation is chosen. This is implemented as

$$\tau = -\sigma \max(-\sigma\tau^a, -\sigma\tau^b, -\sigma\tau^c, -\sigma\tau^d), \tag{7.17}$$

where

$$\sigma = \text{sign}(u_{j+1} - u_{j-1}). \tag{7.18}$$

7.4.2   The mixed model approach

The mixed model approach consists of using a combination of the fractal interpolation model and a Smagorinsky model. The first stage of the interpolation is determined using one cell upwind-biased interpolation functions from 4.8. The second stage is the same as before. The subgrid scale stress is then computed as the maximum of the stress from the fractal model and the stress from the Smagorinsky model.

This is implemented as

$$\tau = \max(\tau^{\mathrm{frac}}, \tau^{\mathrm{Smag}}), \tag{7.19}$$

where τ^{Smag} is defined in equation 6.28 and a constant coefficient $C_S^2 = 0.28$ is used.

Chapter 8

Results and discussion

The chapter presents the most important results for the subgrid model tests. First the subgrid models ability to recreate the subgrid stress is tested by comparing the subgrid stress calculated from filtered DNS results. Then the subgrid model is tested in actual simulations where the statistical features of the velocity are compared with DNS results.

8.1 Specifications

All numerical methods and subgrid models used here are introduced and explained in previous chapters. A short summary is however given here for clarity. All DNS results refer to the simulation presented in detail in section 5.3, and all low resolution simulations use the same set of parameters.

There are three subgrid models tested, the multifractal model with local dissipation maximisation (labelled MF), the mixed Smagorinsky multifractal model (labelled MFS) and the dynamic Smagorinsky model (labelled DS). All simulations using subgrid models utilise the energy conserving skew-symmetric treatment of the convection term. In addition to simulations using these three subgrid models, a simulation using the third order one cell upwind-biased method without subgrid modelling is studied (labelled NS). Values directly computed from DNS results are used as a reference (labelled DNS).

8.2   Correlation studies

The task of a subgrid model in the Burgers equation is to model the subgrid stress term

$$\tau = \widetilde{uu} - \tilde{u}\tilde{u}, \tag{8.1}$$

in the filtered equation. The subgrid stress is easily calculated from DNS results using this definition, and ideally a subgrid model should predict the same values using the filtered velocity. To test the merit of a subgrid model without doing actual simulations using the model, one can calculate the modelled subgrid scale stress from filtered DNS results and compare it with the exact subgrid stresses calculated using equation 8.1.

The reference subgrid stress values τ_{DNS} are calculated from the DNS results using a top hat filter with filter width $\Delta = 2\,\Delta x = \frac{2}{25} =$ and the definition of the subgrid stress (equation 8.1). The modelled stresses are calculated by applying the subgrid models to the top-hat filtered DNS velocity. The exact and modelled subgrid stresses are calculated for all 950000 time samples for $t \in (50, 1000)$ and statistics are computed by averaging over all time samples.

Before computing the statistical correlation between the exact and modelled subgrid stress, a visual comparison of the actual subgrid stresses is studied. Figures 8.1, 8.2 and 8.3 show the computed subgrid stress compared with the exact DNS subgrid stress at time $t = 200$ for models MF, MFS and DS, respectively. This is a simple way of studying how well the general features of the subgrid stress are represented in the different models.

Figure 8.1 shows that the modelled subgrid stress τ_{MF} in general follows the exact stress τ_{DNS} but fails to reach the maximum values of the sharpest peaks. Both τ_{DNS} and τ_{MF} are strictly positive, which means that the stress values corresponding with positive gradients will cause backscatter.

Figure 8.2 shows that the modelled subgrid stress τ_{MF} appears to correspond well with the exact stress τ_{DNS}, but the peaks are too large. Also for this model the subgrid stress τ_{MFS} is strictly positive, and backscatter is expected.

The third modelled stress τ_{DS} is shown in figure 8.3 with a distinctive difference. The model predicts both positive and negative values, despite the exact stress τ_{DNS} being strictly positive. This makes the graph of the modelled subgrid stress τ_{DS} overlap less with the graph of τ_{DNS}, but the peaks appear to be correctly placed.
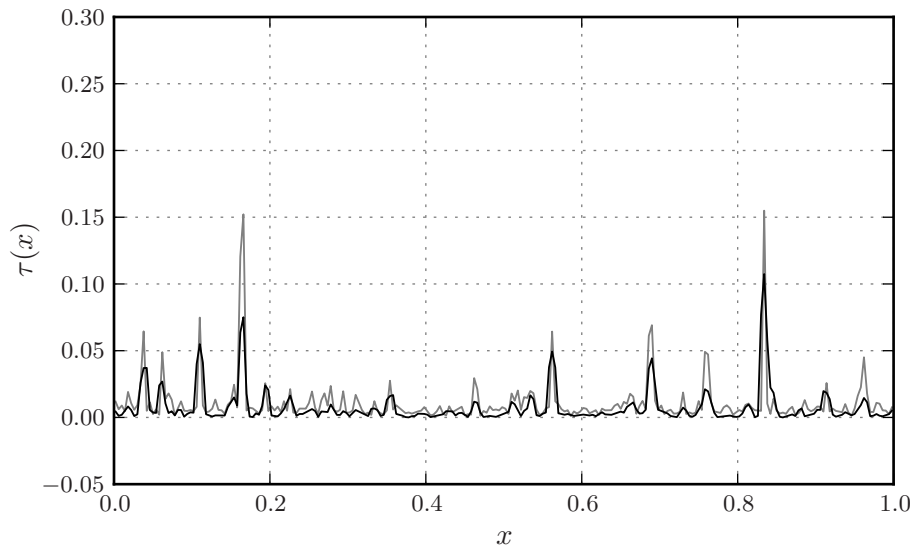
Figure 8.1: Modelled subgrid stress using MF model τ_{MF} (black line) compared with exact subgrid stress τ_{DNS} (grey line) at time $t = 200$
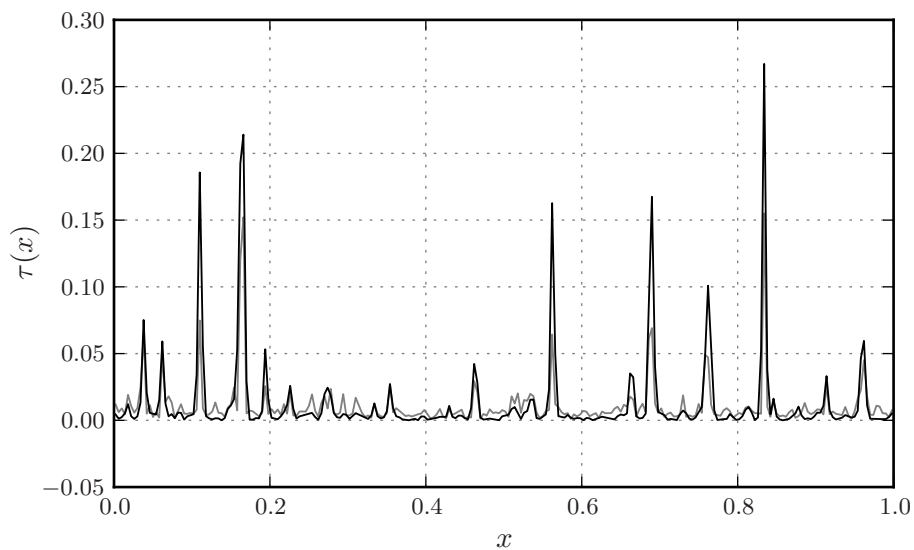
Figure 8.2: Modelled subgrid stress using MFS model τ_{MFS} (black line) compared with exact subgrid stress τ_{DNS} (grey line) at time $t = 200$
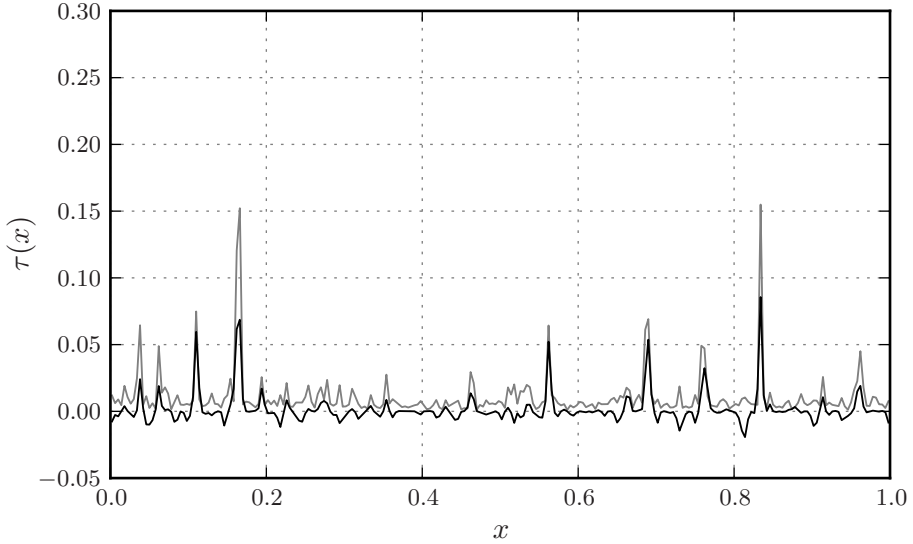
Figure 8.3: Modelled subgrid stress using DS model τ_{DS} (black line) compared with exact subgrid stress τ_{DNS} (grey line) at time $t = 200$

All three models predict subgrid stresses that seemingly correlate quite well with the DNS stress. Although neither of the models generally predict exact values at the peaks, most peaks are correctly located. Although it can not be stated that these types of plots generally exhibit much detailed information, the most visible features are well represented. None of the models stand out notably, they are neither better nor worse than the other models, and it is difficult to determine which model most successfully compares with τ_{DNS}. The most markedly different of the three models is the DS model with the negative values of τ_{DS}.

To reveal more about the local dynamics of the subgrid models the local subgrid dissipation rate $\Pi(x)$ is calculated and plotted for all three subgrid models. Graphs of $\Pi(x)$ for models MF, MFS and DS are compared with $\Pi_{\mathrm{DNS}}(x)$ at time $t = 200$ in figures 8.4, 8.5 and 8.6, respectively. The characteristics of the subgrid dissipation is an important feature for a subgrid model, as this accounts for the energy transfer of the model. Since perhaps the most important task of the subgrid model is to model the transfer of energy to smaller scales, it is important that the subgrid dissipation is correctly predicted.
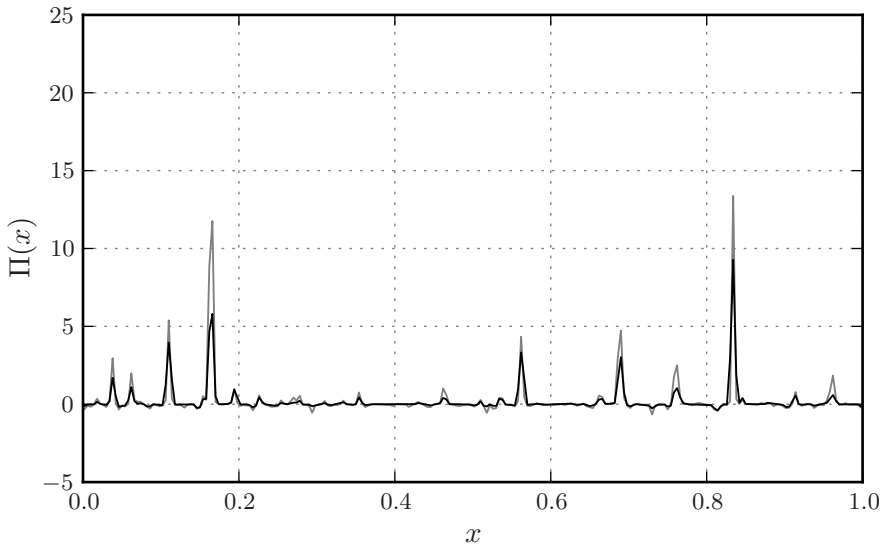
Figure 8.4: Modelled subgrid dissipation using MF model Π_{MF} (black line) compared with exact subgrid dissipation Π_{DNS} (grey line) at time $t = 200$

In figure 8.4 the subgrid dissipation for the MF model $\Pi_{MF}(x)$ is compared with $\Pi_{DNS}(x)$, and appears to match quite well, although the maximum dissipation values are lower than those of $\Pi_{DNS}(x)$. Small negative peaks are seen for both $\Pi_{DNS}(x)$ and $\Pi_{MF}(x)$ showing the existence of backscatter.

Backscatter is also seen in figure 8.5, showing the subgrid dissipation of the MFS model $\Pi_{MFS}(x)$ compared with $\Pi_{DNS}(x)$. In general the modelled subgrid dissipation appears to show good correlation with the exact subgrid dissipation, but for this model the peaks are too large.

The dissipation of the DS model $\Pi_{DS}(x)$ is compared with $\Pi_{DNS}(x)$ in figure 8.6, and also here the most characteristic features appear to be well represented. Due to the predicted negative subgrid stress in regions of positive velocity gradient the subgrid dissipation of the DS model $\Pi_{DS}(x)$ is strictly positive.

Once again, none of the three models stand out, and once again it is difficult to conclude on a preferred model from these plots. The lack of backscatter for the DS model is the most significant difference, but considering how small the negative dissipation peaks are, it is not sure
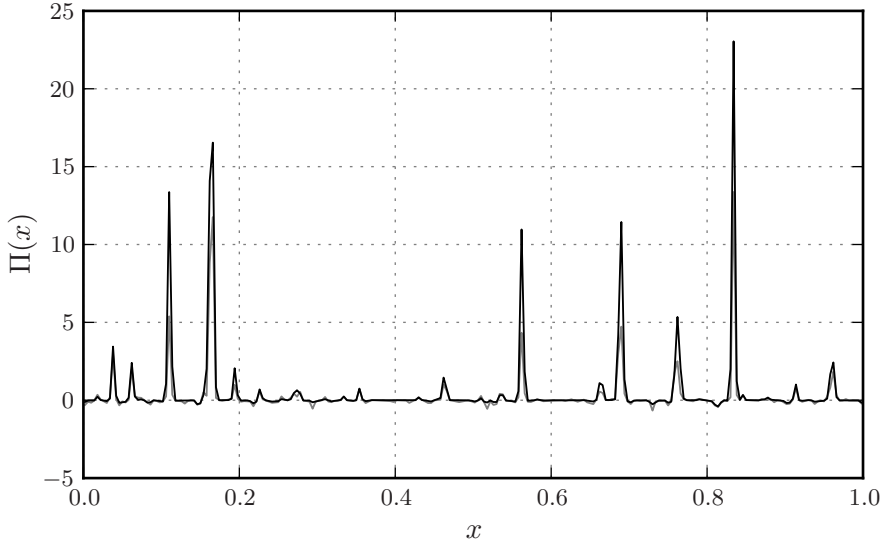
Figure 8.5: Modelled subgrid dissipation using MFS model Π_{MFS} (black line) compared with exact subgrid dissipation Π_{DNS} (grey line) at time $t = 200$

how important this is.

Both the subgrid stress and the dissipation plots show graphs with very characteristic large scale features, corresponding with the largest shocks in the solution. One might assume that the prediction of very large peaks in the dissipation plots dominates the overall energy balance. All three models tested here manage to correctly place the local maxima, but fail to predict the correct values. The overall intermittent features are preserved, but the actual values are often significantly different. If these large peaks dominate the overall energy balance, then this might cause a problem. Even though the largest peaks are the most important for the global energy balance, the small scale features are essential for the local energy balance. Incorrect dissipation on a local level, for instance excessive backscatter, could cause local oscillations.

There is a limit to the amount of knowledge one can extract from the performance of a subgrid model by studying one single time sample. To get a more complete understanding of how well the modelled subgrid stress matches the exact subgrid stress, the commonly used correlation coefficient
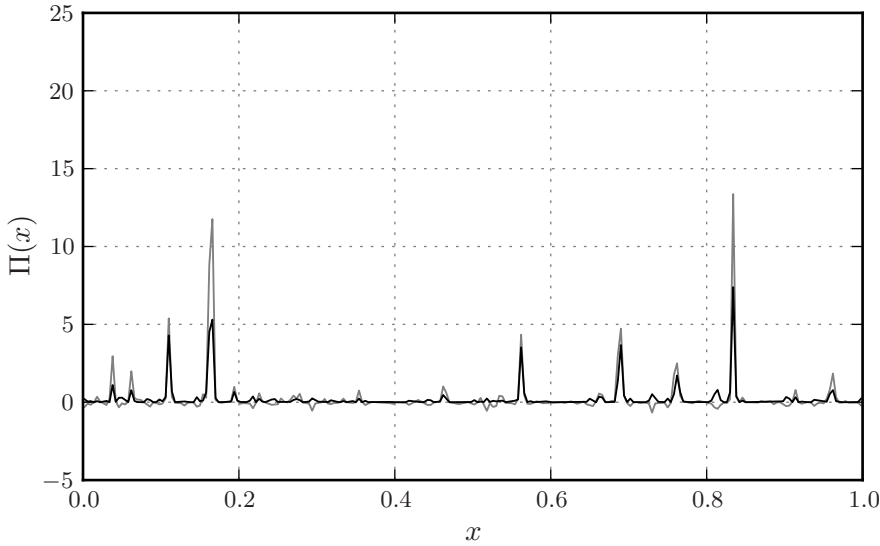
Figure 8.6: Modelled subgrid dissipation using DS model Π_{DS} (black line) compared with exact subgrid dissipation Π_{DNS} (grey line) at time $t = 200$

was computed for all the three subgrid models. The correlation coefficient (defined in section A.3.3) measures how well the two variables fit a linear relation. A correlation equal to 1 implies that the data points all perfectly fit a linear line. As mentioned before, high correlation is considered a desirable feature for a subgrid model. The correlation coefficients are computed using all available temporal and spatial data points.

Correlation results for both $\text{corr}(\tau_{\text{model}}, \tau_{\text{DNS}})$ and $\text{corr}(\Pi_{\text{model}}, \Pi_{\text{DNS}})$ are presented in table 8.1 for all three subgrid models. All six correlation coefficients are much larger than expected. All three models have higher correlation coefficients for the subgrid dissipation, and the model with the highest correlation is the MFS model. Considering that the standard Smagorinsky model is known to show correlation coefficients around 0.1–0.2 (Liu *et al.*, 1994*a*) for real turbulence, the correlation coefficients shown here are surprising. Correlation coefficients in excess of 0.9 are shown for both subgrid stress and subgrid dissipation for the DS model, perhaps suggesting that this model is more successful in reproducing the characteristics of one-dimensional turbulence

The correlation coefficients for all three models are so high that it might

	MF	MFS	DS
$\mathrm{corr}(\tau_{\mathrm{model}}, \tau_{\mathrm{DNS}})$	0.830	0.943	0.916
$\mathrm{corr}(\Pi_{\mathrm{model}}, \Pi_{\mathrm{DNS}})$	0.943	0.978	0.967

Table 8.1: Correlation coefficients for modelled subgrid stress τ_{model} and modelled subgrid dissipation Π_{model} for subgrid models MF, MFS and DS

be tempting to suggest that all three models provide excellent fits to the DNS results. As will be shown, this is not necessarily so. If one were to choose a subgrid model solely based on the correlation coefficient then the MFS model has the most promising results. Clearly, the information that can be extracted from a single number does not provide sufficient basis for selecting the best subgrid model.

To getter a better idea of how well the models actually correlate with the exact subgrid stress, a more visual approach is used. While the correlation coefficient measures how well $\mathrm{corr}(\tau_{\mathrm{model}}, \tau_{\mathrm{DNS}})$ fits any straight line, the information of interest is how well it fits the line $\tau_{\mathrm{model}} = \tau_{\mathrm{DNS}}$. To investigate how closely the data fits, the modelled subgrid stress is plotted against the exact subgrid stress in figures 8.7, 8.8 and 8.9, respectively. The coordinates $(\tau_{\mathrm{model}}, \tau_{\mathrm{DNS}})$ are plotted as scatter points together with the ideal linear relation $\tau_{\mathrm{model}} = \tau_{\mathrm{DNS}}$. The desired result is that the points fit as closely as possible to the line, and the position will say something about how well the modelled results compare with the exact results.

The correlation plot of the MF model is shown in figure 8.7. There is a very strong clustering of the points, with a few scattered points. This clustering is expected considering the small number of very large values in the previously presented subgrid stress plots. Most of the data seems to be fairly well fitted to a linear regression line, thus explaining the large correlation coefficient. The data does however not fit the straight line plotted in the figure. For the smallest values the points seem approximately symmetrically distributed about the straight line, but as the values increase the asymmetry increases. The largest subgrid stress values are consistently under-predicted, as indicated earlier by the subgrid stress plot. Despite the large correlation coefficient the correlation suggested in figure 8.7 is far from excellent. Although most points are in close proximity to the line $\tau_{\mathrm{MF}} = \tau_{\mathrm{DNS}}$, the overall trend is wrong.

A similar correlation plot of the MFS model is shown in figure 8.7. As

Figure 8.7: Coordinates $(\tau_{\mathrm{MF}}, \tau_{\mathrm{DNS}})$ plotted as scatter points and compared with the linear line $\tau_{\mathrm{MF}} = \tau_{\mathrm{DNS}}$

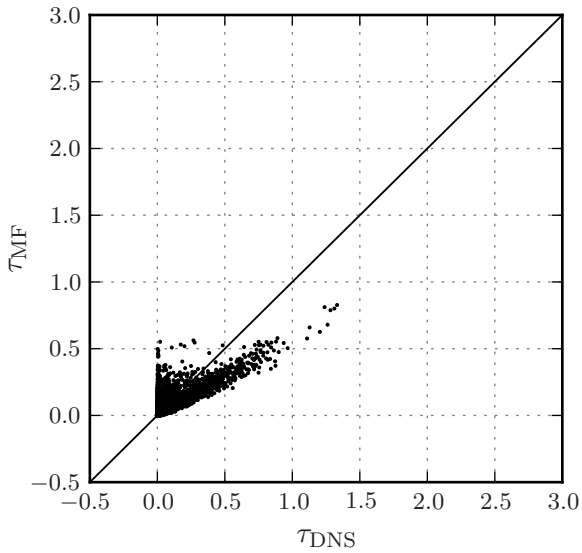Figure 8.8: Coordinates $(\tau_{\mathrm{MFS}}, \tau_{\mathrm{DNS}})$ plotted as scatter points and compared with the linear line $\tau_{\mathrm{MFS}} = \tau_{\mathrm{DNS}}$
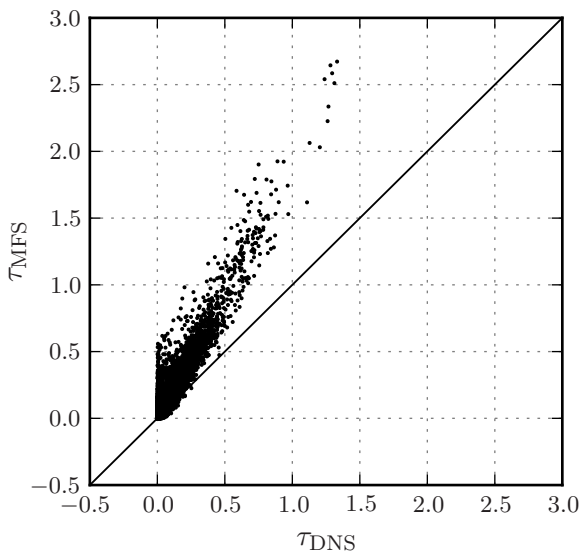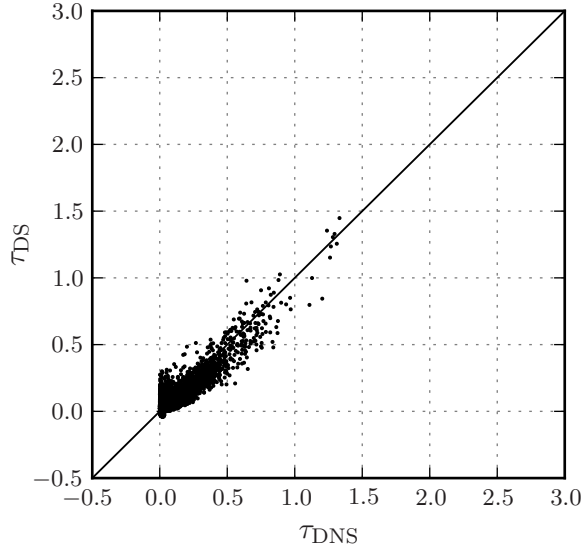
Figure 8.9: Coordinates (τ_{DS}, τ_{DNS}) plotted as scatter points and compared with the linear line $\tau_{DS} = \tau_{DNS}$

expected from the large correlation coefficient the data appears to follow a linear line well. However, this time almost all points fall above the line $\tau_{MFS} = \tau_{DNS}$, indicating that the model consistently over-predicts the subgrid stress. The slope is also wrong and larger values of the subgrid stress are increasingly over-predicted.

The correlation plot of the DS model is shown in figure 8.12, and appears to be the most promising of the three. It is evident that the points are much more symmetrically distributed about the line $\tau_{DS} = \tau_{DNS}$ than the previous two models, which is clearly desireable. There is also here quite a bit of scattering and most points do seem to fall below the desired linear regression line. What makes this correlation plot the most promising is that the general trend of the data fits the trend of the line $\tau_{DS} = \tau_{DNS}$.

As for the subgrid stress, the subgrid dissipation is plotted in correlation plots in figures 8.10, 8.11 and 8.12, respectively. Similar trends emerge as for the subgrid stress correlation plot, and most previous observations also apply here. The MF model predicts dissipation values that are quite consistently too low and the MFS model predicts values consistently too high. All three models appear to fit a linear line quite well, but only the DS
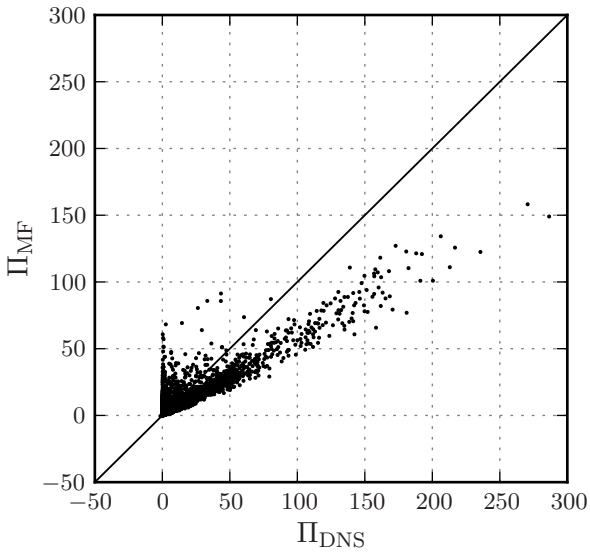
Figure 8.10: Coordinates (Π_{MF}, Π_{DNS}) plotted as scatter points and compared with the linear line $\Pi_{MF} = \Pi_{DNS}$
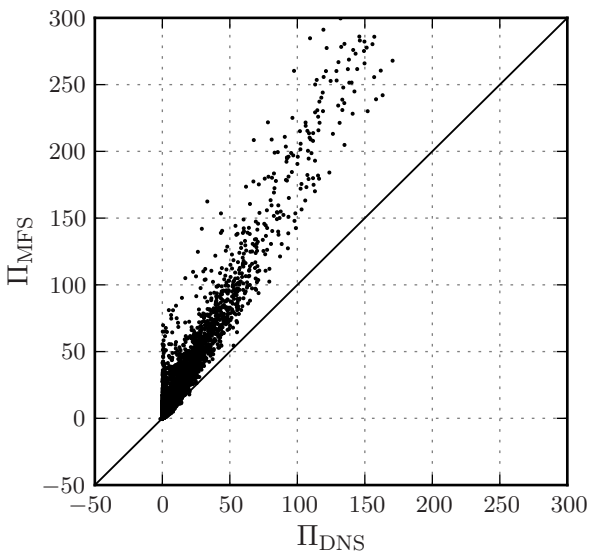

Figure 8.11: Coordinates (Π_{MFS}, Π_{DNS}) plotted as scatter points and compared with the linear line $\Pi_{MFS} = \Pi_{DNS}$
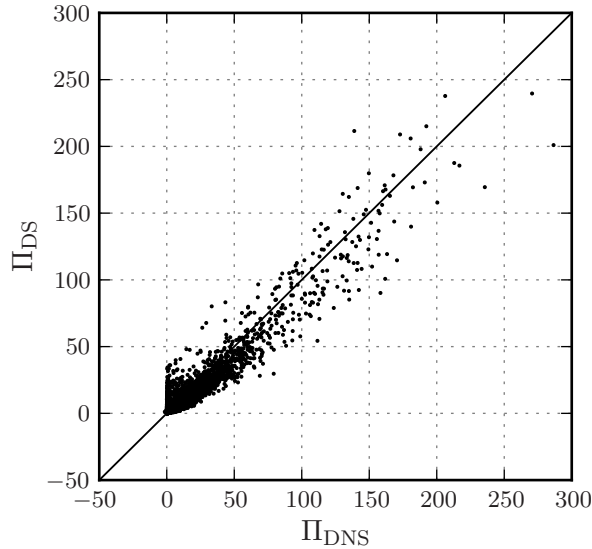
Figure 8.12:   Coordinates (Π_{DS}, Π_{DNS}) plotted as scatter points and compared with the linear line $\Pi_{DS} = \Pi_{DNS}$

model shows the desired trend. The coordinates (Π_{MF}, Π_{DNS}) consistently fall below the line $\Pi_{MF} = \Pi_{DNS}$, while the coordinates (Π_{MFS}, Π_{DNS}) consistently fall above the line $\Pi_{MFS} = \Pi_{DNS}$. The coordinates (Π_{DS}, Π_{DNS}) are approximately symmetrically distributed about the line $\Pi_{DS} = \Pi_{DNS}$.

Neither of the shown correlation plots seem to show excellent data fit, contradictory to the very high correlation coefficients presented earlier. It is worth mentioning once again that the correlation coefficient actually measures the degree to which the data fits a straight line. This is a good example of how little information one can obtain from the statistical correlation of two variables, based on the correlation coefficient alone. The data can fit a linear line excellently, and thus have a high correlation coefficient, however it does not follow that two variables tend to have the same values.

Better fits in the correlation plots for the MF and MFS models could be achieved by multiplying the model by a coefficient, but this would not necessarily yield better results in actual simulations. It still remains to be seen how important it is to have a model that predicts a subgrid stress that is highly correlated with the exact subgrid stress, and whether or not the
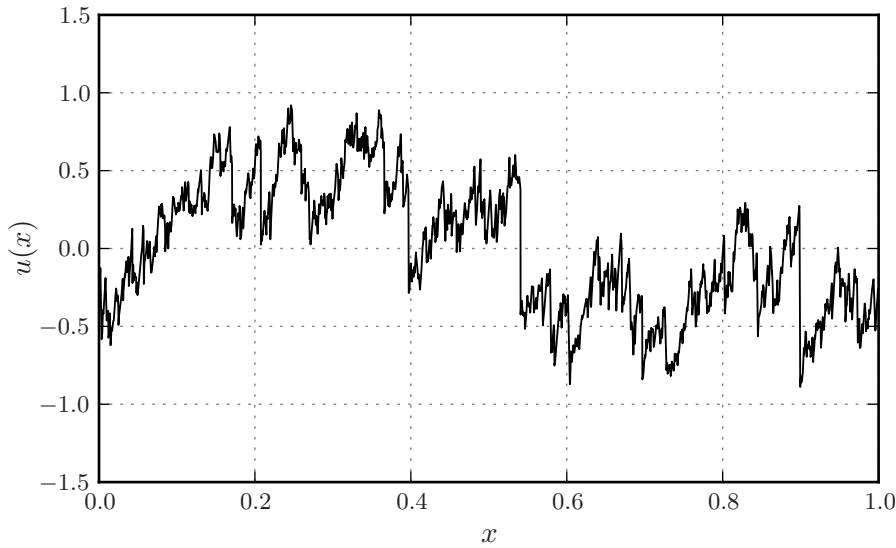
Figure 8.13: Graph of velocity at time $t = 100$ for DNS simulation

models with the most appealing correlation features give the best results in actual simulations.

8.3 Statistical features of simulation results

Although useful information about the performance of a subgrid model is revealed when studying the correlation with the exact subgrid stress, the ultimate test of the quality of a subgrid model is to test its performance in actual simulations. All three subgrid models MF, MFS and DS are therefore tested in low resolution simulations and the results are compared with the high resolution DNS simulation and the low resolution simulation without subgrid model NS.

Because filtered equations are solved one could argue that it would be most appropriate to compare the results with filtered DNS results. However, the velocity fields in the simulations are not explicitly filtered. The top-hat filtering procedure only enters into the subgrid model. Filtering is used to derive the subgrid stress for the fractral interpolation function, and it is used to determine the constant in the dynamic Smagorinsky model. Regardless of filtering, the ultimate goal of the low resolution simulations

Figure 8.14: Graph of velocity at time $t = 100$ for MF simulation

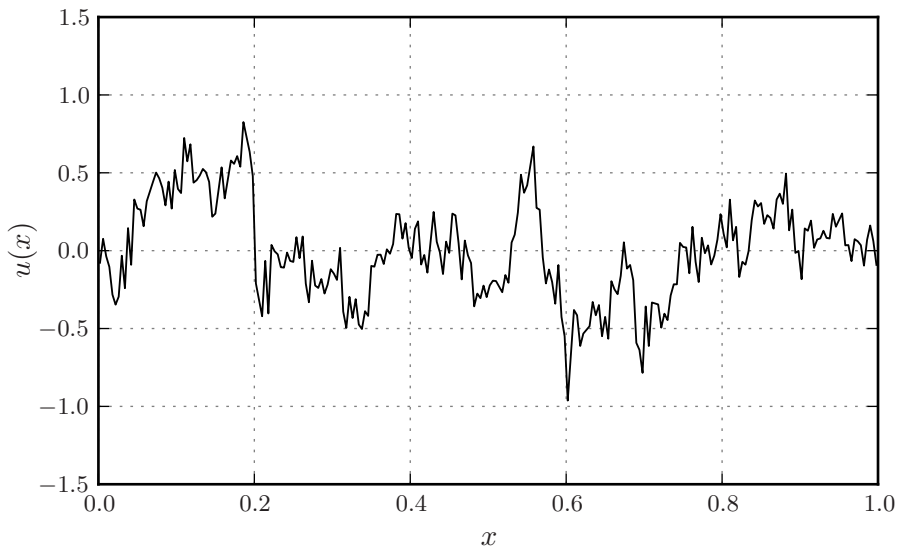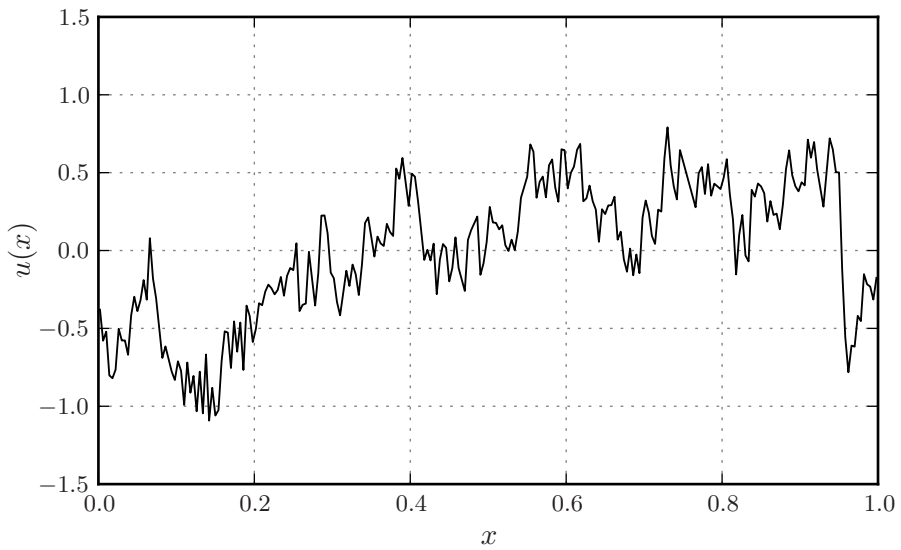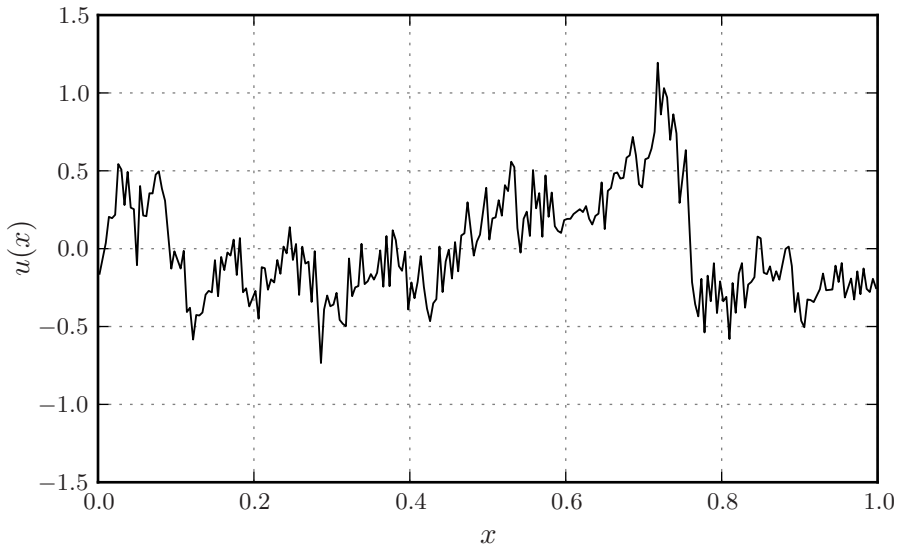Figure 8.15: Graph of velocity at time $t = 100$ for MFS simulation

Figure 8.16: Graph of velocity at time $t = 100$ for DS simulation
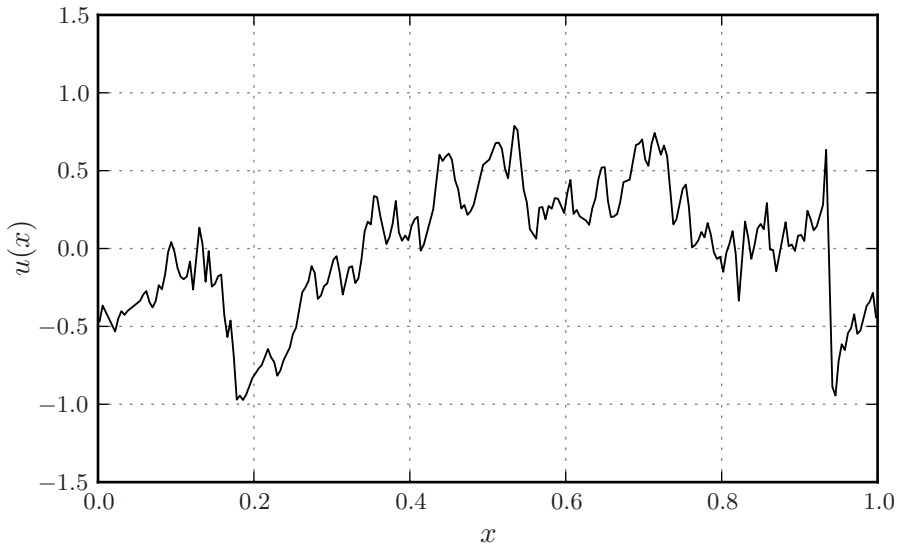

Figure 8.17: Graph of velocity at time $t = 100$ for NS simulation

is to get results that are as close as possible to the DNS results. Therefore
the unfiltered DNS results are used for all comparisons. Filtering the DNS
results would make the comparison dependent on the filter type.

The simulations presented here use different random values for the
sources, and thus only the statistical properties of the solutions can be
compared. The random number generator starts from a different seed for
each of the simulations and the number of random values required differs.
A direct comparison between simulations with comparable random sources
is presented in the next section.

Before studying the actual statistics, a general impression of the visual
soundness of the results can be obtained by analysing the velocity plots.
The velocities at time $t = 100$ are plotted in figures 8.13, 8.14, 8.15, 8.16
and 8.17 for simulations DNS, MF, MFS, DS and NS, respectively. Due
to the different random values for the sources, these plots are not meant
to be directly comparable, but only meant to show general features of the
velocity.

Figure 8.13 shows the velocity from the DNS simulation and similar
features as discussed before are observed. The velocity graph is very
irregular and shows both larger shocks and a large number of smaller shocks.
The velocity plots from the low resolution simulations presented in figures
8.14, 8.15, 8.16 and 8.17 all show comparable large scale features, but with
less small scale fluctuations. This is clearly due to the considerably lower
resolution applied for these cases.

Of the four low resolution velocity plots, the NS velocity plot is the one
that is the most different. The NS velocity plot exhibits considerably less
small scale fluctuations, and the velocity appears smoother. This means
that more of the small scale fluctuations are suppressed by the dissipation.
There are no obvious differences between the velocity plots for MF (figure
8.14), MFS (figure 8.15) and DS (figure 8.16), and so at first glance the
three subgrid models appear to behave similarly.

Once again we progress from the basic visual inspection to a more
comprehensive statistical description. Averages are computed for 950000
time samples for $t \in (50, 1000)$ for all of the simulation results. If the
low resolution simulations (MF, MFS, DS and NS) are to provide good
approximations to the high resolution DNS simulation, then the statistics
of the velocity signal should be similar. However, only the larger scales are
represented in the low resolution simulations and thus only statistics of the
larger scales are available for comparison.

Figure 8.18: Averaged energy spectra for simulations MF (solid black line), MFS (dotted line), DS (dashed line), NS (dash-dot line) and DNS (grey line)

A useful parameter in all kinds of signal analyses is the energy spectrum. A great deal of information can be extracted from the velocity signal by analysing the energy spectrum. The energy spectrum will disclose if the overall energy balance is sound, and if the energy is correctly distributed among the different scales. Energy spectra for all the simulations are presented in figure 8.18.

Clearly it can be seen that all the energy spectra follow each other well for the represented scales. For wave numbers $\kappa \in (1, 10)$ all spectra completely overlap, proving that the energy spectra of the largest scales are similar for all of the simulations. The implication of this is that the largest scales are properly represented in all cases. For wave numbers $\kappa \in (10, 100)$ the spectra do not completely overlap, but there are no major deviations, and for wave numbers $\kappa > 100$ most of the low resolution velocity graphs significantly deviate from the DNS spectrum.

To get better insight into where deviations occur between the wave numbers, a detailed view of the averaged energy spectra is plotted in figure 8.19. Here the differences become more apparent. For the range between
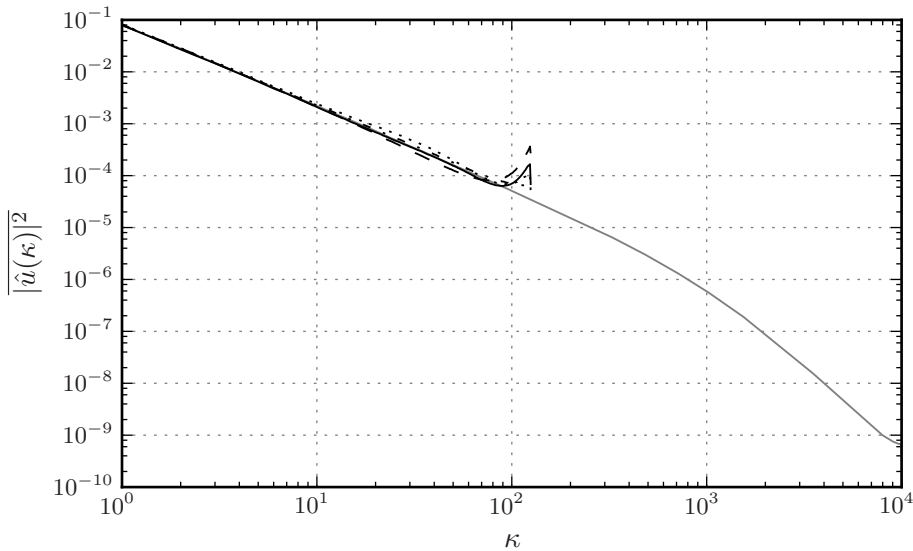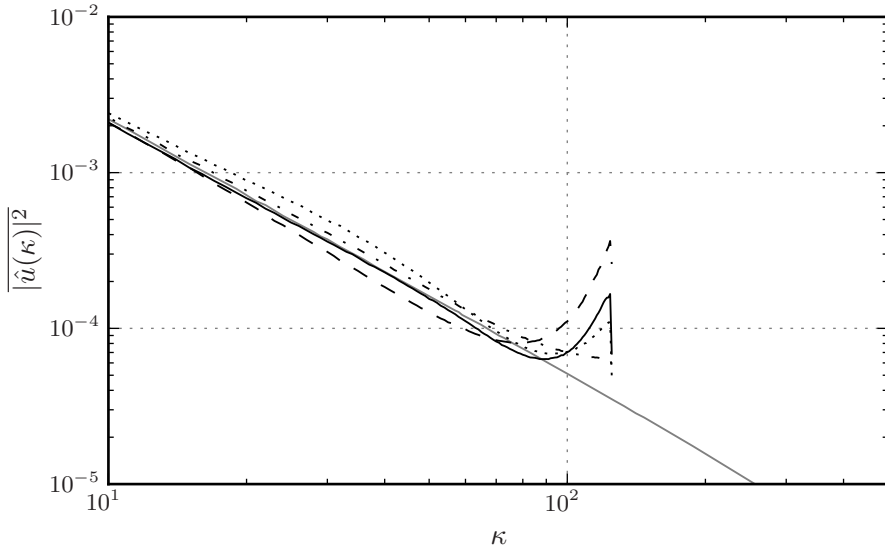
Figure 8.19: Detailed view of averaged energy spectra for simulations MF (solid black line), MFS (dotted line), DS (dashed line), NS (dash-dot line) and DNS (grey line)

wave numbers 10 and 100 the MFS and NS spectra lie slightly above the DNS spectrum, while the DS spectrum is placed slightly below. The only spectrum that is overlapping well with the DNS spectrum for most of this range is the MF spectrum, with only a slight deviation for the larger wave numbers.

For wave numbers larger than 100 the deviations are much more conspicuous and MF, MFS, DS and NS spectra all exhibit a peak at the largest wave numbers. The most prominent peak is seen for the DS spectrum, while the NS spectrum has the smallest peak. These deviations could indicate that there is excessive energy at the largest wave numbers represented in the simulations, but it is also possible that this effect is caused by aliasing in the direct Fourier transform. Aliasing is a type of distortion commonly observed when using the discrete Fourier transform with a too low sampling rate. As the velocity is very far from smooth this is not an unexpected effect.

Generally the energy spectra for MF, MFS, DS and NS all match very well with the DNS energy spectrum. It follows that the correct amount

Figure 8.20: First order structure function plotted against distance r for simulations MF (solid black line), MFS (dotted line), DS (dashed line), NS (dash-dot line) and DNS (grey line)

of energy is distributed among the different scales, and that the overall dissipation is approximately right. Out of the four the most promising energy spectra is the MF energy spectrum, showing very little deviation also in the region $\kappa \in (10, 100)$. It also interesting to observe how similar the energy spectra are. The four completely different approaches all give almost the same results. This shows that it is possible to get the required amount of dissipation with different types of subgrid models and also without a subgrid model. The large difference between the energy spectra of the simulations using subgrid models and the energy spectrum of the simulation using the same convective flux treatment but no subgrid model in figure 5.23 shows the effect of the subgrid models.

Although investigating the energy spectra is useful, it might be possible to extract additional information by analysing the structure functions. To begin with we look at the first order structure function $S_1(r)$, plotted in figure 8.20. The first order structure function also shows generally good agreement for MF, MFS, DS and NS, when compared with the DNS structure function. There are no significant inconsistencies, and the most

Figure 8.21: Second order structure function plotted against distance r for simulations MF (solid black line), MFS (dotted line), DS (dashed line), NS (dash-dot line) and DNS (grey line)

apparent difference is what appears to be a slightly different slope for the MF structure function. There are also some deviations for the lowest r values but the differences are small. The first order scaling features of the velocity does therefore appear to be in order for all of the low resolution simulations.

The second order structure function $S_2(r)$ is plotted in figure 8.21, and it is obvious that the deviations now become more significant. There is still a generally reasonable agreement with the DNS structure function for MF, MFS, DS and NS structure functions, and the slopes are not that different. As the value of r decreases the difference between the curves further develops into a clear deviation for the lowest values of r. The NS structure function lies above the DNS structure function, while all of the others are placed below.

This difference is even more pronounced for the fourth order structure function presented in figure 8.22, and the deviations really become significant. Neither of the structure functions for MF, MFS, DS or NS fit closely to the DNS structure function for $r < 0.02$, and the NS structure
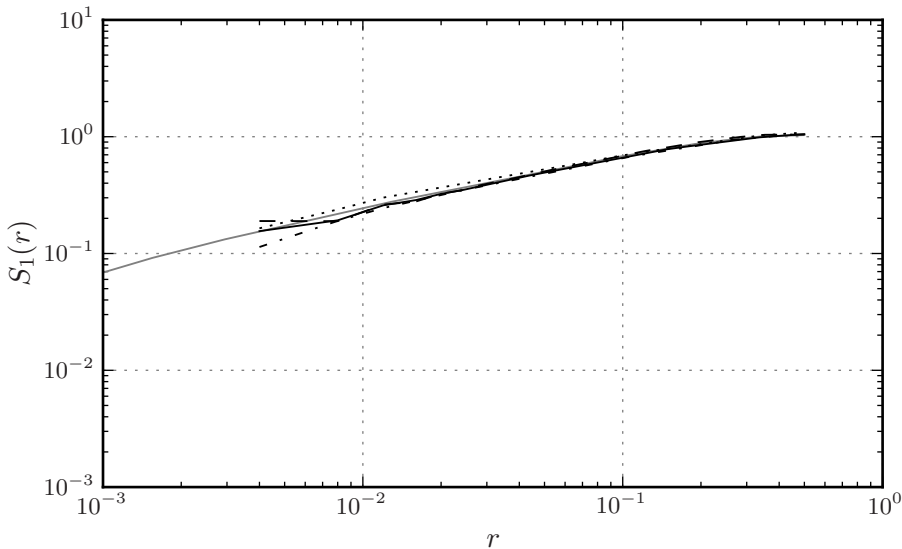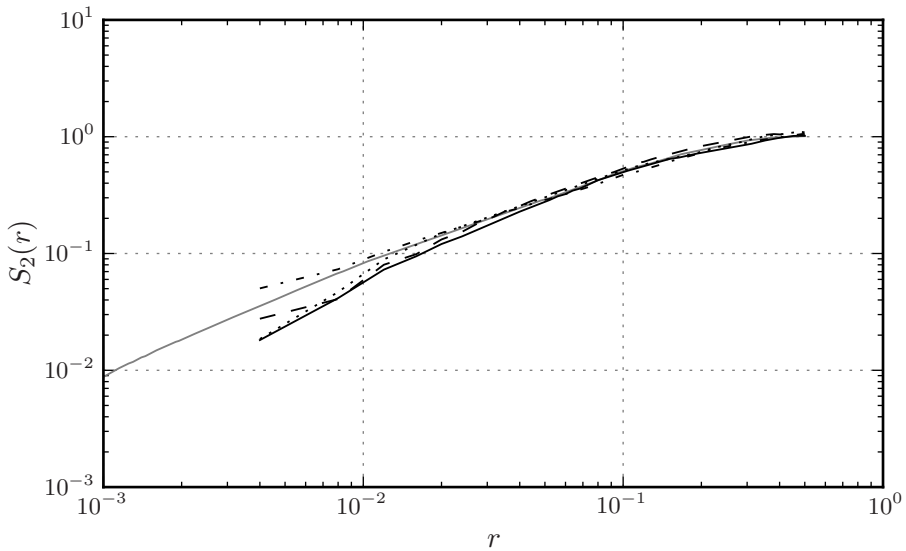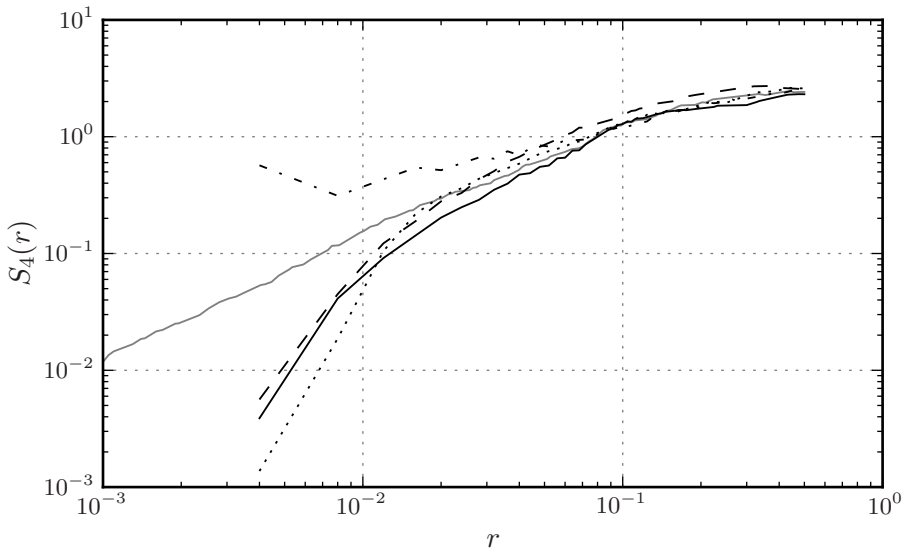
Figure 8.22: Fourth order structure function plotted against distance r for simulations MF (solid black line), MFS (dotted line), DS (dashed line), NS (dash-dot line) and DNS (grey line)

function deviates the most and for the largest scales. For $r > 0.1$ there is still quite reasonable agreement between all of the results.

The general impression from studying first, second and fourth order structure functions is that the low order statistics are well represented by all of the simulations, while higher order statistics are represented to a lesser degree. The higher order statistics of the smaller scales deviate significantly from the desired DNS structure function behaviour, and it is not immediately obvious which of MF, MFS, DS and NS has the most attractive results. The fourth order NS structure function clearly stands out with its very different behaviour compared to MF, MFS and DS, despite seemingly similar energy spectra.

It is difficult to determine how important these deviations are and if they are associated with the deviations observed in the energy spectra. It is however likely that the general representation of lower order statistics is satisfactory for all the low resolution simulations, while the higher order statistics are not that well represented. The largest scales are well taken care of by all the simulations.
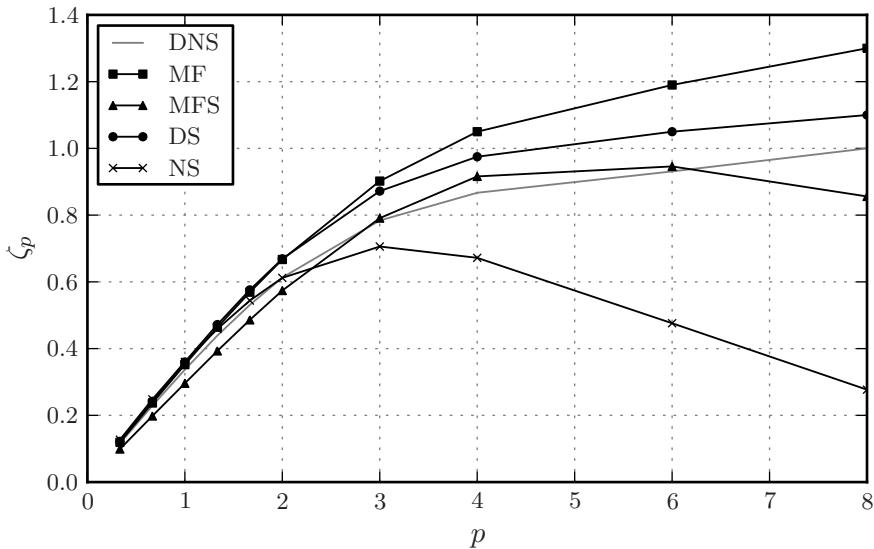
Figure 8.23: Structure function exponent scaling spectrum for simulations MF, MFS, DS and NS compared with DNS scaling spectrum

As before a least squares fit in the range $r \in (0.01, 0.1)$ is used to find the slope of the structure functions within the inertial range. These slopes are then compared for all the simulations in figure 8.23. The structure function scaling exponents ζ_p illustrate the differences observed earlier. While the deviations are quite small for the lower order structure function exponents, the deviations increase considerably for the higher order exponents.

It is obvious that the high order scaling exponents of the NS simulation behave very different from the other simulations. While it follows the DNS scaling spectrum very well for order p up to 2, the scaling properties completely change for larger order structure functions. The three other scaling spectra MF, MFS and DS look quite similar. The MFS scaling spectrum seems to fit the DNS spectrum closest for most of the structure function orders, but it is the only spectrum with appreciable deviations for order p less than 2. Both the scaling spectra for MF and DS have similar shapes to the DNS spectrum, but predict consistently too large scaling exponents for $p > 2$.

The differences seen for the higher order scaling exponents are caused by the discrepancy for small r's moving further into the range $r \in (0.01, 0.1)$.

The largest scales are still fairly well represented as shown in figure 8.22. The structure function scaling spectra of MF, MFS and DS all compare quite well with the DNS scaling spectrum. It should be noted that the deviations for the higher order structure functions are affected by much larger statistical uncertainty, due to the lack of smoothness of the high order structure function plots. Despite this, the completely different trend shown by the NS scaling spectrum is a disturbing result, and indicates that higher order statistics are not properly represented by the NS simulation results.

8.4 Direct comparison

The results presented so far have shown that the statistical properties of the low resolution simulation results correspond quite well with DNS results. However, the low resolution simulations should not only be able to predict the stationary statistical properties, but also the dynamic behaviour. The low resolution simulations should be able to predict velocities corresponding reasonably well with the DNS velocity if compared at the same instant. Simulations with directly comparable results are therefore run for all cases MF, MFS, DS, NS and DNS, and compared. All the simulations start from initial condition $u_0 = 0$, are run from $t = 0$ to $t = 10$ and have otherwise identical parameters as the earlier simulations. The MF, MFS, DS and NS simulations use 250 grid cells and the DNS use 20000 grid cells.

In order to be able to directly compare two different stochastically forced simulations, we must ensure that the large scale modes of the source term are identical for both the low resolution simulations and the DNS simulation. This is achieved by initialising the random number generator from the same seed and generating the same amount of numbers for all the simulations. The random source modes in the low resolution simulations are therefore identical to the large scale modes of the DNS, and the random modes corresponding with the smaller scales in the DNS are not used for the other simulations.

The development of the total kinetic energy $K(t)$ for $t \in (0, 1)$ is plotted in figure 8.24 and this gives a good description of the dynamical behaviour of the system. Only the first time unit is plotted as it gives a clearer understanding of what is also valid for the rest of the period $t \in (0, 10)$. As the most scales with most energy are resolved for all simulations, the total kinetic energy is expected to be similar even though much more scales are
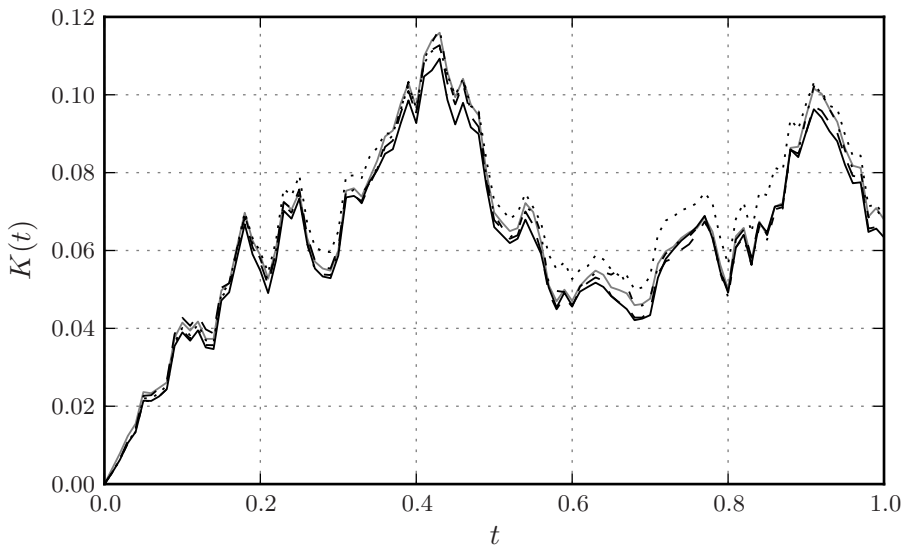
Figure 8.24: Evolution of total kinetic energy for simulations MF (solid black line), MFS (dotted line), DS (dashed line) and NS (dash-dot line) compared with DNS (grey line)

present in the DNS results.

The general impression of the kinetic energy in figure 8.24 is that all the energy graphs follow each other quite closely. This shows that all the simulations provide good representations of the temporal evolution of the total kinetic energy. This means that the global energy balance between the stochastic energy source and the dissipation is well represented by the low resolution simulations. The most significant deviations are found for the MFS energy curve, but the deviations are not that large. Based on the temporal development of kinetic energy, it does not seem to matter what the source of the dissipation is. The simulation using no subgrid model, with only numerical dissipation, does behave very similarly to the simulations using subgrid models.

The low resolution simulations should be able to provide good approximations of the actual DNS velocity field. The smaller scales are inevitably lost, but the larger scales should preferably follow the DNS large scales as closely as possible. The velocity at time $t = 10$ for $x \in (0.0, 0.2)$ is plotted for the MF simulation in figure 8.25, the MFS simulation in figure

Figure 8.25: Graph of velocity at time $t = 10$ for MF simulation (black line) compared with DNS velocity (grey line)

8.26, the DS simulation in figure 8.27 and the NS simulation in figure 8.28. In all the figures the DNS velocity is used as a reference for comparison.

For all of the low resolution simulations, the large scale features of the velocity have a general resemblance to the large scale features of the DNS velocity at time $t = 10$. Of the four simulations, the NS velocity appears to correlate best with the DNS velocity. The MFS velocity has the largest deviations, and it is the only simulation that fails to predict the large peak around $x = 0.16$.

It is uncertain how much information about the subgrid model can be extracted from velocity plots at a single time, but it is promising that after 10 characteristic length scales all the low resolution simulations predict velocities that show good agreement with the large scale features of the DNS velocity. As already mentioned, the NS velocity fits particularly well.

The observations made so far about the velocity plots might not be applicable velocity trends for all time steps. Instead of studying velocity plots for all the different time steps, simple correlation plots are used. As we want the velocity of the simulations MF, MFS, DS and NS to fit as closely to the DNS velocity as possible, the quality of the results can easily
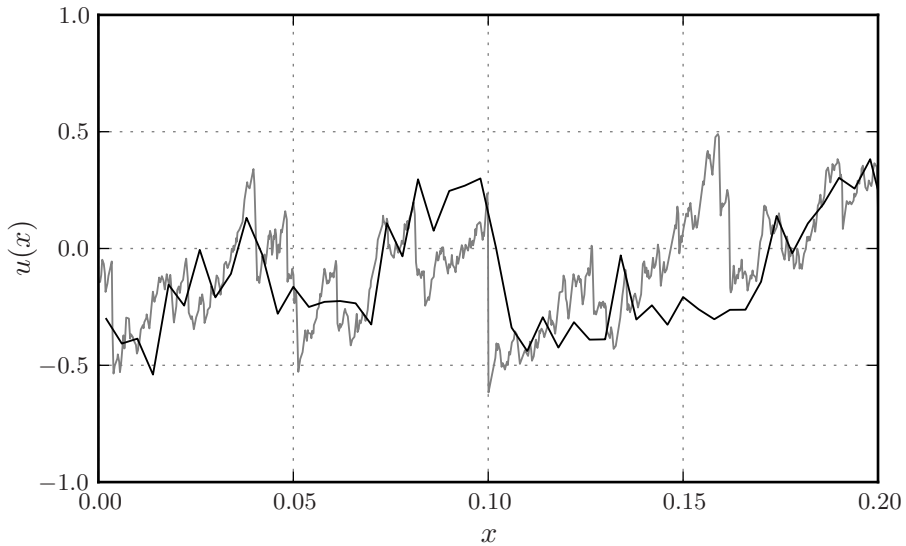
Figure 8.26: Graph of velocity at time $t = 10$ for MFS simulation (black line) compared with DNS velocity (grey line)

be evaluated with a data fit to the line $u_{\text{LES}} = u_{\text{DNS}}$.

The coordinates $(u_{\text{LES}}, u_{\text{DNS}})$ are plotted and compared with the line $u_{\text{LES}} = u_{\text{DNS}}$ in figures 8.29, 8.30, 8.31 and 8.32 for simulations MF, MFS, DS and NS, respectively. The velocity coordinates are chosen for equal values of x for the LES and DNS results by sampling the DNS velocity at the lower resolution. Ideally one would want all the points to align along the straight line, implying that the low resolution results were identical to the sampled DNS results. TThis is not the expected result and would not be the likely result even if the DNS was compared with a filtered DNS, as peaks are expected to have reduced amplitude for explicitly or implicitly filtered results.

All the four correlation plots show scatter points following a similar trend as the desired linear regression line, but how near the points are aligned with the straight line differs. As observed from the plotted velocities the best agreement is found for the NS velocity. The width of the scatter around the line is narrowest for the NS velocity, showing best correlation with the DNS velocity. The most scatter is found for the MFS velocity, and so this is the simulation where the velocity deviates the

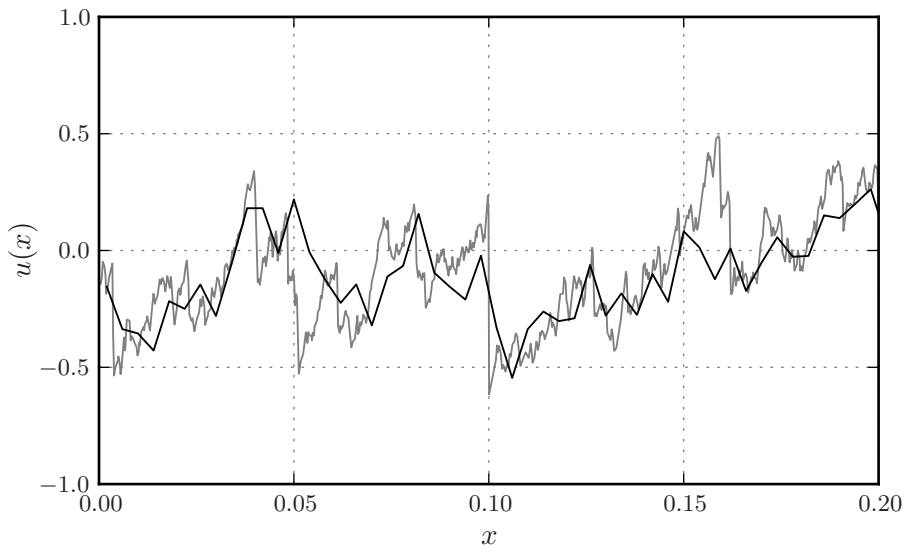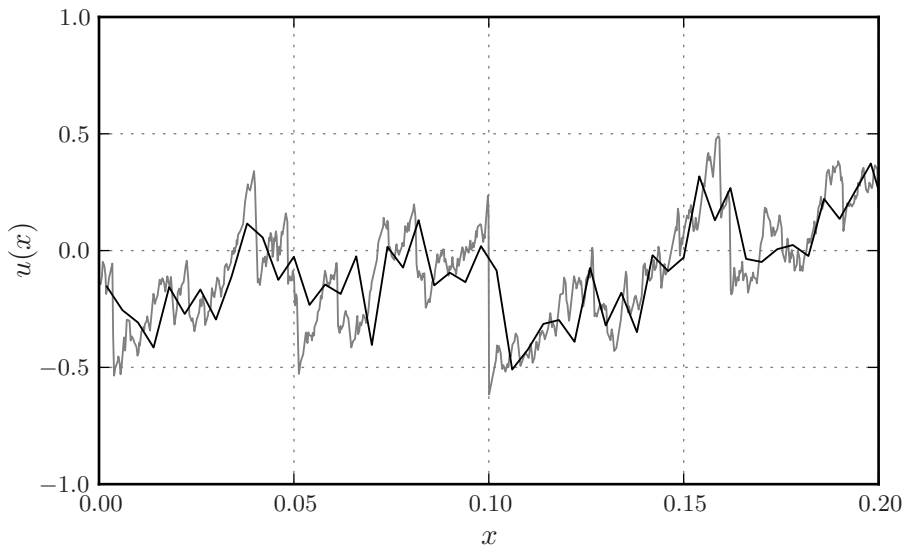Figure 8.27: Graph of velocity at time $t = 10$ for DS simulation (black line) compared with DNS velocity (grey line)
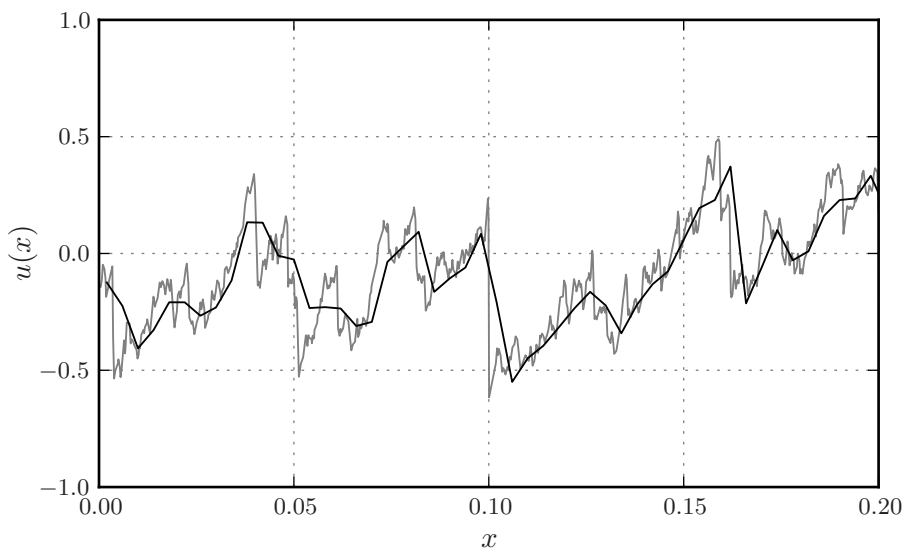
Figure 8.28: Graph of velocity at time $t = 10$ for NS simulation (black line) compared with DNS velocity (grey line)
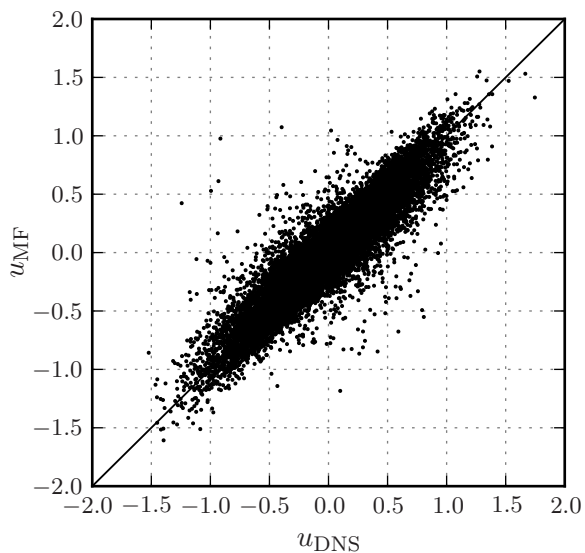
Figure 8.29:   Coordinates $(u_{\mathrm{MF}}, u_{\mathrm{DNS}})$ plotted as scatter points and compared with the straight line $u_{\mathrm{MF}} = u_{\mathrm{DNS}}$
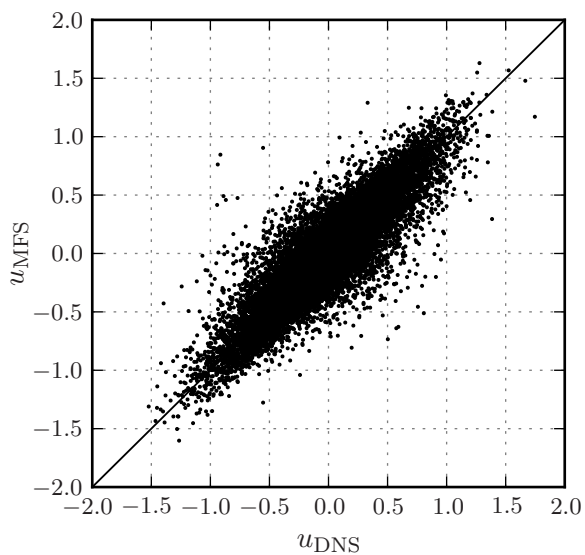
Figure 8.30:   Coordinates $(u_{\mathrm{MFS}}, u_{\mathrm{DNS}})$ plotted as scatter points and compared with the straight line $u_{\mathrm{MFS}} = u_{\mathrm{DNS}}$
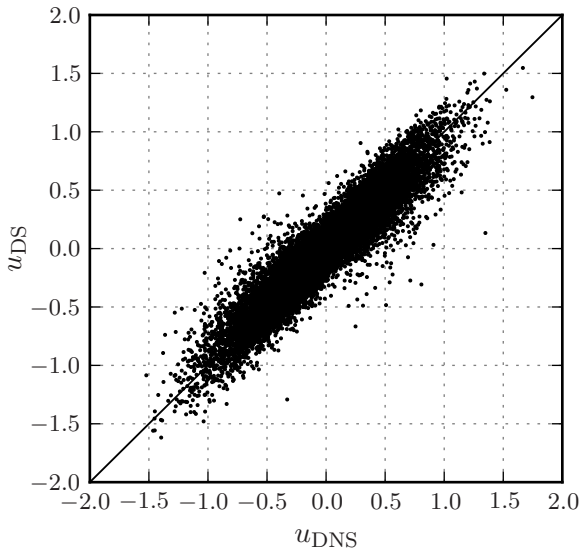
Figure 8.31: Coordinates (u_{DS}, u_{DNS}) plotted as scatter points and compared with the straight line $u_{DS} = u_{DNS}$
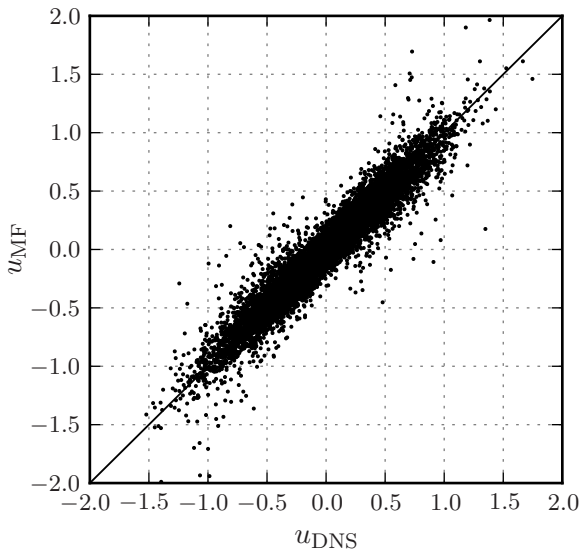
Figure 8.32: Coordinates (u_{NS}, u_{DNS}) plotted as scatter points and compared with the straight line $u_{NS} = u_{DNS}$

most. The remaining two plots, for MF and DS velocities respectively, show approximately equally good results.

8.5   Summary of results

A lot of results have been shown and some general observations should be mentioned. For the most part the results look promising. Most comparisons made, both for instantaneous and statistic parameters, show that results of all four low resolution simulations MF, MFS, DS and NS agree quite well with the DNS results.

For the correlation tests of the computed subgrid stress and subgrid dissipation, the Smagorinsky model appeared to be most promising as it was the only model where the scatter points followed the same trend as the straight line. The scatter points from the MF and MFS models could be made to fit by multiplying the model by a constant. This would however also change all the other results, most of which looked quite promising. A surprising observation was how high the correlation factors were for all three models, with values around 0.9 for both subgrid stress and dissipation. This was much higher than expected and considerably higher than typically reported for three dimensional turbulence. Using either Smagorinsky, similarity or fractal interpolation models, no correlation coefficient larger than 0.5 for the subgrid stress was found by Basu *et al.* (2004*a*). It seems like the tested subgrid models yield a much higher correlation in one dimensional turbulence.

For the simulation results the agreement with DNS was in general good. All four low resolution simulations gave results in reasonable to good agreement with the DNS results. The NS simulation using no subgrid model performed better than the three simulations using models for the direct comparisons. The statistical properties of higher order structure functions in particular were however not properly represented by this simulation, mostly due to the less than satisfactory prediction of the smaller scales. Considering that numerical dissipation is essentially an eddy-viscosity model in one dimension, one might argue that the NS simulation also has a subgrid model. How well this would translate to three dimensions is not easy to predict, but it is important to note that in three dimensions the numerical dissipation would no longer be exactly analogous to an eddy-viscosity model.

As the primary purpose of this report is to study fractal subgrid models,

the performance of the two fractal models MF and MFS are of particular interest. Both models provide sufficient dissipation to work as subgrid models, and the results are generally quite good. For most of the studied results, both models behave quite similarly to the DS model, but they are not appreciably better for any of the results. The results indicate that both MF and MFS models are viable alternatives as subgrid models, but that neither outperform the commonly used DS model.

Compared with published results, general agreement for the evolution of the kinetic energy and instantaneous velocity is similar to what was observed by Basu (2009) for dynamic eddy-viscosity models. The agreement of the energy spectra and the second order structure function is also similar. Basu (2009) concluded that eddy-viscosity subgrid models produced satisfactory results, and this would be suitable to also conclude for the results presented herein.

The idea of using the fractal interpolation technique as a subgrid model was introduced by Scotti & Meneveau (1999), and the two fractal models MF and MFS presented here produce energy spectra in equally good agreement with the DNS spectrum as the best fractal model of Scotti & Meneveau (1999). Scotti & Meneveau (1999) did however, not get satisfactory results with an eddy-viscosity model with constant eddy-viscosity.

Chapter 9

Conclusion

In this thesis subgrid models have been tested for low resolution simulations of the stochastically forced Burgers equation. Two new subgrid models based on the fractal interpolation technique have been developed and thoroughly tested. The results have been compared with high resolution simulations, and results from low resolution simulations using the well-known dynamic Smagorinsky model. In order to also evaluate the necessity of having a subgrid model, a low resolution simulation with a numerically dissipative convective scheme and no subgrid model was compared with the other simulations.

Correlation studies of the subgrid stress tensor computed from filtered high resolution results revealed that the dynamic Smagorinsky model and the two fractal models all had remarkably high correlation coefficients with the exact subgrid stress. Correlation coefficients with values around 0.9 was found for all three models, and for both the subgrid stress and the subgrid dissipation. This is a much higher correlation coefficient than what is typically found for any subgrid models in published three-dimensional studies. However, it was seen from the correlation plots that the dynamic Smagorinsky model predicted the subgrid stress values closest to the exact values. While no backscatter was predicted by the dynamic Smagorinsky model, both of the fractal models predicted regions of negative subgrid dissipation.

To test the performance of the subgrid models in actual simulations, new low resolution simulations were compared with high resolution simulation results. It was found that all the low and high resolution simulations corresponded reasonably well. Both of the new fractal subgrid models

were tested, as well as the dynamic Smagorinsky model and one simulation
without a subgrid model. The energy spectra and the low order structure
functions of of the low and high resolution results were in good agreement.
Larger deviations were found for the higher order structure functions.
The low resolution simulation with no subgrid model showed particularly
poor results for the higher order structure functions, due to problematic
behaviour at the smallest scales.

By using the same exact random large scale modes for the sources in
the different simulations, instantaneous results could be compared for the
different simulations. All the low resolution simulations predicted a correct
development of the kinetic energy, following the high resolution simulation
closely. When comparing the actual velocity values, it was found that the
simulation with no subgrid model compared best with the high resolution
results.

The purpose of this study has been to evaluate fractal based subgrid
models for the stochastically forced Burgers equation. The results have
showed that the fractal interpolation technique is a viable basis for a subgrid
model. The two-stage interpolation method makes it possible to adjust the
amount of dissipation to what is required by the numerical methods used.
However, none of the results show in any way that the fractal models have
significantly superior performance to the Smagorinsky model.

Perhaps equally interesting as the results for the fractal subgrid
models, are the results for the simulation using no subgrid model.
Despite questionable performance for high order structure functions, the
simulation using no subgrid model outperformed all the other low resolution
simulations in the direct velocity comparison. By choosing a numerical
method with the appropriate amount of numerical dissipation, good results
can be obtained also without a subgrid model. However, considering
that numerical dissipation is a sort of eddy viscosity model, the only
real difference is that the subgrid model is now included in the numerical
method.

It appears like the single most important factor is to get the appropriate
amount of dissipation, and that this can be achieved in several different
ways. The total amount of dissipation in both the numerical methods and
the subgrid model is what actually matters in the simulation. It follows
that the choice of subgrid model must be closely considered together with
the type of numerical method used. As shown earlier in the report, many
of the most commonly used discretisation methods already have too much

numerical dissipation before the subgrid model is added. This is one of the reasons why the finite volume method was used for the simulations presented here. As a reflection, it might be regarded as unfortunate that subgrid models are often tested with high-order spectral methods.

Even though the stochastically forced Burgers equation is intended used as a model equation for turbulence, it is not appropriate to draw conclusions about three-dimensional turbulence based on one-dimensional results. Even though the low order statistics of the stochastically forced Burgers equation are very similar to those of homogeneous Kolmogorov turbulence, the high order statistics are completely dominated by the shocks. When solving the large eddy simulation equations, the solution is expected to be smooth. This is completely different from the Burgers equation, which will always produce shocks if the viscosity is sufficiently low.

One general concept that should also be applicable to three-dimensional simulations is that both the subgrid model and the numerical methods provide dissipation. Choosing a subgrid model is therefore just as much a matter of finding a model that fits the numerical schemes, as it is a matter of finding a model that properly represents the smallest scales of turbulence. Considering that good results were obtained without using a subgrid model for the stochastically forced Burgers equation, it could be argued that one dimension is not sufficient to represent the complexity of three-dimensional subgrid modelling.

There are several interesting paths one might follow to advance some of the topics addressed here. Although the fractal subgrid models tested here did not have superior performance to the dynamic Smagorinsky model, using fractals to model turbulence is still an intriguing topic. There are many different ways one might use fractal geometry to model turbulence, and the multifractal features of the actual subgrid stress might be exploited to create a direct multifractal model for the subgrid stress, instead of using fractal interpolation for the velocity. The fractal features of dissipation, vorticity and helicity could also be used to create subgrid closures. In the end the merit of all types of subgrid models must be evaluated in actual three-dimensional simulations.

The evaluation of the actual necessity of using subgrid models in three-dimensional simulations is also a topic that deserves further attention. Although the results presented here indicate that subgrid modelling is not strictly necessary in one dimension, this notion can not be immediately extrapolated to three dimensions. It should be possible to choose numerical

schemes with the right appropriate of numerical dissipation, but it is unlikely that this is enough to accurately reproduce the three-dimensional subgrid stress tensor. Nevertheless, this is an interesting topic that needs further investigation.

Bibliography

ANDERSSON, H. I. 1988 Introduction to Turbulence Modelling. Lecture notes in subject 76572 Turbulent Flow, Norwegian Institute of Technology.

ANSELMET, F., GAGNE, Y., HOPFINGER, E. J. & ANTONIA, R. A. 1984 High-order velocity structure functions in turbulent shear flows. *Journal of Fluid Mechanics* **140**, 63–89.

ARAKAWA, A. 1966 Computational design for long-term numerical integration of the equations of fluid motion: Two-dimensional incompressible flow. part i. *Journal of Computational Physics* **1**, 119 – 143.

BARDINA, J., FERZIGER, J. H. & REYNOLDS, W. C. 1980 Improved subgrid-scale models for large-eddy simulation. *American Institute of Aeronautics and Astronautics Paper* **80**, 80–1357.

BARNSLEY, M. F. 1986 Fractal functions and interpolation. *Constructive Approximation* **2**, 303–329.

BARNSLEY, M. F. & RISING, H. 1993 *Fractals everywhere*, 2nd edn. Academic Press.

BASU, S. 2009 Can the dynamic eddy-viscosity class of subgrid-scale models capture inertial-range properties of burgers turbulence? *Journal of Turbulence* **10**, 1–16.

BASU, S., FOUFOULA-GEORGIOU, E. & PORTÉ-AGEL, F. 2004a Synthetic turbulence, fractal interpolation, and large-eddy simulation. *Physical Review E* **70**, 026310–1–026310–11.

BASU, S., FOUFOULA-GEORGIOU, E. & PORTÉ-AGEL, F. 2004*b* Synthetic turbulence, fractal interpolation, and large-eddy simulation. *Physical Review E* **70**, 026310–1–026310–11.

BEC, J., FRISCH, U. & KHANIN, K. 2000 Kicked Burgers turbulence. *Journal of Fluid Mechanics* **416**, 239–267.

BERGLAND, G. D. 1969 A guided tour of the fast fourier transform. *Spectrum, IEEE* **6**, 41–52.

BOUSSINESQ, J. 1877 Essai sûr la théorie des eaux courantes. *Mémoires a l'Académie des Sciences de l'Institut National de France* **23**, 24–46.

BURGERS, J. M. 1948 A mathematical model illustrating the theory of turbulence. *Advances in Applied Mechanics* **1**, 171–199.

BURGERS, J. M. 1974 *The nonlinear diffusion equation: asymptotic solutions and statistical problems*. Reidel Dordrecht.

CHEKHLOV, A. & YAKHOT, V. 1995*a* Kolmogorov turbulence in a random-force-driven Burgers equation. *Physical Review E* **51**, R2739–R2742.

CHEKHLOV, A. & YAKHOT, V. 1995*b* Kolmogorov turbulence in a random-force-driven Burgers equation: Anomalous scaling and probability density functions. *Physical Review E* **52**, 5681–5684.

COCKBURN, B., SHU, C.-W., JOHNSON, C., TADMOR, E. & SHU, C.-W. 1998 Essentially non-oscillatory and weighted essentially non-oscillatory schemes for hyperbolic conservation laws. In *Advanced Numerical Approximation of Nonlinear Hyperbolic Equations*, *Lecture Notes in Mathematics*, vol. 1697, pp. 325–432. Springer Berlin / Heidelberg.

COLE, J. D. 1951 On a quasi-linear parabolic equation occurring in aerodynamics. *Quarterly of Applied Mathematics* **9**, 225–236.

COOLEY, J. W. & TUKEY, J. W. 1965 An algorithm for the machine calculation of complex Fourier series. *Mathematics of Computation* **19**, 297–301.

DAVIS, A., MARSHAK, A., WISCOMBE, W. & CAHALAN, R. 1994 Multifractal characterizations of nonstationarity and intermittency in geophysical fields: Observed, retrieved, or simulated. *Journal of Geophysical Research* **99** (D4), 8055–8072.

DURBIN, P. A. & PETTERSON REIF, B. A. 2011 *Statistical theory and modeling for turbulent flows*. John Wiley & Sons, Ltd.

ERTESVÅG, I. S. 2000 *Turbulent strøyming og forbrenning: frå turbulensteori til ingeniør-verkty*. Tapir akademiske forlag, Trondheim.

FALCONER, K. 2003 *Fractal Geometry: Mathematical Foundations and Applications*, 2nd edn. John Wiley & Sons Ltd.

FRIGO, M. & JOHNSON, S. G. 2005 The design and implementation of FFTW3. *Proceedings of the IEEE* **93**, 216–231.

FRISCH, U. 1995 *Turbulence: The Legacy of A. N. Kolmogorov*. Cambridge University Press.

FRISCH, U. & BEC, J. 2001 "Burgulence". *New trends in turbulence, Turbulence: nouveaux aspects* pp. 341–383.

GERMANO, M. 1992 Turbulence: the filtering approach. *Journal of Fluid Mechanics* **238**, 325–336.

GERMANO, M., PIOMELLI, U., MOIN, P. & CABOT, W. 1991 A dynamic subgrid-scale eddy viscosity model. *Physics of Fluids A: Fluid Dynamics* **3**, 1760–1765.

GEURTS, B. J. 2004 *Elements of direct and large-eddy simulation*. R.T. Edwards, Inc.

GOTOH, T. & KRAICHNAN, R. H. 1998 Steady-state Burgers turbulence with large-scale forcing. *Physics of Fluids* **10**, 2859–2866.

GOTTLIEB, S. & SHU, C. W. 1998 Total variation diminishing Runge-Kutta schemes. *Mathematics of Computation* **67**, 73–85.

GURBATOV, S. N., MALAKHOV, A. N. & SAICHEV, A. I. 1991 *Nonlinear random waves and turbulence in nondispersive media: waves, rays, particles*. Manchester University Press.

GURBATOV, S. N., SIMDYANKIN, S. I., AURELL, E., FRISCH, U. & TOTH, G. 1997 On the decay of Burgers turbulence. *Journal of Fluid Mechanics* **344**, 339–374.

HARTEN, A., ENGQUIST, B., OSHER, S. & CHAKRAVARTHY, S. R. 1987
Uniformly high order accurate essentially non-oscillatory schemes, iii.
Journal of Computational Physics **71**, 231–303.

HAYOT, F. & JAYAPRAKASH, C. 1996 Multifractality in the stochastic
burgers equation. *Physical Review E* **54**, 4681–4684.

HAYOT, F. & JAYAPRAKASH, C. 1997*a* From scaling to multiscaling in the
stochastic burgers equation. *Physical Review E* **56**, 4259–4262.

HAYOT, F. & JAYAPRAKASH, C. 1997*b* Structure functions in the
stochastic burgers equation. *Physical Review E* **56**, 227–230.

HINZE, J. O. 1975 *Turbulence*, 2nd edn. McGraw-Hill.

HOPF, E. 1950 The partial differential equation $u_t + uu_x = \mu u_{xx}$.
Communications on Pure and Applied Mathematics **3**, 201–230.

JAFFARD, S. 1997*a* Multifractal formalism for functions part i: Results
valid for all functions. *SIAM Journal on Mathematical Analysis* **28**, 944–
970.

JAFFARD, S. 1997*b* Multifractal formalism for functions part ii: Self-similar
functions. *SIAM Journal on Mathematical Analysis* **28**, 971–998.

KEYNES, J. M. 1920 *A Treatise on Probability*. Macmillan & Co., Ltd.,
London. Unabridged republication (2007) by Watchmaker Publishing.

KOLMOGOROV, A. N. 1941*a* Dissipation of energy in locally isotropic
turbulence. *Dokl. Akad. Nauk SSSR* **30**, 16–18.

KOLMOGOROV, A. N. 1941*b* The local structure of turbulence in
incompressible viscous fluid for very large Reynolds number. *Dokl. Akad.
Nauk SSSR* **30**, 299–303.

KOLMOGOROV, A. N. 1941*c* On degeneration (decay) of isotropic
turbulence in an incompressible viscous liquid. *Dokl. Akad. Nauk SSSR*
31, 538–540.

KOLMOGOROV, A. N. 1941*d* On the logarithmically normal law of
distribution of the size of particles under pulverization. *Dokl. Akad. Nauk
SSSR* **31**, 99–101.

Kolmogorov, A. N. 1942 Equations of turbulent motion of an incompressible fluid. *Izvestia Akademia Nauk SSSR, Seria Fizicheska VI* **6**, 56–58.

Kwak, D. 1975 *Three-dimensional time dependent computation of turbulent flow*. PhD Thesis, Stanford University.

Launder, B. E. & Spalding, D. B. 1974 The numerical computation of turbulent flows. *Computer Methods in Applied Mechanics and Engineering* **3**, 269–289.

van Leer, B. 1974 Towards the ultimate conservative difference scheme. II. Monotonicity and conservation combined in a second-order scheme. *Journal of Computational Physics* **14**, 361–370.

Leonard, A. 1974 Energy cascade in large-eddy simulations of turbulent fluid flows. *Advances in Geophysics* **18**, 237–248.

Lilly, D. K. 1967 The representation of small scale turbulence in numerical simulation experiments. In *IBM Scientific Computing Symposium on environmental sciences*, pp. 195–210. Yorktown heights.

Lilly, D. K. 1992 A proposed modification of the Germano subgrid-scale closure method. *Physics of Fluids A: Fluid Dynamics* **4**, 633–635.

Liu, S., Meneveau, C. & Katz, J. 1994*a* On the properties of similarity subgrid-scale models as deduced from measurements in a turbulent jet. *Journal of Fluid Mechanics* **275**, 83–119.

Liu, X. D., Osher, S. & Chan, T. 1994*b* Weighted essentially non-oscillatory schemes. *Journal of Computational Physics* **115**, 200–212.

Love, M. D. 1980 Subgrid modelling studies with burgers' equation. *Journal of Fluid Mechanics* **100**, 87–110.

Lumley, J. L. 1970 *Stochastic Tools in Turbulence*. Academic Press Inc., New York. Unabridged republication (2007) by Dover Publications, Inc.

Mandelbrot, B. B. 1974 Intermittent turbulence in self-similar cascades: divergence of high moments and dimension of the carrier. *Journal of Fluid Mechanics* **62**, 331–358.

MANDELBROT, B. B. 1975 On the geometry of homogeneous turbulence, with stress on the fractal dimension of the iso-surfaces of scalars. *Journal of Fluid Mechanics* **72**, 401–416.

MANDELBROT, B. B. 1982 *The Fractal Geometry of Nature*. W. H. Freeman and Company, New York.

MANDELBROT, B. B. & HUDSON, R. L. 2006 *The (Mis)behavior of Markets: A Fractal View of Financial Turbulence*. Basic Books.

MCLACHLAN, R. I. 2003 Spatial discretization of partial differential equations with integrals. *IMA Journal of Numerical Analysis* **23**, 645–664.

MENEVEAU, C. & KATZ, J. 2000 Scale-invariance and turbulence models for large-eddy simulation. *Annual Review of Fluid Mechanics* **32**, 1–32.

MENEVEAU, C. & SREENIVASAN, K. 1987 The multifractal spectrum of the dissipation field in turbulent flows. *Nuclear Physics B - Proceedings Supplements* **2**, 49–76.

MONIN, A. S. & YAGLOM, A. M. 1971 *Statistical Fluid Mechanics: Mechanics of Turbulence: Volume I*. MIT Press, Cambridge. Unabridged republication (2007) by Dover Publications, Inc., Translation by J. L. Lumley (editor).

MONIN, A. S. & YAGLOM, A. M. 1975 *Statistical Fluid Mechanics: Mechanics of Turbulence: Volume II*. MIT Press, Cambridge. Unabridged republication (2007) by Dover Publications, Inc., Translation by J. L. Lumley (editor).

MÜLLER, B. 2010 Introduction to Computational Fluid Dynamics: Lecture notes for the course Computational Heat and Fluid Flow. Department of Energy and Process Engineering, Norwegian University of Science and Technology.

NILSEN, C. 2010 Statistical Description of Turbulent Flow. *Tech. Rep.*. Department of Energy and Process Engineering, NTNU.

NILSEN, C. & ANDERSSON, H. I. 2011 A computational study of burgers turbulence. In *MekIT'11 Sixth National Conference on Computational Mechanics* (ed. H. I. Andersson & B. Skallerud), pp. 257–268.

PRANDTL, L. 1945 Über ein neues Formelsystem für die ausgebildete Turbulenz. *Nachrichten Akademisches Wissenschaft, Göttingen, Mathematik-Physik Klasse* pp. 6–19.

RICHARDSON, L. F. 1922 *Weather Prediction by Numerical Process*. Cambridge University Press, Cambridge.

SCHLICHTING, H. 1979 *Boundary Layer Theory: Seventh Edition*. McGraw-Hill.

SCHLICHTING, H. & GERSTEN, K. 2000 *Boundary Layer Theory: 8th Revised and Enlarged Edition*. Springer Verlag.

SCHROEDER, M. 1991 Fractals, Chaos, Power Laws: Minutes from an Infinite Paradise. Unabridged republication (2009) by Dover Publications, Inc.

SCOTTI, A. & MENEVEAU, C. 1997 Fractal model for coarse-grained nonlinear partial differential equations. *Physical Review Letters* **78**, 867–870.

SCOTTI, A. & MENEVEAU, C. 1999 A fractal model for large eddy simulation of turbulent flow. *Physica D: Nonlinear Phenomena* **127**, 198–232.

SCOTTI, A., MENEVEAU, C. & SADDOUGHI, S. G. 1995 Fractal dimension of velocity signals in high-reynolds-number hydrodynamic turbulence. *Physical Review E* **51**, 5594–5608.

SHE, Z.-S., AURELL, E. & FRISCH, U. 1992 The inviscid Burgers equation with initial data of Brownian type. *Communications in Mathematical Physics* **148**, 623–641.

SINAI, Y. 1992 Statistics of shocks in solutions of inviscid Burgers equation. *Communications in Mathematical Physics* **148**, 601–621.

SMAGORINSKY, J. 1963 General circulation experiments with the primitive equations. *Monthly Weather Review* **91**, 99–164.

SREENIVASAN, K. R. 1991 Fractals and multifractals in fluid turbulence. *Annual Review of Fluid Mechanics* **23**, 539–600.

TENNEKES, H. & LUMLEY, J. L. 1972 *A First Course in Turbulence*. The MIT press.

TURNER, C. V. & ROSALES, R. R. 1997 The small dispersion limit for a nonlinear semidiscrete system of equations. *Studies in Applied Mathematics* **99** (3), 205–254.

VASSILICOS, J. C. 1989 On the geometry of lines in two-dimensional turbulence. In *Advances in Turbulence 2*.

VERGASSOLA, M., DUBRULLE, B., FRISCH, U. & NOULLEZ, A. 1994 Burgers' equation, Devil's staircases and the mass distribution for large-scale structures. *Astronomy and Astrophysics* **289**, 325–356.

VERSTEEG, H. K. & MALALASEKERA, W. 2007 *An introduction to computational fluid dynamics: the finite volume method*. Prentice Hall.

WINCKELMANS, G. S., LUND, T. S., CARATI, D. & WRAY, A. A. 1996 A priori testing of subgrid-scale models for the velocity-pressure and vorticity-velocity formulations. In *Center for Turbulence Research, Proceedings of the summer program*, pp. 309–329.

YAKHOT, V. & CHEKHLOV, A. 1996 Algebraic Tails of Probability Density Functions in the Random-Force-Driven Burgers Turbulence. *Physical Review Letters* **77**, 3118–3121.

YEE, H. C. & SJÖGREEN, B. 2004 Designing adaptive low-dissipative high order schemes for long-time integrations. In *Turbulent Flow Computation* (ed. R. Moreau, D. Drikakis & B. J. Geurts), *Fluid Mechanics and Its Applications*, vol. 66, pp. 141–198. Springer Netherlands.

Appendix A

Statistical treatment of turbulence

The chapter gives an introduction to the notion of treating turbulence as a statistical problem. First the problem of turbulence is presented, and then it is argued why one might consider this a statistical problem. Common tools of probability theory are then presented, and averaging is discussed. Lastly the chapter deals with scales and self-similarity in turbulence, serving as a bridge to the next topic of fractal geometry.

Classical books on turbulence, that cover the statistical approach, are Hinze (1975), Monin & Yaglom (1971), Monin & Yaglom (1975), Tennekes & Lumley (1972) and Lumley (1970). A more modern account of turbulence, and statistical tools in particular, is given by Frisch (1995).

A.1   The turbulence problem

In nature and in engineering applications, flows are usually turbulent. Turbulent flows are characterised by severely disorganised, irregular and unsteady motion, three-dimensionality, rapidly varying vorticity, high diffusion and viscous dissipation.

Even though this chapter has been based on statistical methods, the problem of turbulence is a deterministic one. The incompressible Navier-Stokes equations in Cartesian tensor form is written in equation (A.1). The incompressible continuity equation in Cartesian tensor form is written in

equation (A.2).

$$\rho \frac{Du_i}{Dt} = f_i - \frac{\partial p}{\partial x_i} + \mu \frac{\partial^2 u_i}{\partial x_j \partial x_j} \tag{A.1}$$

$$\frac{\partial u_i}{\partial x_i} = 0 \tag{A.2}$$

The Navier-Stokes equations can be solved, when coupled with the continuity equation and sufficient boundary conditions. A thorough explanation of the Navier-Stokes equations, and other fundamental differential equations of fluid mechanics is given in Schlichting (1979) or Schlichting & Gersten (2000).

For incompressible flow the incompressible Navier-Stokes equations are commonly thought to contain all of turbulence, and thus solving these equations would give the solution to the problem of turbulence in an incompressible fluid. However, there is no known analytical solution to the Navier-Stokes equations, and solving them through Direct Numerical Simulation is extremely costly and time consuming. The difficulty of turbulence is connected to some of the properties of these equations, which include:

- The existence of a smooth solution at all times.

- Interdependency for the entire domain.

- Non-linearity, due to the non-linear advection terms.

- A large range of scales, giving a system that is stiff at all times.

A.2 A probabilistic approach

Keynes (1920) defined probability as the degree of rational belief we can hold a claim to. Even though turbulence is not a problem of randomness, a probabilistic approach might lead to results that one can hold rational belief in. The statistical approach attempts to simplify the problem described in chapter A.1 by looking for order and universality in the erratic behaviour of turbulence.

For a laminar flow problem, solving the set of equations yields the unique solution that describes the flow properties. In turbulence, however, the problem is finding the ensemble of all solutions satisfying the equation and boundary conditions. Thus, even though the problem is deterministic, the

solution can be probabilistic. Essentially, when one is looking for general results, the study is no longer just concerned with that particular flow, but with the statistical ensemble of all similar flows.

Usually the field of statistics is concerned with studying the output from a process, where the generator of the data is unknown and the problem consists of understanding how the generator works. However, in the field of statistical fluid mechanics, the generator is known, and the problem consists of predicting the output.

In order to better understand turbulence, one can use results from experiments or high accuracy simulations such as DNS, and then try to find general results. In order to do so, various statistical tools are needed.

A.3 Probability theory

For a stochastic variable u, the probability of finding u between u and $u + du$ is the probability density function $B(u)$, and it is defined such that

$$\int_{-\infty}^{\infty} B(u)\, du = 1. \tag{A.3}$$

A.3.1 Averaging and ergodicity

Finding averages is a central part of a statistical description of turbulence. A discussion on averaging was written by Monin & Yaglom (1971, pages 205–218) and different types of averages were listed by Hinze (1975, page 5). For a stochastic variable u, two commonly used averages can be defined.

Definition A.1. *The ensemble average of u is defined as*

$$\langle u \rangle \equiv \int_{-\infty}^{\infty} uB(u)\, du\,, \tag{A.4}$$

where $B(u)$ is the probability density function of u.

Definition A.2. *The time average of a time dependent u is defined as*

$$\overline{u} \equiv \lim_{T \to \infty} \frac{1}{T} \int_{0}^{T} u(t)\, dt\,, \tag{A.5}$$

where T is the averaging period.

In statistics an average value is usually found by evaluating all realisations of the total solution space. In most cases, and also here, this is not possible. So to find usable averages, we invoke ergodicity and use the time average of the value as an approximation to the ensemble average over all realisations. Ergodic theory is a large branch of mathematics that will not be covered in any detail here, but Birkhoff's ergodic theorem (Frisch, 1995, pp. 36–37) ensures that the ensemble average can be approximated by the time average. Ergodicity is also discussed in Monin & Yaglom (1971, pp. 214–218 and 249–256).

Theorem A.3. *The ergodic theorem states that under suitable conditions, the time average of u is equal to the ensemble average of u,*

$$\bar{u} = \langle u \rangle. \tag{A.6}$$

The ergodic theorem can be thought of as an extension of the strict law of large numbers. For practical purposes one conveniently assumes that the time average can be approximated by an average over a finite number of time instances

$$\bar{u} = \frac{1}{T} \int_0^T u(t)\, dt = \frac{1}{T} \sum_{n=1}^N u_n\, \Delta t = \frac{1}{N} \sum_{n=1}^N u_n, \tag{A.7}$$

for suitably large T and N, and constant Δt.

A.3.2 Statistical moments

For a stochastic variable u, the moments can be defined and they provide information on how u is distributed in the probability space. The moments of a random variable, in the context of turbulence, are discussed in detail in Monin & Yaglom (1971, pp. 222–256) and Lumley (1970, pp. 19–41).

Definition A.4. *The nth order moment of u is defined as*

$$\langle u^n \rangle \equiv \int_{-\infty}^{\infty} u^n B(u)\, du\,. \tag{A.8}$$

The 1st order moment is then the ensemble average of u. A random variable is centred if the 1st order moment is equal to zero. By subtracting the 1st order moment from u, one gets the central moments. The first four central moments are most commonly used.

Definition A.5. *The 2nd order central moment of u is the variance of u*

$$\sigma^2 \equiv \langle (u - \langle u \rangle)^2 \rangle, \tag{A.9}$$

and can be approximated by

$$\sigma^2 = \overline{(u - \overline{u})^2}. \tag{A.10}$$

Definition A.6. *The 3rd order central moment of u is the skewness of u*

$$S \equiv \langle (u - \langle u \rangle)^3 \rangle, \tag{A.11}$$

and can be approximated by

$$S = \overline{(u - \overline{u})^3}. \tag{A.12}$$

Definition A.7. *The 4th order central moment of u is the flatness of u*

$$F \equiv \langle (u - \langle u \rangle)^4 \rangle, \tag{A.13}$$

and can be approximated by

$$F = \overline{(u - \overline{u})^4}. \tag{A.14}$$

The gaussian probability density function has a flatness of $F = 3$, and for direct comparison with this distribution it is common to use the kurtosis, which Monin & Yaglom (1971) called the excess.

Definition A.8. *The kurtosis of u is defined as*

$$K = F - 3. \tag{A.15}$$

Tennekes & Lumley (1972, page 200) defined the kurtosis as equal to the flatness, which is not strictly correct.

A.3.3 Joint probability distribution and covariance

The concept of a probability density function can be extended to more than one variable. The joint probability density function $B(u, v)$ expresses the joint probability of finding u between u and $u + du$, and v between v and $v + dv$. It is defined such that

$$\int_{-\infty}^{\infty} \int_{-\infty}^{\infty} B(u, v) \, du \, dv = 1. \tag{A.16}$$

The moments of a joint probability distribution can be defined in a similar way as the moments of a single variable distribution.

Definition A.9. *The mth and nth order joint moment of u and v is defined as*

$$\langle u^m v^n \rangle \equiv \int_{-\infty}^{\infty} \int_{-\infty}^{\infty} u^m v^n B(u, v) \, du \, dv \, . \tag{A.17}$$

The most commonly used joint moment is $\langle uv \rangle$, for $m = n = 1$, which is called the covariance. The covariance is a measure of the asymmetry of $B(u, v)$.

A commonly used measure of correlation between two variables u and v is the Pearson product-moment correlation coefficient, often just called the correlation coefficient. The correlation coefficient is defined as

$$\text{corr}(u, v) = \frac{\langle uv \rangle}{\sigma_u \sigma_v} \tag{A.18}$$

and measures how well (u, v) follows a linear dependendence.

A.3.4   Filtering

To get a better idea of the concept of scale, it is useful to introduce the idea of filtering. A function u can be represented by the Fourier series

$$u(\boldsymbol{x}) = \sum_{\boldsymbol{\kappa}} \hat{u}_{\boldsymbol{\kappa}} e^{i\boldsymbol{\kappa}\boldsymbol{x}}, \quad \boldsymbol{\kappa} \in \frac{2\pi}{L} \mathbb{Z}^3, \tag{A.19}$$

and associated with a length scale l there is a filtering scale K_l such that $l = K_l^{-1}$. To separate the range of large scales, from that of smaller scales, the idea of the high-pass and low-pass filters is introduced.

Definition A.10. *The low-pass filtered function of u is defined as*

$$u_{K_l}^{<}(\boldsymbol{x}) \equiv \sum_{\kappa \leq K_l} \hat{u}_{\boldsymbol{\kappa}} e^{i\boldsymbol{\kappa}\boldsymbol{x}}. \tag{A.20}$$

Definition A.11. *The high-pass filtered function of u is defined as*

$$u_{K_l}^{>}(\boldsymbol{x}) \equiv \sum_{\kappa > K_l} \hat{u}_{\boldsymbol{\kappa}} e^{i\boldsymbol{\kappa}\boldsymbol{x}}. \tag{A.21}$$

A.4 Symmetry and scale invariance

When studying physical systems it is often useful to study symmetries. Symmetry in this context is used in the extended definition as any invariance group of the system. The Navier-Stokes equations have several invariance groups or symmetries, including space-translation, time-translation, Galilean transformation, parity, rotation and scaling symmetry (Frisch, 1995). In the context of this project, scaling symmetry is of most interest.

Using A.1 and ignoring f_i yields

$$\frac{\partial u_i}{\partial t} + u_j \frac{\partial u_i}{\partial x_j} = -\frac{1}{\rho} \frac{\partial p}{\partial x_i} + \nu \frac{\partial^2 u_i}{\partial x_j \partial x_j}. \tag{A.22}$$

Introducing the scaling $u_i \to \lambda^n u_i$, $t \to \lambda^{1-n} t$, $x_i \to \lambda x_i$ and knowing that p/ρ scales as velocity squared gives

$$\lambda^{2n-1} \frac{\partial u_i}{\partial t} + \lambda^{2n-1} u_j \frac{\partial u_i}{\partial x_j} = -\lambda^{2n-1} \frac{1}{\rho} \frac{\partial p}{\partial x_i} + \lambda^{n-2} \nu \frac{\partial^2 u_i}{\partial x_j \partial x_j}. \tag{A.23}$$

This is only true for $n = 1$, but when neglecting viscosity there are infinitely many scaling groups that satisfy the equation. Thus for high Reynolds number flow, one would expect some sort of scale invariant behaviour.

For turbulent flow it is more useful to consider statistical symmetry as the traditional symmetries will be broken for a single solution. Statistical space translation symmetry corresponds to homogeneous turbulence, while statistical rotation symmetry corresponds to isotropic turbulence. Due to the presence of solid boundaries, turbulence is seldom homogeneous, isotropic or strictly self-similar. However, many turbulent flows suggest some form of homogeneity, isotropy and scale-invariance.

A.4.1 Scales in turbulence

It has already been mentioned that turbulence is a phenomenon with a large range of scales. Due to physical constraints there cannot be an infinite range of scales, and so there must be a lower and upper cut-off scale. The upper cut-off point is determined by the geometrical constraints of the problem, as the turbulent eddies cannot be much larger than the large scale geometry.

At the lower end, there is the point at which the viscous forces become significant and the turbulent motion dissipates. This is known as the

Kolmogorov length scale η, which can be estimated as $\eta/D = \left(\varepsilon Re^3\right)^{-\frac{1}{4}}$ using the terminology defined earlier in this chapter. There can be even smaller scales related to scalar transport in the flow. The Batchelor scale is defined as $\eta_B = \eta/Sc^{\frac{1}{2}}$. For high Schmidt number flow the Batchelor scale can be significantly smaller than the Kolmogorov scale.

The idea of scales can be illustrated with the high-pass and low-pass filtrations. The small scales of turbulence are what remain after a high-pass filtration of a Fourier representation of the signal. The large scales are what remain after a low-pass filtration of the signal.

A.4.2   Self-similarity in turbulence

Perhaps the most famous, and one of the earliest, accounts of the apparent self-similarity of turbulence was written by Richardson (1922) in his famous rhyme.

> Big whorls have little whorls
> Which feed on their velocity
>
> And little whorls have lesser whorls
> And so on to viscosity
> (in the molecular sense)

Richardson's rhyme suggests a physical notion of self-similarity in turbulence. The study of self-similarity was then shifted to wavenumber space, most significantly by Kolmogorov (1941b,c,a,d). One of the most well known results in turbulence is Kolmogorov's $\frac{5}{3}$ energy spectrum law. In an intermediate range in the turbulence energy spectrum, known as the inertial range, the turbulence energy related to a wavenumber κ is proportional to $\kappa^{-\frac{5}{3}}$.

Another important result is the two-thirds law, stating that the second order structure function follows an $l^{\frac{2}{3}}$ law. This result also implies a $\kappa^{-\frac{5}{3}}$ law in the energy spectrum. Kolmogorov also suggested that structure functions S_p should have scaling exponents $\zeta_p = \frac{p}{3}$.

Kolmogorov's hypotheses suggest power law behaviour and self similarity in the wavenumber space. This approach to self-similarity is also described in detail by Hinze (1975) and Monin & Yaglom (1971, 1975). A modern account of Kolmogorov's hypotheses is given by Frisch (1995).

The notion that turbulent eddies are spatially compact structures, and not Fourier modes, has led to more geometrical studies of self-similarity

in turbulence in real space. One of the most significant proponents for the study of self-similarity in real space was Benoit B. Mandelbrot who is considered the father of fractal geometry.

To give a description of self-similarity in real space for a turbulent interface, the idea of fractality seems appropriate. Instead of trying to describe the geometry of turbulence using regular objects of Euclidian geometry, the irregular and inherently self-similar fractal geometry can be used.

Appendix B

Fractal geometry

A brief introduction to fractal geometry is given, along with the necessary mathematical theory to support the definitions. The chapter starts with a description of the geometrical concept that is a fractal, is then followed by the mathematical foundation for the theory of fractal geometry, and ends with some examples of fractals and applications.

The seminal work on fractal geometry is from Mandelbrot (1982), the revised essay on fractals. More modern accounts of fractal geometry are given by Falconer (2003) and Schroeder (1991).

B.1 What is fractal geometry?

Mathematics has traditionally been mostly concerned with the geometry of well-behaved differentiable surfaces. The idea of a fractal geometry was developed to be able to study the geometric properties of sets that were not smooth. The term *fractal* was initially conceived by Mandelbrot from the Latin word *fractus*, meaning broken or irregular, and he created the unifying field of fractal geometry (Mandelbrot, 1982). The idea of a set having non-integer dimension, is however much older.

The need for a geometry of non-smooth sets arose from the realisation that nature is rarely smooth, and that Euclidian geometry is not sufficient to describe natural phenomena.

A clear definition of a fractal is hard to find, but it is possible to create a list of properties that most fractals will satisfy.

1. Too irregular to be described by Euclidian geometry.

2. A large range of scales.

3. A certain degree of self-similarity among scales, either exact, approximate or stochastic.

4. A Hausdorff dimension greater than the the topological dimension.

5. A simple recursive description.

Property number 4 was the fractal definition used by Mandelbrot (1982), but this does not hold for all fractals.

B.2   Dimension

To introduce the idea of a fractal dimension and clarify what the term fractal dimension will mean in this report, a survey of the subject of dimensions is given. This includes a brief introduction to measure theory and then a mathematical definition of the Hausdorff dimension and the box-counting dimension. The idea of a fractal dimension is then discussed. For all of these dimensions, the general idea is that of a measurement at scale δ, that is for each δ a set is measured in such a way that irregularities smaller than δ are ignored.

B.2.1   Dimensions and topology

The dimension of a set says something about how disconnected it is, or how much space is occupied around each point in the set. In topology in Euclidian space, the dimension is a measure that for a point is equal to zero, for a line is equal to one, for a surface is equal to two and for a volume is equal to three. There is also an idea of dimension for more general sets, but it is much less intuitive and not always easily computed.

B.2.2   Set theory and measures

In mathematics a measure is a way of assigning a size to a set, in much the same way that one could assign a mass distribution to a set. The idea is to have a property, or measure, that is such that if the set is divided into a countable number of subsets in a reasonable way, then the measure of the whole set is equal to the sum of all the subset measures. A simple example of a measure is a counting measure, where the measure of a set is

equal to the number of points in the set. Another well known measure is the n-dimensional Lebesque measure $\mathcal{L}^n$ which evaluates the n-dimensional volume of a general set.

In order to proceed, a few set theory definitions are needed. For a non-empty subset of $\mathbb{R}^n$, F of real numbers we have.

Definition B.1. *The supremum* $\sup F$ *is the smallest number n such that* $\phi \leq n$ *for all* $\phi \in F$.

Definition B.2. *The infinum* $\inf F$ *is the largest number n such that* $\phi \geq n$ *for all* $\phi \in F$.

Definition B.3. *The diameter* $|F|$ *is the largest distance between any two points in F, i.e.* $|F| = \sup\{|\phi_1 - \phi_2| : \phi_1, \phi_2 \in F\}$.

B.2.3 The Hausdorff measure and dimension

F is a non-empty subset of the n-dimensional Euclidian space $\mathbb{R}^n$, $|F|$ is the diameter of F and $\{F_i\}$ is a finite collection of sets with diameter at most δ, covering F. $\{F_i\}$ is called a δ-cover of F and s is assumed non-negative. Then

$$\mathcal{H}_\delta^s \equiv \inf \left\{ \sum_{i=1}^\infty |U_i|^s : \{U_i\} \text{is a } \delta\text{-cover of } F \right\}, \tag{B.1}$$

and the Hausdorff measure can be defined.

Definition B.4. *The s-dimensional Hausdorff measure of F is the smallest possible sum of the s-power diameters of* $|U_i|$, *when the supremum diameter* δ *goes to zero.*

$$\mathcal{H}^s(F) \equiv \lim_{\delta \to 0} \mathcal{H}_\delta^s(F) \tag{B.2}$$

When evaluating $\mathcal{H}^s$ for different values of s, $\mathcal{H}^s$ jumps from infinity to zero at a critical value. This value is called the Hausdorff dimension of F, and is defined.

Definition B.5. *The Hausdorff dimension of F is the value of s at which the s-dimensional Hausdorff measure of F jumps from infinity to zero.*

$$\dim_\mathcal{H} F \equiv \sup\{s : \mathcal{H}^s(F) = \infty\} \tag{B.3}$$

The Hausdorff dimension is often difficult to compute, and because of this, other dimensions can be more convenient to use. However, the Hausdorff dimension is an important theoretical concept that defines the idea of a divider dimension in the most rigorous way.

B.2.4   The box-counting dimension

Again, the non-empty subset F of $\mathbb{R}^n$ is studied. N_δ is the smallest number of sets of diameter at most δ that covers F. Then the box-counting dimension can be defined.

Definition B.6. *The box-counting dimension is defined as*

$$\dim_B F \equiv \lim_{\delta \to 0} \frac{\log N_\delta(F)}{-\log \delta}, \tag{B.4}$$

if the upper and lower limits are equal.

There are many ways of covering F with a suitable collection of subsets, and the best suited covering depends on the set F.

B.2.5   The fractal dimension

For both the Hausdorff dimension and the box-counting dimension, the general idea is that of a measurement at scale δ. It will often be difficult to use the strict definitions of Hausdorff and box-counting dimension for sets outside the domain of pure mathematics. It is practical to use a less strict definition.

If a set F is measured at scale δ and the number of steps required to cover F obeys the power law

$$N(F) \sim c\delta^{-D_F}, \tag{B.5}$$

then D_F is the divider dimension of F and c is the D_F-dimensional length. This means that $-D_F$ is the slope of a log-log plot of N as a function of δ, which is very convenient when it is difficult to allow δ to approach zero. We call D_F the fractal dimension of F.

The idea of a fractal dimension is, although quite commonly used, not rigorously defined. This has led to numerous different definitions and often inconsistency in the treatment of the fractal dimension. Because of this, some authors advice against the use of the term "fractal dimension" (e.g. Falconer (2003) and Vassilicos (1989)). It is, however, a term commonly used in scientific publications.

B.2.6   Intersection of surfaces

In turbulence research and many other fields, it is difficult to get complete three-dimensional data, and one is often forced to study planes of intersections. Because of this, it will not be possible to find the fractal dimension of a set in $\mathbb{R}^3$ directly, and instead one must determine the fractal dimension of the intersection of the set and a plane or a line.

To assess the dimension of the set itself, one then has to find a relation between the dimension of a set and the dimension of an intersection. This problem is discussed for general sets in Mandelbrot (1982, pp. 135–136) and Falconer (2003, pp. 109–119).

For the purpose of this study, one can generally say that the intersection of a set F in $\mathbb{R}^3$ and a sufficiently thin plane, that is thinner than the smallest scale in F, has a dimension that is one less than the dimension of F, if and only if the resulting dimension is independent of the orientation of the intersecting plane. For a line, the dimension of the intersection will be two less than the dimension of the set. For sufficiently sparse sets, the intersection set could be empty.

For this study, the dimension of a line in two orthogonal intersecting planes is being used to infer the dimension of a surface in $\mathbb{R}^3$.

B.3   Some examples of fractals

B.3.1   The Cantor set

The Cantor set is one of the oldest and also simplest fractals, yet it possesses many interesting properties. The Cantor set is constructed by starting with a line of length unity, and removing the middle third section. This process is repeated infinitely many times, and what remains is the Cantor set. An illustration of the Cantor set after the first six iterations is shown in figure B.1. In this figure, what are actually points, are drawn as bars to make the illustration clearer.

As the Cantor set is completely discontinuous, it must have a dimension that is less than one. At the same it is much denser around each point than a collection of points of zero dimension. It then follows intuitively that the dimension of the Cantor set must lie somewhere between zero and one. The Cantor set satisfies many of the common traits of fractals, i.e. self similarity, fine structure, simple recursive definition and a Hausdorff dimension which is strictly greater than the topological dimension.

Figure B.1: The Cantor set after six iterations.

The length of the set measured at scale δ can be expressed recursively as

$$L\left(\frac{\delta}{3}\right) = \frac{2}{3}L\left(\delta\right),\tag{B.6}$$

which has the solution

$$L(\delta) = \delta^{1-D},\tag{B.7}$$

$$D = \frac{\log 2}{\log 3} \approx 0.6309\tag{B.8}$$

where D is a divider dimension of the Cantor set. This is also equal to the Hausdorff dimension of the Cantor set.

B.3.2   Julia sets

The Julia sets are a collection of self-similar recursively defined sets, from a polynomial function. A special category of Julia sets are the quadratic Julia sets defined from the recursive assignment

$$Z \to Z^2 + Z_0,\tag{B.9}$$

in the complex plane. Different values of Z_0 yield the collection of quadratic Julia sets.

The so-called filled-in Julia set contains all values in $\mathbb{C}$ such that assignment (B.9) is limited, i.e. does not go to infinity. The Julia set is the boundary of the filled-in Julia set. The quadratic Julia set for $Z_0 = -1$ has a Hausdorff dimension of 1.2683, and is shown in figure B.2.

A special case of the Julia set is the well known Mandelbrot set, which is the set of all Z_0 such that the Julia set, defined from equation (B.9), is connected.
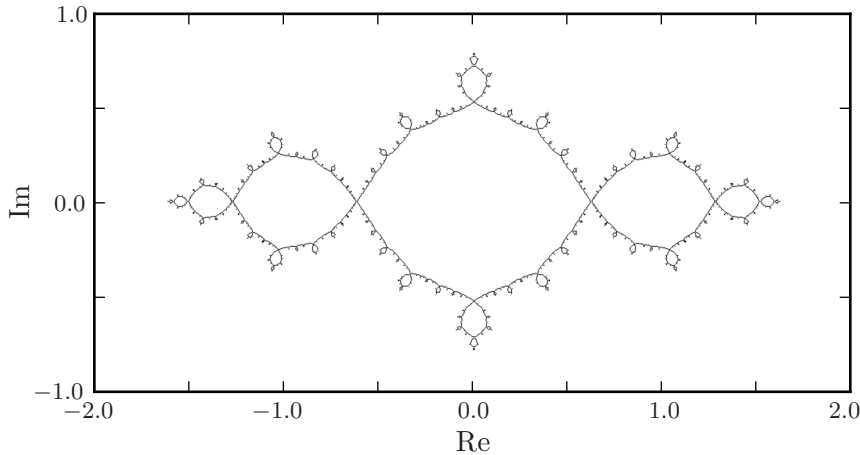
Figure B.2: The Julia set $Z \to Z^2 - 1$.

B.3.3 Fractional Brownian motion

The fractals described thus far have been deterministic fractals, described by an exact recursive rule. Another type of fractal is the random fractal or stochastic fractal. For a random fractal, the recursive divider rule is a stochastic process. Brownian motion is a typical example of a random fractal.

Brownian motion, or the Wiener process, is a Gaussian process. The process starts in the origin and moves by independent and normally distributed increments. An example of a realisation of one-dimensional Brownian motion is plotted in figure B.3.

For many purposes random functions with different properties to Brownian motion are useful. A variation of Brownian motion is fractional Brownian motion, which has normally distributed, but not independent, increments. For simplicity, one-dimensional fractional Brownian motion is first considered.

Fractional Brownian motion with a Hurst index $H \in (0, 1)$ is a Gaussian process $u : [0, \infty) \to \mathbb{R}$, where the increment $u(x + l) - u(x)$ is normally distributed with mean zero and variance l^{2H}. The joint moment $\langle u(x)u(x + l) \rangle$ is expressed as

$$\langle u(x)u(x + l) \rangle = \frac{1}{2} \left(x^{2H} + (x + l)^{2H} - l^{2H} \right), \tag{B.10}$$
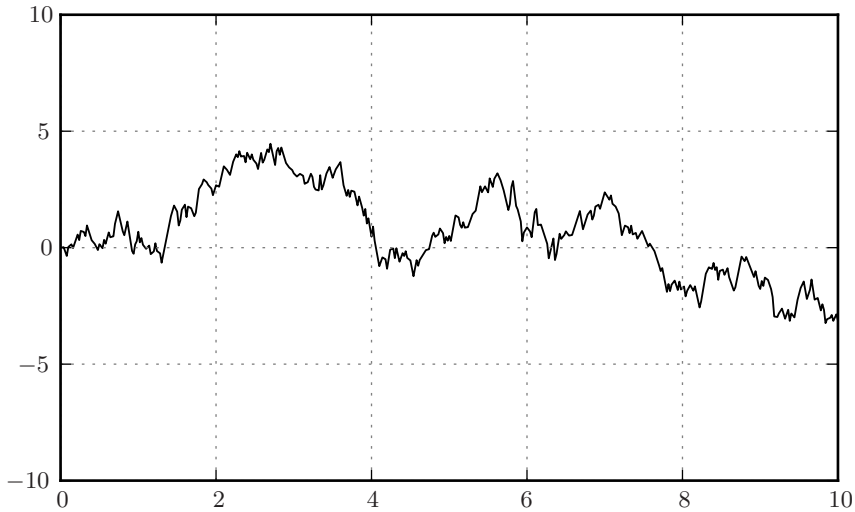
Figure B.3: A realisation of one-dimensional Brownian motion.

and the second order structure function S_2 is

$$S_2(l) = \langle [\,\Delta u\,(l)]^2 \rangle = l^{2H}. \tag{B.11}$$

For $H > \frac{1}{2}$ the increments are positively correlated, for $H < \frac{1}{2}$ the increments are negatively correlated, and for $H = \frac{1}{2}$ the process is regular Brownian motion.

The power spectrum of $u(x)$ is expected to follow $\kappa^{-(1+2H)}$, and the Hausdorff and box-counting dimensions are $2-H$. The fractional Brownian motion can be extended to two dimensions, yielding a fractional Brownian surface, by replacing x with coordinates (x, y). Then, l is a length in two-dimensional space, and the dimensions are equal to $3 - H$.

For a specific Hurst index, $H = \frac{1}{3}$, the fractional Brownian surface has a second order structure function equal to $l^{\frac{2}{3}}$, a power spectrum following $\kappa^{-\frac{5}{3}}$, and Hausdorff and box-counting dimensions equal to $\frac{8}{3} \approx 2.67$.

B.4   Applications

Fractal geometry has typically been used to describe the geometry of objects that are too irregular to be described using Euclidian geometry.   This

includes most of the objects in nature. In the introduction to his essay, Mandelbrot noted that nature is rarely smooth.

> Clouds are not spheres, mountains are not cones, coastlines are not circles, and bark is not smooth, nor does lightning travel in a straight line. (Mandelbrot, 1982)

Fractals have perhaps most famously been used to describe coastlines, after the realisation that the length of a coastline is highly dependent on the scale of the measurement. Also mountains and clouds have been described as fractal, and convincing mountains and clouds can been generated using random fractals. Fractal geometry has further been used in signal processing and antenna technology.

It is obvious that natural objects do not behave as perfectly fractal as the mathematical fractals. The self-similarity is not exact and not defined for an infinite range of scales. So there is a lower and upper cut-off point, beyond which the object is no longer fractal. Nevertheless, fractal geometry can be useful to describe the region that is approximately fractal.

Another field where fractals have been used is finance. Mandelbrot proposed a fractal description of financial instruments, because the commonly used Gaussian statistics did not sufficiently encompass the uncertainty in finance and the importance of large deviations. Mandelbrot & Hudson (2006) presented a new theory of finance, based on fractal geometry.

B.4.1 Fractals and turbulence

The application of fractal geometry to something that is by definition smooth like fluid flow, might at first appear contradictory. However, if limited to an intermediate range of scales, a fractal description could be justified. The scale-invariance in turbulence discussed in section A.4 would suggest that a fractal description could have merit. Any self-similarity in turbulence can only be stochastic, and so turbulence will mostly resemble random fractals.

It could also be argued that turbulence geometrically resembles objects of fractal geometry more than the classical objects of Euclidian geometry. It should be clear that a turbulent wake is no more a cone frustum than mountains are cones.

Fractals have been used in different ways in turbulence. A fractal description of the geometry of lines or surfaces in turbulence have been

proposed by several authours. More recently fractals have been used to model turbulence, and fractally forced turbulence has been studied.

Appendix C

Programming

A program was created to solve the stochastically forced Burgers equation. A description of the most important features of this program is given in this appendix.

C.1   Program structure

The programming language Fortran was used to create the part of the program that performs the actual computations. Fortran is a popular programming language for numerical computations because of the computational speed of the compiled programs. The Fortran program was compiled using the GNU Fortran compiler with compilation flags `-O3` and `-march=native` for optimisation. All simulations were run on a desktop computer with a x86-64 quad-core processor; the code was not parallelised.

The Fortran program has a simple structure where a main program communicates with a number of subroutines, each doing a specialised task. There are subroutines for data import, data export, initialisation, grid generation, spatial discretisation, temporal discretisation, subgrid modelling and the source term. For each of these classes there are several different subroutines, for example for different discretisation methods and subgrid models. The desired subgrid models are decided by the user and chosen using procedure pointers in the main program. The procedure pointers are the only Fortran 2003 feature in the program; the rest is strictly Fortran 95.

To simplify the use of this program a front end, consisting of one Python script and one BASH script, is developed to communicate with the Fortran

program. The BASH script defines commands used by the user and the
Python script imports values from a setup file and sends these values to the
Fortran program.

C.2   Implementing the FFT algorithm

In order to compute the stochastic source term for each time step, a set of
Fourier modes with amplitude $(A/\sqrt{\Delta t})k^{-\alpha/2}$ and phases randomly chosen
uniformly in $[0, 2\pi]$ were prescribed. The power law exponent α specifies
the energy spectrum of the forcing. The prescribed Fourier modes were
then inversely Fourier transformed using the fast Fourier transform (FFT)
(Cooley & Tukey, 1965) to get the force in real space. Using the FFT
algorithm takes advantage of the periodicity of the Fourier modes and
reduces the computational effort from N^2 to $N \log_2(N)$ operations. An
introduction to the FFT algorithm was written by Bergland (1969).

A simple radix-2 Fast Fourier Transform algorithm was first imple-
mented in a Fortran subroutine to handle the inverse Fourier transform.
For added flexibility and optimisation, this algorithm was later replaced
with the FFTW (Fastest Fourier Transform in the West) library (Frigo &
Johnson, 2005), yielding considerable speed improvements.

C.3   Using the program

Because of the large number of simulations, it would be inconvenient to
modify and compile the Fortran program for each parameter change. The
program therefore imports all specified parameters from a setup file, and
predefined commands are used to use the program. These commands are
defined in the BASH script and are listed here.

`master-cfd new-project [project name]` creates a new project
called [project name] in the current directory. A standard setup file
`[project name].SETUP` is created in the current directory. This is the
only command that depends on the current directory.

`master-cfd run [project name]` runs the simulation titled [project
name].

`master-cfd run-all [project name]` runs all the simulations located
in the same folder as [project name].

`master-cfd stop [project name]` stops the simulation titled [project
name].

 `master-cfd restart [project name]` restarts the simulation titled [project name] by initialising the simulation from the last time step that was written to file.

 `master-cfd remove [project name]` removes the project titled [project name].

 `master-cfd tail [project name]` displays the progress of the simulation [project name]. The total elapsed time, the flow time, the number of time steps and one velocity value is printed to standard output each time step.

 `master-cfd get-pid [project name]` prints the process ID of [project name] to standard output.

 `master-cfd edit [project name]` opens the setup file `[project name].SETUP` for editing.

 `master-cfd list-projects` writes a list of all the simulation projects stored on the computer to standard output.

 `master-cfd find-project [project name]` writes the location in the file system of [project name] to standard output.

 `master-cfd about-project [project name]` writes the contents of the file `[project name].SETUP` to standard output.

 An example of what a typical setup file contains follows.

```
#===============================================================
#                    Setup file for master-cfd
#===============================================================

grid = {
    "xmin": 0,
    "xmax": 1,
    "nx":    250
}
spatial_discretisation = {
    "flux_function": "arakawa_flux"
}
time_discretisation = {
    "scheme": "RK_TVD",
    "dt":    0.00001,
    "tmax": 1000
}
physical_parameters = {
```

```
    "kinematic_viscosity":  0.000005,
    "power_fluid_index" :   1
}
boundary_conditions = {
    "type": "periodic"
}
initialisation = {
    "type": "stochastic",
    "k1":    0.5,
    "k2":    -0.833333,
    "k3":    0.5,
    "k4":    0,
    "k5":    0,
    "k6":    0
}
output = {
    "output_rate": 1000
}
source = {
    "type": "stochastic",
    "coefficient": 0.25,
    "spectrum": -0.5,
    "l":      0.5,
    "small_scale": 0
}
sgs_model = {
    "type": "multifractal"
}
random_number = {
    "seed": "clock"
}
```

Those familiar with the Python programming language will notice that the setup file contains dictionary classes, making it very easy to import all the values from the file. The different parameters specified in the setup file should be mostly self-explanatory.

Appendix D

A computational study of Burgers turbulence

A computational study of Burgers turbulence

Christopher Nilsen and Helge I. Andersson

Department of Energy and Process Engineering
The Norwegian University of Science and Technology
e–mail: chrinil@stud.ntnu.no, helge.i.andersson@ntnu.no

Summary New simulations of the stochastically forced Burgers equation using the finite volume method compare favourably with previously published results using a pseudo-spectral code. Low resolution simulations without subgrid modelling exhibit sufficient dissipation to avoid build-up of energy. White (k^0), pink (k^{-1}) and brown (k^{-2}) energy spectra for the stochastic sources result in energy spectra for the solutions proportional to k^{-1}, $k^{-5/3}$ and k^{-2}, respectively.

Introduction

When J. M. Burgers introduced the Burgers equation, he intended it to be a model equation for turbulence. The Burgers equation contains the same type of advective non-linearity and diffusion term as the three dimensional Navier-Stokes equations. When it was discovered that an explicit analytical solution to the Burgers equation could be found [13, 6], it seemed unlikely that solutions to the Burgers equation could contribute to the study of turbulence. One of the characteristic features of the Navier-Stokes equations and turbulence, is the sensitivity to changes in initial conditions. In real turbulence apparent randomness spontaneously develops; this does not happen with the Burgers equation.

The Burgers equation is a nonlinear wave equation, and has found applications in nonlinear acoustics and other wave problems. A review was written by Gurbatov *et al.* [12]. Other applications include cosmology, condensed matter and statistical physics, and also the study of vehicular traffic. This is elaborated on by Frisch & Bec [9] and references therein.

A common usage of the Burgers equation is also as a testing ground for the three-dimensional Navier-Stokes equations, both with regards to testing numerical methods and studying the physics. Because the terms in the Burgers equation are similar to those in the Navier-Stokes equations, new numerical methods can typically be tested for the Burgers equation, with the added convenience of exact solutions.

Even though the Burgers equation was initially thought to be a model equation for turbulence, the standard Burgers equation has little to do with turbulence. As will be seen, the addition of a source term can make the solution of Burgers equation resemble turbulence. The use of the Burgers equation to study turbulence has gained renewed popularity in recent years (1980s and onwards), and the study of random solutions to the Burgers equation is sometimes referred to as "burgulence". The randomness can either enter through a random initial condition or a stochastic source term, the latter being the approach studied here. There have been many studies on Burgers turbulence in recent years, and on how it relates, or does not relate, to real three-dimensional turbulence. Many of these studies are referenced by Frisch & Bec [9].

Analytical solutions to the Burgers equation are well documented and the dominance of shocks in the solution leads to an energy spectrum proportional to k^{-2} [3]. She *et al.* [15] studied solutions to the Burgers equation in the limit of vanishing viscosity with a fractional Brownian initial condition. A companion paper by Sinai [16] studied the statistics of shocks for the same problem. Both showed an energy spectrum proportional to k^{-2}, characteristic of the shocks in the solution.

The study of the stochastically forced Burgers equation has been the topic for many papers. Notably, simulations published by Checklov & Yakhot [4, 5, 18] provided new insight into the physics of Burgers turbulence. It was shown that the one-dimensional Burgers equation with stochastic forcing exhibited turbulence-like properties, provided that the stochastic force was white in time and had a k^{-1} spatial energy spectrum. The numerical experiments revealed an energy spectrum proportional to $k^{-5/3}$, and strong intermittency.

The topic of this study is the numerical solution of stochastically forced Burgers turbulence using the finite volume method. Different discretisation schemes are tested, and an investigation of the effect of different sources was carried out to identify how the energy spectrum of the solution was influenced by the source term. Furthermore, the objective was to identify which source type yielded a solution with most turbulence-like properties. Special emphasis was placed on the case when the source term had a k^{-1} energy spectrum.

The stochastically forced Burgers equation

The Burgers equation is a quasi-linear parabolic partial differential equation in one-dimensional space and time. It was first suggested by Burgers [2] as a model equation for studying turbulence. The Burgers equation,

$$\frac{\partial u}{\partial t} + \frac{\partial}{\partial x}\left(\frac{1}{2}u^2\right) = \nu\frac{\partial^2 u}{\partial x^2}, \tag{1}$$

can be considered as a one-dimensional version of the Navier-Stokes equations without pressure forces. The Burgers equation describes a compressible flow, as only trivial incompressible flows exist in one dimension, and ν plays the part of a diffusivity or kinematic viscosity. All variables are treated as non-dimensional, leading to ν being interpreted as an inverse Reynolds number.

The stochastically forced Burgers equation is the Burgers equation with the addition of a stochastic source term, i.e.

$$\frac{\partial u}{\partial t} + \frac{\partial}{\partial x}\left(\frac{1}{2}u^2\right) = \nu\frac{\partial^2 u}{\partial x^2} + G(x,t), \tag{2}$$

where $G(x,t)$ is the stochastic source. Statistical properties of the source can be varied and are expected to affect the statistics of the results. For the simulations presented here the source is white noise in time, but with spatial correlation. The source is described by the energy spectrum

$$\overline{|\hat{G}(k)|^2} \propto k^{-\alpha}, \tag{3}$$

where $-\alpha$ is the slope of the spectrum, $\hat{(\cdot)}$ denotes the Fourier transform and $\overline{(\cdot)}$ temporal averaging. Here and in the rest of the paper, k is the absolute value of the wave number. Every function of k will then include the contribution from both positive and negative wave numbers.

Equation (2) is not just the governing equation for a type of Burgers turbulence, as studied here, it has also been proven useful in other applications including the study of stochastic growth of interfaces [1].

Numerical methods

The stochastically forced Burgers equation has been solved using a finite volume method (FVM) code. A Fortran 95 code was developed, together with a simple front-end consisting of Python

and BASH scripts. The Fortran program was compiled using the GNU Fortran compiler with compilation flags `-O3` and `-march=native` for optimisation. All simulations were run on a desktop computer with a x86-64 quad-core processor; the code was not parallelised.

Different discretisation methods have been implemented in the FVM code, to allow for comparison and validation. The diffusive flux is discretised using a central difference method, having second order theoretical accuracy. The convective flux is approximated by two different commonly used flux functions, the upwind method (Roe's approximate Riemann solver) and the local Lax-Friedrichs (LLF) method. Both methods are first order accurate, and in order to increase the order of accuracy, MUSCL interpolation [17] has also been used. The discretised equation was solved on an equidistant grid.

The MUSCL interpolation technique replaces the piecewise constant reconstruction with a linear reconstruction, and consequently increases the order of accuracy of the method. This interpolation yields left and right values at the cell faces expressed as

$$u_L = u_j + \frac{1}{4}\left[(1-\kappa)\Delta^+ u_j + (1+\kappa)\Delta^- u_j\right], \qquad (4)$$

$$u_R = u_{j+1} - \frac{1}{4}\left[(1-\kappa)\Delta^- u_{j+1} + (1+\kappa)\Delta^+ u_{j+1}\right], \qquad (5)$$

where $\Delta^+ u$ and $\Delta^- u$ are the minmod-limited velocity differences

$$\Delta^+ u_j = \text{minmod}\left(\Delta u_{j-\frac{1}{2}}, \beta\,\Delta u_{j+\frac{1}{2}}\right), \qquad (6)$$

$$\Delta^- u_j = \text{minmod}\left(\Delta u_{j+\frac{1}{2}}, \beta\,\Delta u_{j-\frac{1}{2}}\right), \qquad (7)$$

$\Delta u_{j+\frac{1}{2}} = u_{j+1} - u_j$ and the minmod limiter is defined as

$$\text{minmod}(a,b) = \frac{1}{2}(\text{sign}(a) + \text{sign}(b))\min(|a|,|b|). \qquad (8)$$

Using the minmod limiter reduces the order of accuracy to first order at local extrema, but ensures that oscillations are avoided. Combined with the upwind Riemann solver this yields the third order upwind method, for $\kappa = 1/3$. A value of $\beta = 2/3$ is recommended [10, page 147]. The MUSCL interpolation technique with $\kappa = 1/3$ and $\beta = 2/3$ is also tested for the local Lax-Friedrichs method.

Both the explicit Euler method and the third order total variation diminishing (TVD) Runge-Kutta method of Gottlieb & Shu [11] have been used to integrate the equation in time. The time step has for each simulation been chosen such that the difference between the solution using the explicit Euler method and the TVD Runge-Kutta method is negligible.

In order to compute the stochastic source term for each time step, a set of Fourier modes with amplitude $(A/\sqrt{\Delta t})k^{-\alpha/2}$ and phases randomly chosen uniformly in $[0, 2\pi]$ were prescribed. The power law exponent α specifies the energy spectrum of the forcing. The Fourier modes were then inversely transformed using the fast Fourier transform (FFT) [7] to get the force in physical space. Using the FFT algorithm takes advantage of the periodicity of the Fourier modes and reduces the computational effort from N^2 to $N\log_2(N)$ operations.
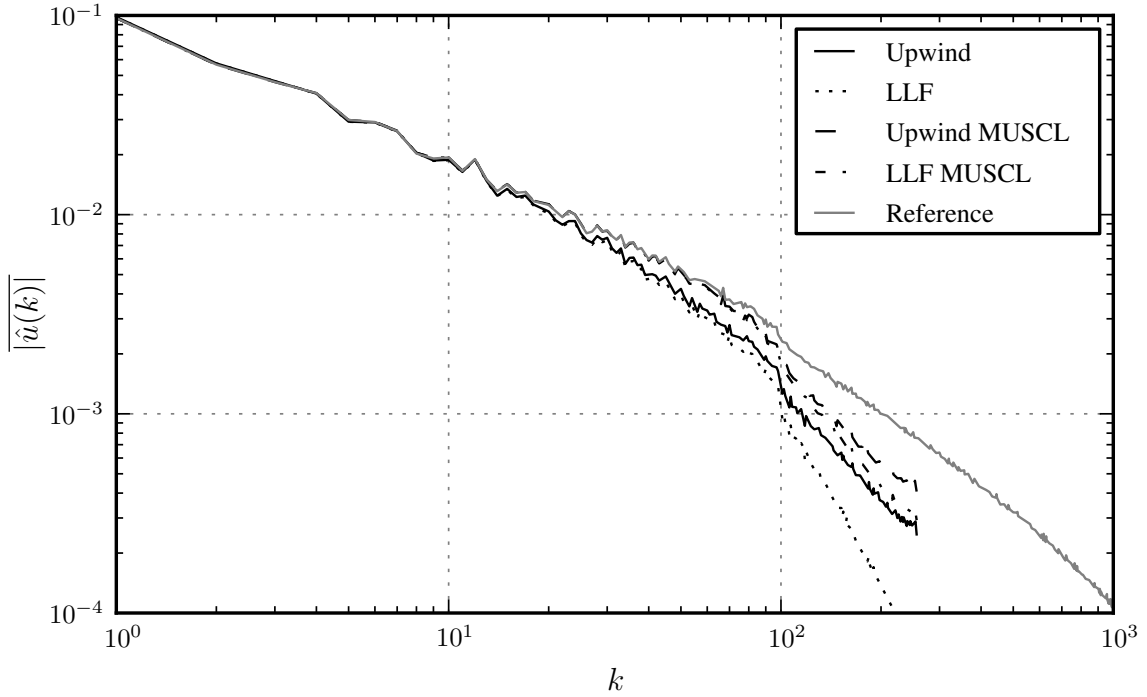
Figure 1: The averaged amplitude spectra of the velocity for the four different convective flux functions for 2^9 grid cells are compared with a reference simulation using the LLF method with MUSCL for 2^{13} grid cells.

Results and discussion

Convective flux discretisation

To compare the different flux functions, low resolution simulations of the stochastically forced Burgers equation have been compared with a high resolution reference simulation. Source statistics are described by an amplitude constant $A = 0.05$, spectrum $\alpha = 1$ and an upper cut-off wave number of $k = 100$. The equation was integrated in time using the TVD Runge-Kutta method with $\Delta t = 5 \cdot 10^{-5}$, and statistics are computed from $t = 0$ until $t = 10$, starting from initial condition $u_0 = 0$. The kinematic viscosity was $\nu = 1 \cdot 10^{-5}$, and periodic boundary conditions were used.

Simulations for 2^9 grid cells in $[0, 1]$ were compared with a reference simulation of 2^{13} grid cells using the LLF method and MUSCL. For the low resolution simulations all four flux function combinations, upwind and local Lax-Friedrichs with and without MUSCL, were tested.

Averaged amplitude spectra for the results are plotted in figure 1 to investigate how well the different methods perform at low and high wave numbers. The spectra at the low resolutions are plotted up until $k = 1/(2\,\Delta x\,)$, beyond which no spectral information exists. The Fourier transform is calculated using the FFT algorithm.

The first order methods start deviating from the reference simulation already at wave number 20, while the higher order methods follow this reference until $k = 70$. All methods end up deviating significantly, demonstrating that the resolution is too low. In addition to yielding superior results for the higher order methods, the amplitude spectra also appear to exhibit less high wave number damping for the upwind flux function. This difference is less significant for the simulations utilising the MUSCL interpolation technique.

Forcing spectrum

The statistical properties of the stochastic force are to a large degree described by the Fourier spectrum. Three of the most well known types of noise functions are white noise with an energy spectrum $\propto k^0$, pink noise with energy spectrum $\propto k^{-1}$ and brown noise with an energy spectrum $\propto k^{-2}$. These three energy spectra have been tested as sources in the stochastically forced Burgers equation in order to determine how the spectral properties of the source affect the spectral properties of the results.

Simulations have been conducted using the local Lax-Friedrichs method with MUSCL interpolation for the convective fluxes, and the TVD Runge-Kutta method in time with $\Delta t = 5 \cdot 10^{-5}$. The viscosity is $\nu = 1 \cdot 10^{-5}$, there are 2^{13} grid cells for $x \in [0, 1]$, and the source has an amplitude coefficient $A = 0.05$ and forcing at all admissible scales. All amplitude spectra are averaged over $t \in [10, 20]$, after a statistically steady state is reached, and all simulations are started from initial condition $u_0 = 0$.

Figure 2 shows the resulting velocity and time-averaged energy spectra $\overline{|\hat{u}(k)|^2}$ of the solution for the three different source types, white, pink and brown. Also plotted in the figure are the energy spectra of the source functions and proposed regression lines. A first observation is that the presence of a source term, with energy spectrum decreasing less rapidly than the k^{-2} Burgers shocks, reduces the negative slopes of the spectra. The similarity in general shape of the three velocity plots is caused by the pseudo-random number generator starting from the same seed for all three simulations, thus causing identical phases of the source term for the three simulations.

The velocity plots reveal obvious differences between the three different source types. The velocity plotted for the white source shows little coherent large-scale structures, but high-amplitude noise over a wide range of wave numbers. This is caused by the white source having equal amplitudes for all wave numbers. The energy spectrum follows the regression line k^{-1} quite well, serving as a combination between the stochastic noise and the physics of the shocks in the Burgers equation.

The velocity plot for the source with a pink spectrum shows the existence of large-scale structures as well as smaller structures over a range of wave numbers. This is explained by the energy spectrum falling more steeply than for the white source, and following the $k^{-5/3}$ regression line reasonably well. Small scale structures contribute modestly in the last velocity plot, with the brown source. The solution is primarily dominated by the large scale shocks, also apparent in the energy spectrum that follows the expected k^{-2}.

Out of the three velocity plots, the pink noise solution, is the one that resembles real turbulence the most. This is backed up by an energy spectrum following $k^{-5/3}$, Kolmogorov's energy spectrum for homogeneous turbulence, as previously reported by Checklov & Yakhot [4].

The spectral slope of a graph also provides information about other features of the graph. For example a power law energy spectrum proves the existence of scaling laws, and it is expected that the graphs with energy spectral slopes -1, $-5/3$ and -2 have box-counting dimensions [8] 2, 5/3 and 3/2, respectively. A high box-counting dimension is consistent with a high degree of roughness, evident from the velocity plots. The indicated spectral slopes also lead to second order structure functions, $S_2(r) = \overline{[u(x + r) - u(x)]^2}$, scaling as $S_2(r) \propto r^0$, $S_2(r) \propto r^{2/3}$ and $S_2(r) \propto r^1$ for the white, pink and brown source, respectively [8].
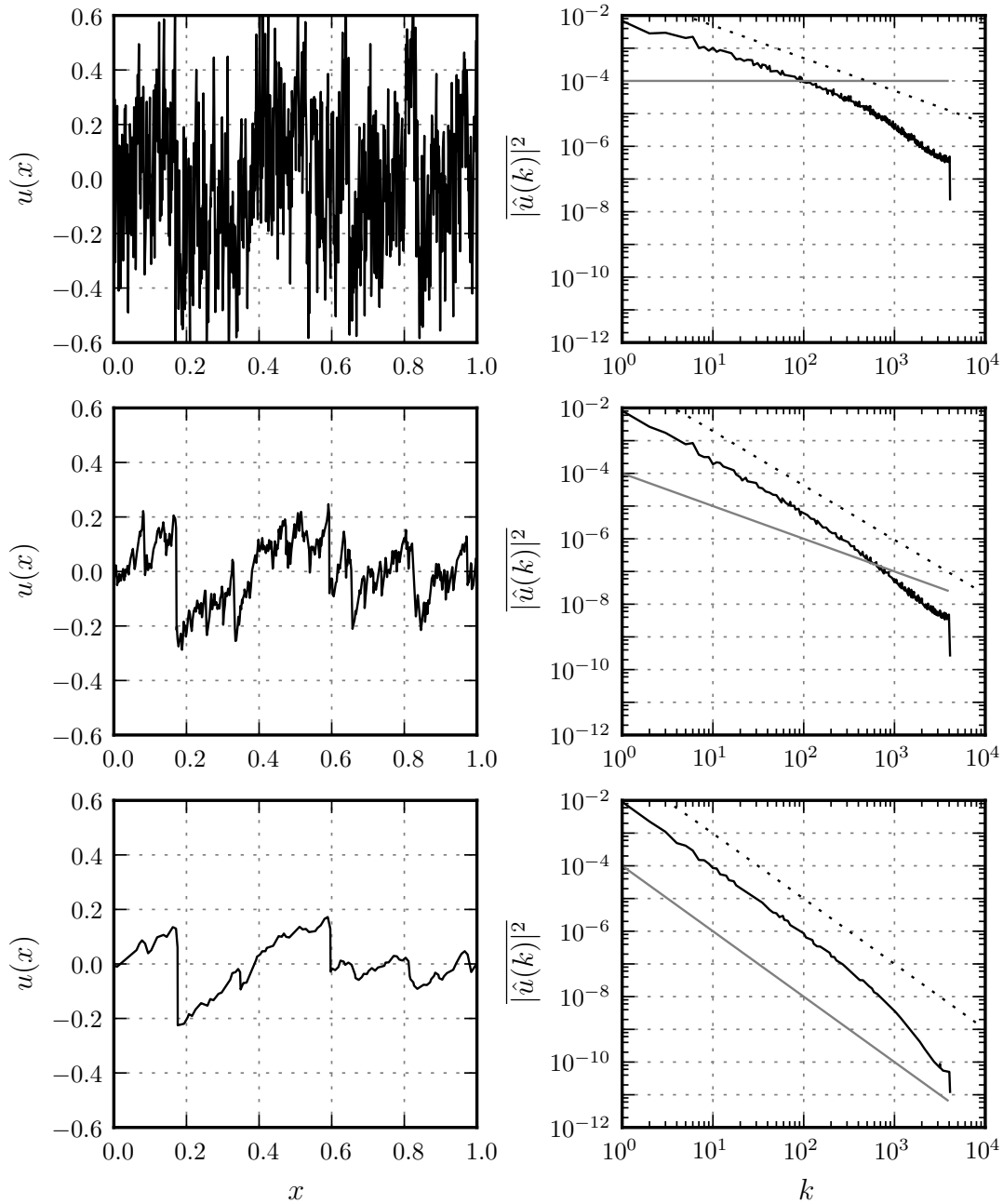
Figure 2: The velocity (left) and energy spectrum (right) for the three different source energy spectrum slopes k^0 (top), k^{-1} (centre) and k^{-2} (bottom), corresponding to white, pink and brown noise, respectively. The grey lines are the energy spectra of the sources (multiplied by a factor 10^{-6}), and the dotted lines represent, from top to bottom, power laws k^{-1}, $k^{-5/3}$ and k^{-2}.
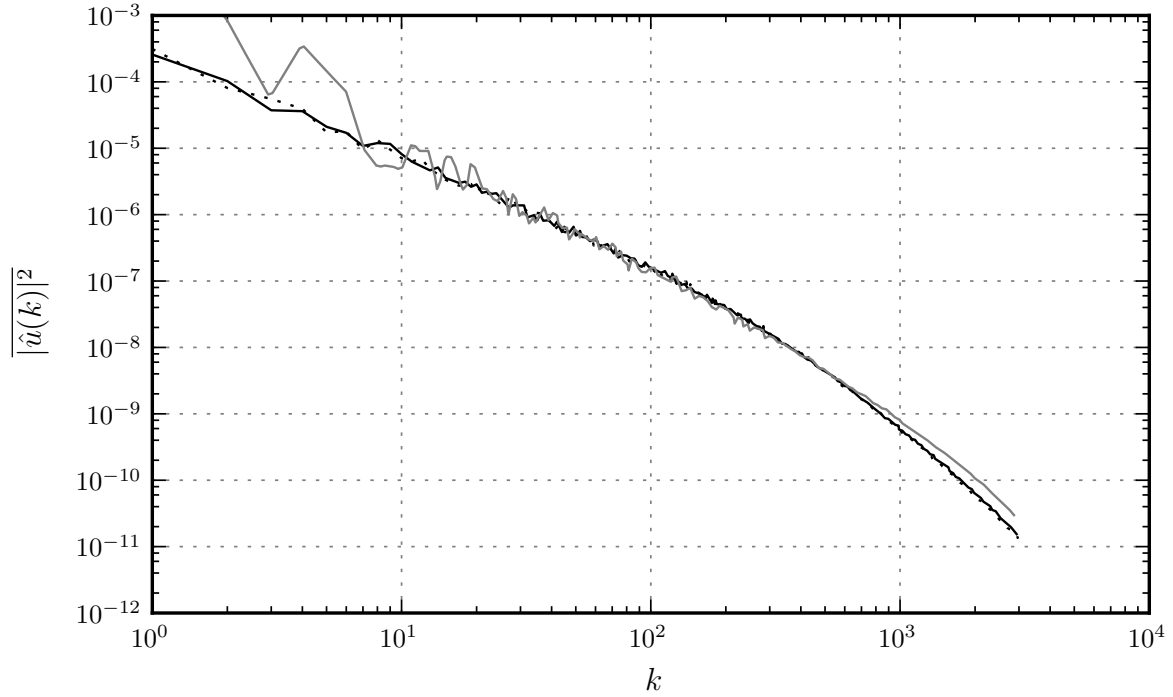
Figure 3: Averaged energy spectra for simulation using 2^{15} grid cells (solid black line) and simulation using 2^{14} grid cells (dotted line), compared with previously published amplitude spectrum of Scotti & Meneveau (grey line) [14].

Burgers turbulence for pink-spectrum source

Simulations using the local Lax-Friedrichs method with MUSCL for 2^{15} and 2^{14} grid cells for $x \in [0, 2\pi]$ were conducted to be compared with previously published results by Scotti & Meneveau [14]. The TVD Runge-Kutta method was used for integration in time, and the time step was $\Delta t = 5 \cdot 10^{-5}$. Kinematic viscosity was $\nu = 1 \cdot 10^{-5}$, and the source parameters were $A = \sqrt{2} \cdot 10^{-3}$, $\alpha = 1$, with forcing at all scales. Initial conditions were $u_0 = 0.1 \sin(2\pi x)$ for the simulation with 2^{15} grid cells and $u_0 = 0.02(x - \pi)$ for the simulation with 2^{14} grid cells.

Energy spectra averaged between $t = 60$ and $t = 200$ are shown in figure 3, compared with results from a pseudo-spectral code by Scotti & Meneveau using 2^{13} modes. All three simulation results exhibit the $-5/3$ energy spectrum slope, characteristic of this type of Burgers turbulence. Spectrum results correspond well for most wave numbers, but deviate for the lowest wave numbers and for wave numbers larger than 10^3. The significance of this deviation is uncertain, but the high wave number difference could be attributed to excessive damping for the simulations presented here. There is however only a marginal difference between the simulation with 2^{15} grid cells and the simulation with 2^{14} grid cells, and if the high wave number discrepancy was caused by numerical diffusion, one would expect the simulation with the highest resolution to yield better results.

It is perhaps more likely that the difference at high wave numbers is related to the difference at the lowest wave numbers. The simulation results from Scotti & Meneveau have large scales with significantly more energy, and thus more energy is transported to the smallest scales. The lack of smoothness at the smallest wave numbers indicates the presence of persistent large scale structures. This difference could perhaps be caused by the implementation of the source term
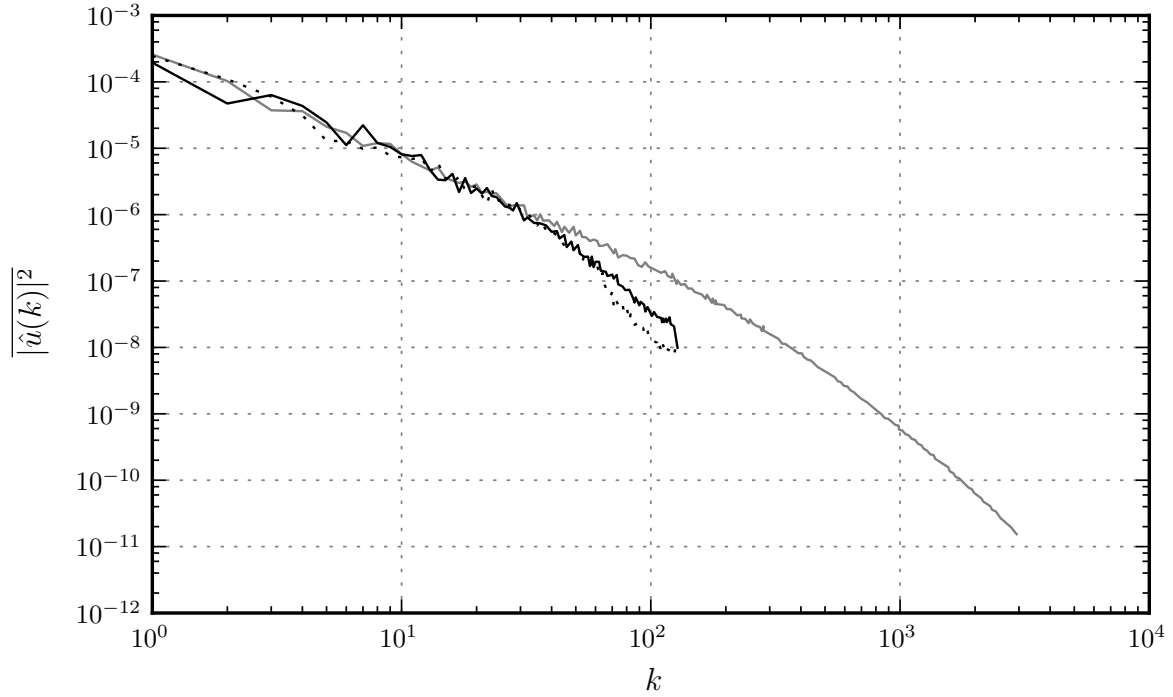
Figure 4: Averaged energy spectra for low resolution simulations using 2^8 grid cells and filter width $\Delta = 2\pi/128$ (solid black line) and filter width $\Delta = 2\pi/64$ (dotted line), compared with simulation using 2^{14} grid cells (grey line).

or the initial condition, the details of which are not entirely clear. Tests with different types of initial conditions have shown that even though the energy of the initial condition quite quickly dies out, traits of the initial condition, in particular shock patterns, survive for a long time.

Additional simulations at a very low resolution of 2^8 grid cells are compared with the high resolution simulation in figure 4, for similar initial conditions. These simulations represent one-dimensional large eddy simulations without subgrid modelling, and are filtered using a spectral cut-off filter (implemented by only prescribing the lowest wave numbers of the stochastic source). Filtering widths of both $\Delta = 2\pi/128$ and $\Delta = 2\pi/64$ were tested.

Energy spectra for both low resolution simulations follow the high resolution energy spectrum for wave numbers smaller than 40, but deviate for larger wave numbers. There is no build-up at the highest wave numbers, as one might expect, but instead excessive damping. Increasing the filtering width to $2\pi/64$ increases the difference at the highest wave numbers. The results show that at this resolution and stochastic forcing, the numerical diffusion is sufficiently large to function as an eddy viscosity, thus dissipating the energy. Sufficient dissipation does not, however, by itself constitute a good subgrid model, and a dedicated subgrid model should be able to produce better results.

The evolution of large scale kinetic energy, defined as $K(t) = 1/(2 \cdot 2\pi) \int_0^{2\pi} \tilde{u}^2 \, dx$, is plotted in figure 5 for the highest resolution simulation, the low resolution simulation filtered at $\Delta = 2\pi/128$ and the simulation by Scotti & Meneveau. $\tilde{u}$ is the velocity u filtered at scale $\Delta = 2\pi/128$. All three spectral curves decay from an initial condition with high kinetic energy and then reach a statistically steady state where forcing and dissipation are in approximate equilibrium. Again it is apparent that the low resolution simulation dissipates a significant
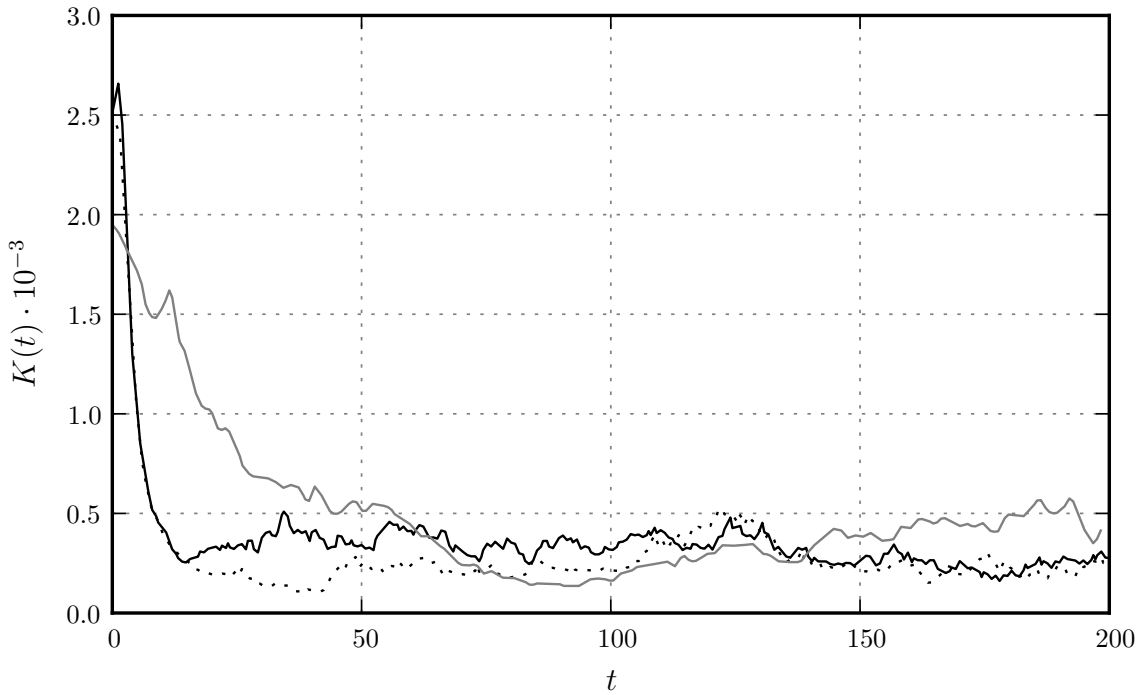
Figure 5: Evolution of large scale kinetic energy simulation using 2^{15} grid cells (solid black line) compared with previously published results from Scotti & Meneveau (grey line) [14] and low resolution simulation with 2^8 grid cells filtered at $\Delta = 2\pi/128$ (dotted line).

amount of energy, as the energy levels out instead of increasing gradually.

Within the statistically steady region, the kinetic energy fluctuations are large. This is because of the instability of the largest scales containing most of the energy, and could also be part of the explanation for the discrepancy seen in figure 3. Truly reliable statistics would require much longer time series than the ones used here. Another noteworthy observation is that the energy decreases far more rapidly from the initial condition for the simulations presented here, than for the results from Scotti & Meneveau. This could be a consequence of different initial conditions, thus supporting the notion that the initial conditions could attribute to some of the difference observed in figure 3.

The effect of time step size was tested by comparing two simulations with 2^{14} grid cells, one with $\Delta t = 5 \cdot 10^{-5}$ and one with $\Delta t = 1 \cdot 10^{-5}$. Energy spectra for these two simulations (not shown) almost completely overlapped, demonstrating that the time step is low enough for the statistical features of the solution to be independent of time step size. This result is contingent on the normalisation by $1/\sqrt{\Delta t}$ in the amplitude of the source.

Energy cascade of Burgers turbulence

Let us once again recall the energy spectrum of Burgers turbulence for a pink noise source, and consider its resemblance to real turbulence. In real three dimensional turbulence the energy spectrum is the result of an energy cascade from large to smaller scales, caused by the three-dimensional vortex stretching that occurs due to the interaction between different sized eddies.

In one-dimensional Burgers turbulence the concept of a vortex does not exist, but still an energy cascade of some sort occurs. Observing figure 6, showing the velocity at time $t = 115$ for the high resolution simulation, some salient features are apparent. The velocity plot is dominated
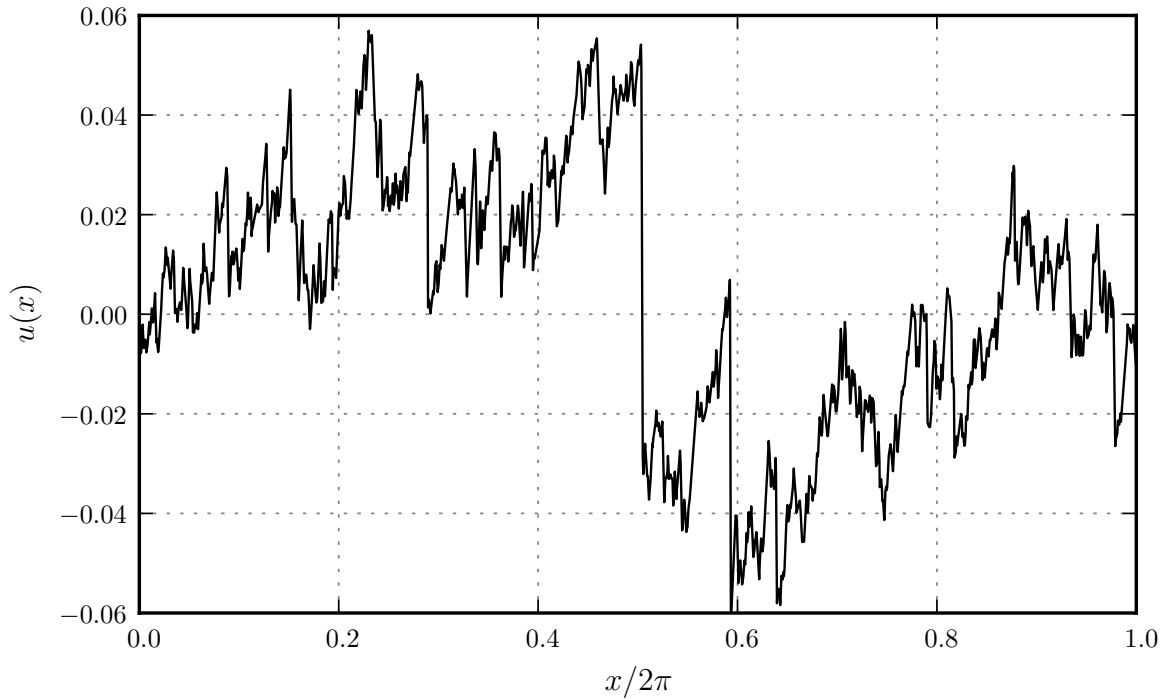
Figure 6: Velocity at time $t = 115$ for simulation with 2^{15} grid cells and pink noise source shows presence of many small shocks and some large shocks.

by a few large shocks, and several smaller ones. Both the creation of large shocks and their breakdown into smaller shocks, take place constantly, serving as an energy interaction and transfer between large and small scales. A forcing that is active over a wide range of scales ensures that both processes occur. Because of this, one would expect a certain degree of backscatter, the process of energy being transported from small to larger scales.

While the energy spectra of the turbulent signals reveal useful information about the spectral properties of the signal, nothing is revealed about the localisation in physical space. The existence of a shock in the solution to the Burgers equation causes an energy spectrum proportional to k^{-2}. Methods, such as wavelet transforms, providing local information about the energy at different wave numbers, would display high wave number peaking around the largest shocks in the solution.

Conclusion

Simulations using the finite volume method for the stochastically forced Burgers equation have shown favourable agreement with previously published results from a pseudo-spectral code. The utilisation of MUSCL interpolation increases the accuracy of the simulation for a given resolution. Very low resolution simulations, representing large eddy simulations without subgrid modelling, showed that the presence of numerical diffusion is sufficient to serve as an eddy viscosity. It is, however, believed that one should be able to get improved results utilising a dedicated subgrid model.

Stochastic forcing with a white (k^0) energy spectrum yields a resulting velocity with an approximately k^{-1} energy spectrum, while a brown (k^{-2}) forcing causes the typical k^{-2} spectrum, characteristic of the shocks. A pink (k^{-1}) forcing spectrum creates a Kolmogorov $k^{-5/3}$ spectrum for the solution.

The evolution of kinetic energy exhibited steady state behaviour with large fluctuations, attributed to the breakdown of larger shocks in the solution. The creation and breakdown of shocks cause an energy interaction between large and small scales. Energy is transported from large to smaller scales, but also, to a lesser degree, from small to large scales.

References

[1] A. L.Barabási and H. E.Stanley *Fractal concepts in surface growth* Cambridge University Press, 1995.

[2] J. M.Burgers A mathematical model illustrating the theory of turbulence *Advances in Applied Mechanics*, **vol.1**, 171–199, 1948.

[3] J. M.Burgers *The nonlinear diffusion equation: asymptotic solutions and statistical problems* Reidel Dordrecht, 1974.

[4] A.Chekhlov and V.Yakhot Kolmogorov turbulence in a random-force-driven Burgers equation *Physical Review E*, **vol.51**, R2739–R2742, 1995.

[5] A.Chekhlov and V.Yakhot Kolmogorov turbulence in a random-force-driven Burgers equation: Anomalous scaling and probability density functions *Physical Review E*, **vol.52**, 5681–5684, 1995.

[6] J. D.Cole On a quasi-linear parabolic equation occurring in aerodynamics *Quarterly of Applied Mathematics*, **vol.9**, 225–236, 1951.

[7] J. W.Cooley and J. W.Tukey An algorithm for the machine calculation of complex Fourier series *Mathematics of Computation*, **vol.19**, 297–301, 1965.

[8] K.Falconer *Fractal Geometry: Mathematical Foundations and Applications* John Wiley & Sons Ltd, 2nd edition, 2003.

[9] U.Frisch and J.Bec "Burgulence" *New trends in turbulence, Turbulence: nouveaux aspects*, pages 341–383, 2001.

[10] B. J.Geurts *Elements of direct and large-eddy simulation* R.T. Edwards, Inc., 2004.

[11] S.Gottlieb and C. W.Shu Total variation diminishing Runge-Kutta schemes *Mathematics of Computation*, **vol.67**, 73–85, 1998.

[12] S. N.Gurbatov, A. N.Malakhov and A. I.Saichev *Nonlinear random waves and turbulence in nondispersive media: waves, rays, particles* Manchester University Press, 1991.

[13] E.Hopf The partial differential equation $u_t + uu_x = \mu u_{xx}$ *Communications on Pure and Applied Mathematics*, **vol.3**, 201–230, 1950.

[14] A.Scotti and C.Meneveau A fractal model for large eddy simulation of turbulent flow *Physica D: Nonlinear Phenomena*, **vol.127**, 198–232, 1999.

[15] Z.-S.She, E.Aurell and U.Frisch The inviscid Burgers equation with initial data of Brownian type *Communications in Mathematical Physics*, **vol.148**, 623–641, 1992.

[16] Y.Sinai Statistics of shocks in solutions of inviscid Burgers equation *Communications in Mathematical Physics*, **vol.148**, 601–621, 1992.

[17] B.van Leer Towards the ultimate conservative difference scheme. II. Monotonicity and conservation combined in a second-order scheme *Journal of Computational Physics*, **vol.14**, 361–370, 1974.

[18] V.Yakhot and A.Chekhlov Algebraic Tails of Probability Density Functions in the Random-Force-Driven Burgers Turbulence *Physical Review Letters*, **vol.77**, 3118–3121, 1996.